# Simulation Methods for the Phase Behavior of Complex Fluids

By

Hyuntae Jung

A dissertation submitted in partial fulfillment of

the requirements for the degree of

Doctor of Philosophy

(Chemistry)

at the

UNIVERSITY OF WISCONSIN-MADISON

2020

Date of final oral examination: 05/05/2020

The dissertation is approved by the following members of the Final Oral Committee:

Arun Yethiraj, Professor, Chemistry

J.R. Schmidt, Professor, Chemistry

Mark Ediger, Professor, Chemistry

Reid Van Lehn, Assistant Professor, Chemical and Biological Engineering

# Simulation Methods for the Phase Behavior of Complex Fluids

Hyuntae Jung

Under the supervision of Professor Arun Yethiraj

At the Univeristy of Wisconsin-Madison

## Abstract

Computer simulations have been widely used in the the study of complex fluids to provide good consistency of macroscopic properties with experiments and understandings in the microscopic view. In the last 10 years, the rise in computing power with graphical processing units and modern data science techniques such as machine learning promote enormous improvements on molecular simulations for studies of complex phenomena which can be challenging, in particular, the phase behavior of complex mixtures. In this thesis, we propose several methods for obtaining phase coexistence of complex fluid mixtures and study phase behaviors of polymer solutions utilizing molecular simulations and a neural network technique. We develop a simulation method for getting phase coexistence from single cell simulations, which uses a spatial concentration autocorrelation function to spatially align instantaneous concentration profiles from different snapshots. Except in the neighborhood of the critical point, the Interface method shows excellent agreement with the phase diagrams of the Widom-Rowlinson model and the symmetric blends of freely jointed polymer molecules available from conventional methods. To obtain coexistence points even near the critical point, we propose a supervised machine learning framework fed by single cell simulation data to optimize convolutional neural network (CNN) filter size as one of hyperparameters. The CNN predictions with simulation data show good agreement with the phase boundary of references close to the critical point. Also, we found that understanding intermediate structures during a phase transition is important to consider them as training sets. Lastly, we study

phase behaviors of poly(ethylene oxide) in imidazolium-based ionic liquids which have the unique low critical solubility temperature phase behavior. We use a hybrid simulation method composed of the Interface method and a neural network model to draw phase diagrams. As a result of prediction of critical points for various systems with substitution of H with $CH_3$ on C2 position and different N-alkyl chain length of cation, our results agree with experimental results. Interestingly, a polymer chain near single C2 methylated cation is likely to form not only wrapping but also crown conformation which implies the entropic-driven phase separation.

## Acknowledgments

I would like to pay my special regards to my advisor, Professor Arun Yethiraj, for giving a chance to solve the scientific problem with my rough, and somewhat unfamiliar idea. He supported me by elaborating such small trials to be meaningful and make them count as publications in theoretical chemistry field. Without his generous support with my work, I would not have been possible for me to complete my degree and publications at the end.

I also wish to show my gratitude to professors JR Schmidt, Mark D. Ediger, Hyuk Yu, Qiang Cui, and Reid Van Lehn for their research topics and activities. Their passion and enthusiasm for science inspired and motivated me to learn from such role models.

I would like to recognize the invaluable assistance from my colleagues; Special thanks to force field developers using Symmetry-adapted perturbation theory in our group, Jesse, Eunsong, Chang Yun, and Kyeong-jun. I will miss all the fun and scientific communications with Tyler, Ajay, Aditya, Inhyuk, and Supreet. I appreciate Xinyi who shared not only the office but also a number of stories and conversations as a best friend.

I also wish to express my gratitude and love to my wife Hyunju who despite several difficulties, encouraged me to prepare and start my PhD program abroad. I would like to remember our past 5 years as one of the most precious memories we have made in our life. I wish to thank to my son Ethan who plays with me and asks to come to the bed and sing a song for his sleeping time.

*This dissertation is dedicated to Hyunju for her devotion and endless love to pursue my dream and to Ethan for his smiles and big warm hug every day.*

# Table of Contents

# List of Tables

# List of Figures

# Chapter 1

# Introduction

Molecular simulation is a powerful and useful tool for studies of chemical, physical, and biological systems. As the simulation performs under physics principles and mathematical equations, we obtain coordinates of molecule in time as output data. Using the data, we can not only calculate various properties to compare with experimental studies such as density, energy, molecular structures, and viscosity but also visualize how they move in such a tiny system. The simulation results can help to interpret complex phenomena in molecular level such as phase behavior of condensed matter. Recently, improvements to both hardware and simulation methods ease obstacles of usage simulations and lead to fast performance and better accuracy of simulation results. Also, modern data-driven techniques such as deep neural network and machine learning combined with simulation methods are rapidly developed with several success on phase behavior predictions. In this dissertation, we aim to propose a new simulation method and a supervised machine learning framework for getting phase boundary of complex fluids, and study the phase separation behavior of polymer in ionic liquid systems utilizing a artificial neural network model.

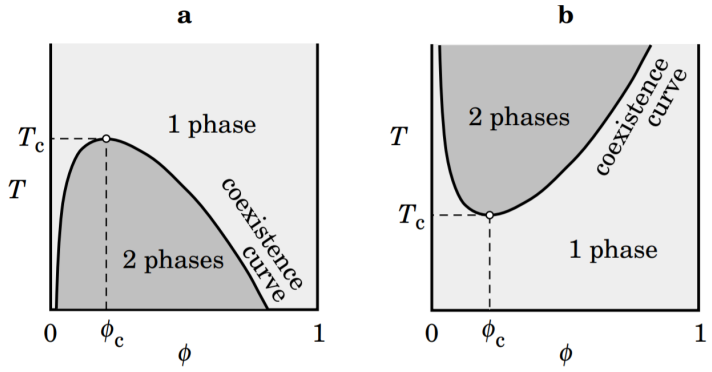


Figure 1.1: Two phase behaviors of polymer solution with respect to temperature and composition for (left) UCST (right) LCST. The critical point has the critical temperature $T_c$ and the critical composition $\phi_c$. Reprinted from Teraoka's book.[1]

## 1.1 Thermodynamics for the miscibility of polymer solvents

The phase separation/mixing behavior of polymer solvent can be understood by a simple thermodynamics equation, $\Delta G_{mix} = \Delta H_{mix} - T\Delta S_{mix}$ where $G$, $H$, $T$ and $S$ are for Gibbs free energy, enthalpy, temperature, and entropy for mixing under constant pressure and temperature, respectively. To be spontaneous mixing for the mixture, $\Delta G_{mix}$ should be negative with appropriate values of temperatures and signs of $\Delta H_{mix}$ and $\Delta S_{mix}$.

In that sense, two terms of the phase transition behavior come out for thermal-responsive mixtures; lower critical solubility temperature (LCST) and upper critical solubility temperature (UCST) in Figure 1.1. UCST behavior of mixtures such as oil and water is that the mixture shows separation (or two-phase, $\Delta G_{mix} > 0$) at a low temperature and mixing (or one-phase, $\Delta G_{mix} < 0$) at a high temperature. It is well understand in terms of relative interactions between components. Like components interact attractively ($\Delta H_{mix} < 0$) or unlike components feel weak repulsion ($\Delta H_{mix} > 0$) at a moderate temperature, then the interactions are weaken and mixing entropy drives mixing at high temperature ($\Delta S_{mix} > 0$). The mixing entropy is usually positive because the number of configurations of components increases when mixing.

However, LCST behaviors can happen under the unusual condition $\Delta S_{mix} < 0$ with two pos-

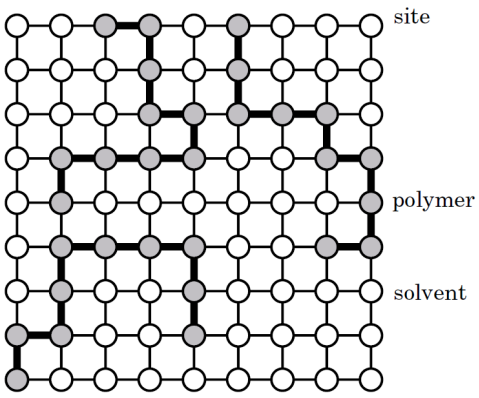


Figure 1.2: Conceptual picture of Flory-Huggins theory for polymer solution. Reprinted from Teraoka's book.[1]

sible mechanisms; loss of free volume when mixing by compressible polymers and reduction of degree of freedom of orientation of polymer and solvents by directional interaction such as hydrogen bonding. The two representative examples of LCST behaviors of polymer solvent are poly(ethylene oxide)[2] (in short, PEO) and poly(N-isopropylacryl amide) (in short, PNIPAM) in water.[3] Because the monomer of those polymers have hydrogen bonding donor and/or acceptor, the LCST behaviors are understood due to hydrogen bondings with water. Beyond the understandings of such complicate phase behaviors in thermodynamics, a theory and a simulation is necessary to explain the transition with details, for example, how the strength of interaction between components affects on the critical point and spatial conformation and dynamics of molecules during phase transition.

## 1.2 The Flory-Huggins theory of mixing/separation behavior of polymer solvents

The simplest theory for phase separation behavior of polymer solution is the Flory-Huggins (FH) theory. The theory hypothesizes that a polymer chain occupies lattice sites which are connected by neighbor sites and a solvent occupies single site with same volume as single polymer site in Figure

1.2. The (Helmholtz) free energy can be expressed by following equation;

$$\frac{\Delta F_{mix}}{N_{site}k_BT} = \chi\phi(1-\phi) + \frac{\phi}{N_p}\ln\phi + (1-\phi)\ln(1-\phi) \tag{1.1}$$

where $F$, $N_{site}$ , $k_B$, $\chi$, $\phi$, and $N_p$ are mixing free energy, the total number of lattice sites, Boltzman constant, interaction parameter, volume fraction of polymer, and the polymer chain length (or the number of sites for single polymer), respectively. Comparing with the thermodynamics equation of $\Delta G_{mix}$ in previous section, the second and third term in Eq. 1.1 correspond with $\Delta S_{mix}$ for polymers and solvents and the first term (typically) correspond with $\Delta H_{mix}$. (see the result when multiplying temperature T on both side) Interaction parameter $\chi$ can be interpreted with combination of interactions of component pairs like following equation;

$$\chi = \frac{Z}{k_BT}\left[\varepsilon_{PS} - \frac{(\varepsilon_{SS}+\varepsilon_{PP})}{2}\right] \tag{1.2}$$

where $\varepsilon_{PS}$ represents interaction strength between polymer (P) and solvent (S) and $Z$ is coordination number, e.g. 4 for a two dimensional lattice model. Rather than Eq. 1.2, in practical cases of fitting phase diagram of polymer solvent, the simple equation with two another parameters A and B is preferred as $\chi = A + \frac{B}{T}$. The practical equation for interaction parameter indicate the appearance of another mixing entropy beside the configurational entropy of polymer and solvent which are the second and third term in Eq. 1.1.

When applying the FH theory to studies of LCST-type phase diagrams, a modified FH theory is necessary because of complicated interactions in mixture. For example, hydrogen bonding can be regarded as a weak interaction between polymer and solvent weakening with increase of temperature, which results in enthalpic correction on the FH equation.[4] Instead of using the specific interaction, one may roughly adapt with solvation energy in terms of dielectric constants to correct enthalpy contribution.[5] Also, an entropic correction can be applicable by reflecting architecture and conformation effect of polymers.[6] For details, I refer a recent review article and polymer

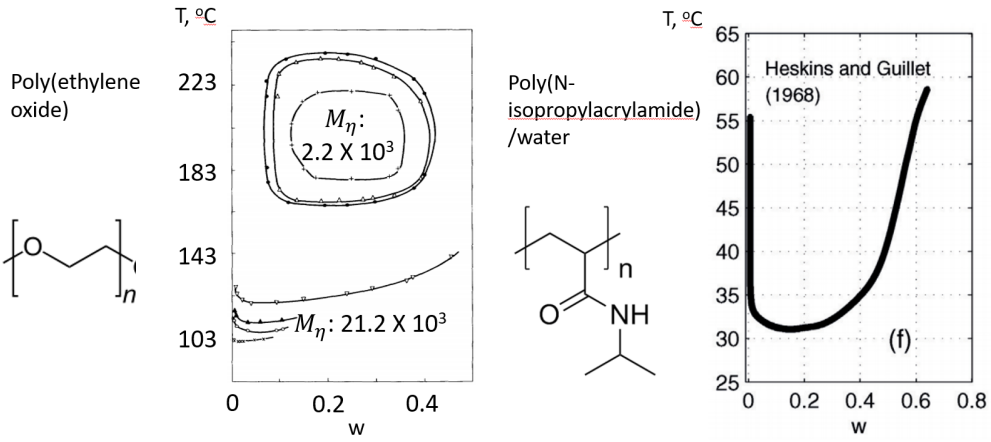


Figure 1.3: Infographics for phase diagrams of (left) poly(ethylene oxide) and (right) poly(N-isopropylacryl amide) in water. The phase diagrams are modified on purpose from references.[2, 3].

physics books for basics of the Flory-Huggins theory and applications.[7, 8]

Connecting the Flory-Huggins (FH) theory with our study of polymer in ionic liquids (ILs), the asymmetric critical composition toward to high fractions of polymer is a unusual behavior. According to the FH theory, the critical composition approximates by $\phi_c \cong \frac{1}{\sqrt{N_p}}$. In other words, polymer solvent systems would show the shift of critical composition toward low volume fraction of polymer for long polymer chain length, which explains the change of critical composition of LCST-type polymer solvents; aqueous PEO solution and PNIPAM solution. Interestingly, Lee et al showed a system of poly(ethylene oxide) (PEO) in imiadzolium-based ionic liquid shows 50 - 80 wt% critical compositions of polymers, which does not agree with the FH theory.[9] Thus, it motivated us for a simulation study for PEO/ILs, which will be described in Chapter 4.

Beside the FH theory, there are available theoretical approaches such as integral equation theory, random phase approximation approach, renormalization group theory, and self-consistent field theory. What they works for phase behavior studies is that they hypothesize a model which is composed of several (dominant) factors on partition function of the mixture and then check if the model works for the phase behavior of a target system using the known phase boundary. But, a study of phase behavior in a molecular/atomic level would be worth in order to obtain somewhat details of

explicit molecules using simulation tools.

## 1.3 Simulation methods for getting phase boundary

Using simulation, the calculation of simple static properties such as pair correlation functions, potential energy, and pressure are relatively straightforward, but the prediction of precise location of phase transitions is not a simple research topic. Phase transitions as collective phenomena occur over a relatively long time and length scales, thus a simulation study for the transition of even single component was challenging until 1987 when Gibbs ensemble method was published.

Since mid-1980s, the Gibbs ensemble method has widely used as a powerful method for getting phase equilibria. Typically, a direct interfacial (or single cell) simulation contains not only coexisting two phases, e.g. A-rich and B-rich phase in A/B binary mixture, but also interface(s) between two phases which is not necessary for getting phase boundary. Unlike the single cell simulation, the Gibbs method takes the coexistence of phases by treating each phase as a separate subsystem, such as one cell for A-rich phase and another cell for B-rich phase,thus there is no physical interface. (see Figure 1.4) Instead of saving computational cost of interface(s) in the single cell simulation, it requires a particle exchange/insertion algorithm to reach the phase equilibria condition on both cells; $T^1 = T^2$, $P^1 = P^2$, and $\mu_i^1 = \mu_i^2$ for $i$ = A or B component for binary mixture in phase 1 and 2 in Fig. 1.4. While the Gibbs method shows success on phase equilibria of toy models, as for practical applications, several bias or weighting algorithms are developed to improve low acceptance rate of particle exchange/insertion in a condensed system. Also, some expanded ensembles were developed for a specific purpose such as particle deletion algorithm instead of insertion. I refer a review article and simulation books for simulations method.[10, 11, 12] Note that we add a note of derivations of Claperyon equation for expanded ensemble simulations of binary mixture in Appendix **??** and reproduce the phase diagram of vapor-liquid transition of Lennard-Jones fluid using Gibbs-Duhem integration in Appendices A. Beside, I put some effects

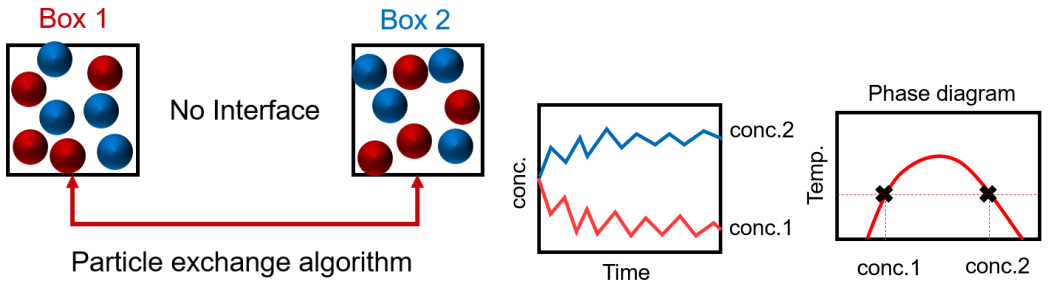


Figure 1.4: Conceptual pictures of Gibbs ensemble simulation of A/B binary mixture to get phase boundary.

by utilizing expanded ensemble simulations and adapting weighted histogram to accelerate polymer insertion in PEO/ILs. Unfortunately, it seems not to work in the way I thought at several preliminary trials.

Since late 1990s, a molecular simulation using single cell started getting attentions back with growing interest on structural properties near interface. With developments of hardware such as the appearance of multithread central processing units (CPUs) and simulation algorithms such as long-range correction and smooth particle mesh Ewald method (PME) on electrostatic potential published in 1995, the simulation can provide both phase behavior and interfacial properties of system simultaneously in a plausible time and length scale with improved accuracy.[13] Recently, huge speed-up of parallel computation performance can be realized by graphics processing units (GPUs) and a new PME method on Lennard-Jones potential appears for better accuracy on weak dispersion energy.[14] In that sense, single cell simulation for drawing phase diagram seems not to be unfeasible longer, but still there are some difficulties. For example, comparing gibbs ensemble simulation, it may take a long computation time, e.g. a few $\mu s$, to reach separation/mixing equilibrium of a large molecules. Relatively strong finite size effect matters because many particles are used for interface and it will suppress (or bias) the phase transition point. Also, simulation settings such as dispersion correction algorithm studied on homogeneous systems can make a difference on phase equilibria due to the inhomogeneous system in a single cell of separation. Nevertheless, surpassing those risks, the good convenience of single cell molecular simulation technique leads

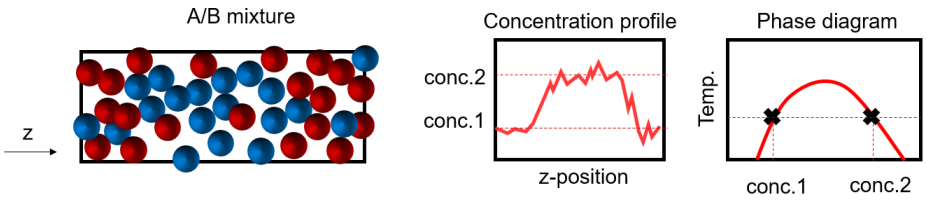


Figure 1.5: Conceptual pictures of single cell simulation of A/B binary mixture to get phase boundary.

to many applications for phase transition studies of condensed matters.

The basic idea to get coexistence is that phase boundary at a given temperature can be obtained from the steady concentration regions which are well shown in Gibbs dividing interface. In other words, when you plot local concentration profile in space for phase separation of mixtures, we may see two steady regions for A and B-rich phase and one smoothly steep region for interface. Unfortunately, in practice, we get the noisy profile every time due to very tiny system size (the small number of particles) and movements of interfaces in time. To reduce noisy local concentration at position, the instantaneous profiles are needed to average in time and correct the movement of interfaces not to artificially smear out concentration values for phases and broaden interfaces. As seen in Figure 1.5, a conventional way to align the interface is to align the center of mass of the total system. It makes sense in some extent because in A/B binary mixture, the concentrations of $A$ components for two steady regions are different enough to distinguish and the components are presumed to evenly distributed within each phase. Although the method is not criticized yet, the assumption would be weak in that noisy and/or asymmetric instantaneous profiles are likely to occur under finite system size. In Chapter 2, we propose a good tool (called interface method) to align interfaces for single cell simulations of phase separation study. Then, we apply the interface method for PEO/ILs with OPLS/AA force field and SAPT-UA force field in Appendix C and Chapter 4, respectively.

In addition to the alignment methods which can get two coexisting compositions at a given temperature, other methods which find phase transition temperature at a given concentration are available using single cell simulations. Depending on what property would be a good indicator for

phase separation behavior of target system, there are various approaches available. In Appendix B, we discuss about local number fluctuation, heat capacity, and polymer segment conformation as order parameters for LCST behavior of PEO in [BMIM][$BF_4$] and [BMIM][$PF_6$].

While I got somewhat useful results of local number fluctuation approach for obtaining phase transition of the two systems, it is not clear about how accurately the approach estimates transition temperatures yet. Also, OPLS/AA force field I used for those systems has a problem on slow dynamics due to full charges of ions, instead of scaled charges which is widely used but shows wrong phase behavior.[15] The slow dynamics indicate it takes a long simulation time for nonequilibrium initial coordinates to be at equilibrium, which might be unfeasible. Also, the anion effect looked obvious and seemed not to be interesting to publish. Meanwhile, symmetry adapted perturbation theory united atom (SAPT-UA) force field of PEO and ILs was developed by Son for fast performance and good accuracy.[16] Therefore, this project moved to use SAPT-UA force field and focus on a cation modification effect by C2-methylation to block the hydrogen bonding on C2 position of imidazolium cation, which will be described in Chapter 4.

## 1.4 New paradigm of data-driven techniques

Currently, machine learning is so popular for data analysis without explicit instructions. Although machine learning algorithms were developed in past, the usage of techniques explosively increase with fast computation performance following Moore's law, the appearance of GPUs, and a number of accessible data in public. As current problems are too complicated to understand underlying principles, machine learning can provide a good solution (or prediction) based on huge amount of available data or big data. The phase transition problem in physics is not an exceptional example as one of machine learning applications.

The conventional method for the prediction of the critical point is to use concepts of universality class, critical exponents, and scaling variables.[17] With Wegner expansion, the order parameter,

e.g. mass fraction difference of A component in two phases (A-rich phase for phase I and B-rich phase for phase II) of A/B binary mixture, can be expressed as

$$w_A^I - w_A^{II} = B_0\tau^{\beta} + B_1\tau^{\beta+\Delta}, \tag{1.3}$$

where $\tau = \frac{T-T_c}{T_c}$. The rectilinear diameter can be expressed as

$$\frac{w_A^I + w_A^{II}}{2} = w_c + A_0\tau + A_1\tau^{1-\Gamma} \tag{1.4}$$

Note that $w_c$ is the mass fraction of component A at the critical point, $A_i$, $i$ = 0, 1 and $B_i$, $i$ = 0,1 are non-universal constants as fitting parameters, while $\beta$, $\Delta$ and $\Gamma$ are universal critical exponents. For the 3D Ising universality class relevant for the present study, the exponents are approximately $\beta$ = 0.326, $\Delta$ = 0.5, and $\Gamma$ = 0.1. Thus, using some coexisting mass fraction point of $A$, we can obtain $T_c$ from Eq. 1.3 and then $w_c$ from Eq. 1.4. The fitting functions for prediction of $T_c$ and $w_c$ work in some extent for many applications including PEO/[BMIM][$BF_4$] with OPLS/AA force field. (see Appendix C) However, the fitting method can be criticized when the coexisting mass fractions are obtained at far from the critical point and a sudden change of phase boundary curve occurs near the critical point.

Machine learning showed a success on predicting phase transition, fed big data without the fitting function and critical exponents. The data can be raw such as coordinates of molecules and molecular type (or kinds of components) from molecular simulation. In fact, other properties calculated from raw data can be also possible for effective feeding and learning, but the order parameter or cumulants such as Binder parameter is not preferred because it is already interfered by some knowledge about phase transition. Under the situation that positions of molecules are only available, human vision is very useful to roughly distinguish mixing/separation of system such as sand/water and oil/water. Then, we can find the analogy between visual images of separation and dog/cat pictures to categorize which image has dog or cat by computer. In Figure 1.6, you can see

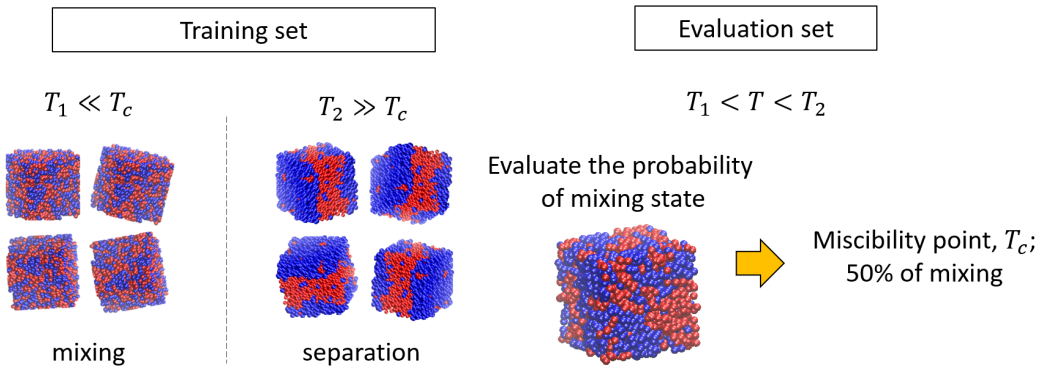


Figure 1.6: A brief explanation of the machine learning strategy about how to train and predict phase of arbitrary binary system of red and blue components.

a strategy of phase prediction by machine learning. Applying the strategy for dog/cat problem in computer vision field, there are various examples in phase transition but limited within 2D and 3D lattice models. Thus, we aim to develop a machine learning framework of 3D off-lattice models in Chapter 3.

Although machine learning (ML) massively contributes to solve many problem, the prediction power is very sensitive on settings including hyperparameters. The hyperparameters define as parameters to set before learning. For example, they are the number and size of filters (or kernels) for convolutional neural network (CNN) and the number of perceptrons for multilayer perceptron (MLP). Also, the prediction result can be changed by architecture of neural network layers including padding, stride size, activation function, optimizer, and initialization scheme on weights. (see an example in Figure 1.7 These factors easily make pitfalls when applying ML to problems in physics, and research scientist is required to have strong domain knowledge to get meaningful result from machine learning.[18] In Chapter3, I was motivated about how to set CNN filter size up for phase transition of binary mixtures of toy models.

In the context, finding optimal hyperparameters is such a overwhelming task to improve the accuracy of machine learning. In order to ease the tedious and seemingly not insightful job, automation machine learning (AutoML) libraries are available. Rather than manually finding optimal hyperparameters, we utilize the best architecture and result suggested from AutoML within one

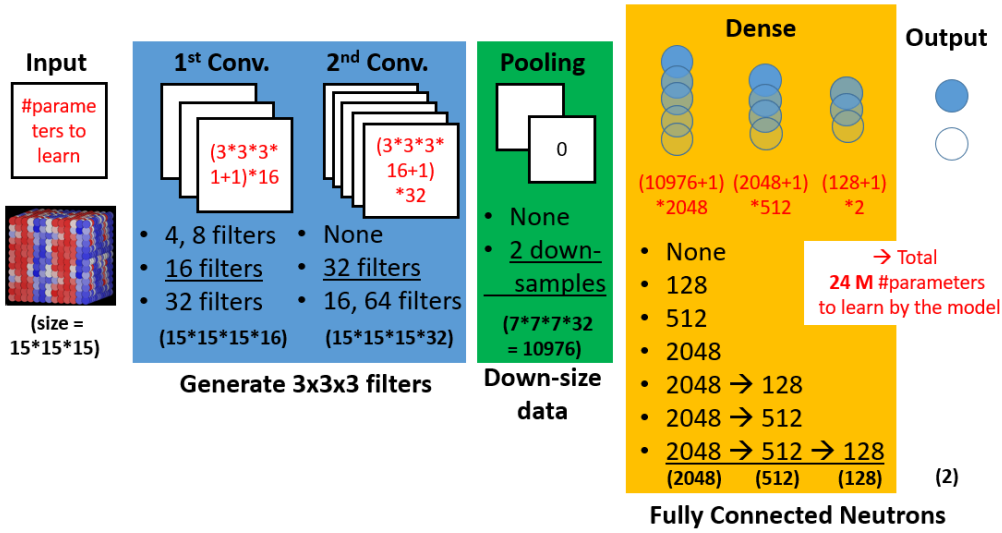


Figure 1.7: An example of several sets of candidate settings of hyperparameters for two-layer CNN model to categorize a image into either of two classes. For the explanation of the number of parameters to optimize and output data size from each layer, we indicate that Red color numbers mean the number of parameters for each layer when choosing the hyperparameter shown as a black underlined text.

day. As another difference with method in Chapter 4, we use collective variables for feeding data, not spatial information in simulation cell. Such these cost-saving algorithm enables us to predict the critical point of complex systems; PEO/IL mixtures in our dissertation. We will discuss details of a hybrid method of molecular simulations and artificial neural networks later.

# References

[1] Iwao Teraoka. *Polymer solutions: an introduction to physical properties*. John Wiley & Sons, 2002.

[2] Susumu Saeki et al. "Upper and lower critical solution temperatures in poly (ethylene glycol) solutions". In: *Polymer* 17.8 (1976), pp. 685–689.

[3] Michael Heskins and James E Guillet. "Solution properties of poly (N-isopropylacrylamide)". In: *Journal of Macromolecular Science—Chemistry* 2.8 (1968), pp. 1441–1455.

[4] Elena E Dormidontova. “Role of competitive PEO- water and water- water hydrogen bonding in aqueous solution PEO behavior”. In: *Macromolecules* 35.3 (2002), pp. 987–1001.

[5] Issei Nakamura. “Spinodal decomposition of a polymer and ionic liquid mixture: Effects of electrostatic interactions and hydrogen bonds on phase instability”. In: *Macromolecules* 49.2 (2016), pp. 690–699.

[6] Glenn H Fredrickson, Andrea J Liu, and Frank S Bates. “Entropic corrections to the Flory-Huggins theory of polymer blends: Architectural and conformational effects”. In: *Macromolecules* 27.9 (1994), pp. 2503–2511.

[7] Piotr Knychała et al. “50th anniversary perspective: phase behavior of polymer solutions and blends”. In: *Macromolecules* 50.8 (2017), pp. 3051–3065.

[8] Michael Rubinstein, Ralph H Colby, et al. *Polymer physics*. Vol. 23. Oxford university press New York, 2003.

[9] Hau-Nan Lee et al. “Unusual lower critical solution temperature phase behavior of poly (ethylene oxide) in ionic liquids”. In: *Macromolecules* 45.8 (2012), pp. 3627–3633.

[10] Athanassios Z Panagiotopoulos. “Monte Carlo methods for phase equilibria of fluids”. In: *Journal of Physics: Condensed Matter* 12.3 (2000), R25.

[11] Daan Frenkel and Berend Smit. *Understanding molecular simulation: from algorithms to applications*. Vol. 1. Elsevier, 2001.

[12] Michael P Allen and Dominic J Tildesley. *Computer simulation of liquids*. Oxford university press, 2017.

[13] Florent Goujon, Patrice Malfreyt, and Dominic J Tildesley. “The gas-liquid surface tension of argon: A reconciliation between experiment and simulation”. In: *The Journal of chemical physics* 140.24 (2014), p. 244710.

[14] Christian L Wennberg et al. “Direct-space corrections enable fast and accurate Lorentz–Berthelot combination rule Lennard-Jones lattice summation”. In: *Journal of chemical theory and computation* 11.12 (2015), pp. 5737–5746.

[15] Eunsong Choi and Arun Yethiraj. “Entropic mechanism for the lower critical solution temperature of poly (ethylene oxide) in a room temperature ionic liquid”. In: *ACS Macro Letters* 4.7 (2015), pp. 799–803.

[16] Chang Yun Son et al. “First-principles united atom force field for the ionic liquid bmim+ bf4–: An alternative to charge scaling”. In: *The Journal of Physical Chemistry B* 120.14 (2016), pp. 3560–3568.

[17] JV Sengers and JMH Levelt Sengers. “Thermodynamic behavior of fluids near the critical point”. In: *Annual Review of Physical Chemistry* 37.1 (1986), pp. 189–222.

[18] Patrick Riley. *Three pitfalls to avoid in machine learning*. 2019.

# Chapter 2

# A Simulation Method for the Phase Diagram of Complex Fluid Mixtures

## 2.1 Introduction

The phase behavior of mixtures of complex fluids is an important and interesting topic. There are fundamental questions in, for example, the phase behavior of polymer solutions, especially with complex solvents such as water or room temperature ionic liquids[1]. Polymer solutions can display a lower critical solution temperature (LCST), i.e., the solution is mixed at low temperatures but phase separates upon heating, or an upper critical solution temperature (UCST), i.e., the solution is mixed at high temperatures but phase separates upon cooling. The phase behavior of polymers can be qualitatively different depending on the solvent. For example, poly (N-isopropylacrylamide) (PNIPAm) exhibits an LCST in water,[2, 3] but a UCST in some ionic liquids.[4, 5, 6, 7] On the other hand poly (ethylene oxide) (PEO) displays both an LCST and UCST in water,[8, 9, 10, 11] but is soluble in many ionic liquids and displays an LCST in some cases.[1, 12, 13]

Computer simulations are a valuable tool to study the phase behavior of complex fluids, but are challenging for polymer solutions. In the Gibbs ensemble method [14] for binary mixtures, for ex-

ample, one starts with two simulation cells chosen so that the conditions are within the coexistence region. In addition to moving the molecules around in each cell, attempts are made to transfer molecules of each species from each cell to the other, with an acceptance criterion chosen to ensure equality of chemical potentials. This method has many successes [15, 16, 17], but for complex fluids the challenge is that successful insertions are rare.[18] Expanded ensemble methods[19, 20, 21, 22, 23, 24] alleviate this problem for model polymer systems, but their implementation for atomistic models is challenging and has not been attempted, to our knowledge. If one coexistence point is known, the rest of the phase diagram can be obtained by Gibbs-Duhem integration[22, 21] although, for binary mixtures, this still requires the insertion/deletion of one of the components.

An alternative for binary mixtures is to simulate a spatially inhomogeneous system with an explicit interface. This requires a large simulation cell so that there are two "bulk" coexisting regions well separated by an interface [25, 26]. Very large simulation cells are necessary but this is not a significant factor given current computational resources. A more problematic issue is that the interface moves during the course of the simulation[27, 28, 29]. For a long enough simulation the interface should move through the entire simulation cell making it difficult to determine coexisting concentrations. Another challenge is that finite size effects are particularly important with an interface due to capillary waves. Single cell simulations have been used successfully to investigate coexistence between the crystal and solution (or melt) of Urea[30, 31] and NaCl[32, 33] to determine the solubility, but the crystal interface is sharp, unlike a fluid-fluid interface.

Direct interfacial simulations can be useful if combined with methods to suppress the movement of the interface.[34] For example, the center-of-mass of one of the components can be chosen as the origin of the co-ordinate system. Alternatively the Gibbs dividing surface can be calculated for each snapshot and this location used as the origin of the simulation cell. These methods have some disadvantages; the center-of-mass of one of the components can be located outside its domain due to periodic boundary conditions and the interface location can be ambiguous when the interface is broad.

In this work, we present a method to align the interfaces obtained in different snapshots of the simulation and therefore obtain converged average values for the coexistence properties. We test the method by comparing our results for the phase diagram to previous simulations of the Widom-Rowlinson (WR) model[35, 23, 36] and symmetric polymer blends.[37]; the agreement is excellent except in the vicinity of the critical point where the interface is too broad. The method can be readily applied to any complex fluid mixture.

## 2.2 Convolution Method

Consider a binary mixture of species $A$ and $B$ where $N_i$ is the number of molecules of species $i$ and $N = N_A + N_B$. The simulation cell is a rectangular parallelepiped with dimensions $L_x$, $L_y$ and $L_z$ in the three Cartesian coordinates, with the origin at (0,0,0). We assume that the interface between the two phases occurs along the $z$ direction. In practice this is always the case if the dimension $L_z$ is chosen to be much larger than $L_x$ and $L_y$.

For a phase separated system (see figure 2.1) the position of the interface moves along $z$ and we wish to shift the concentration profile so that the center of the A-rich phase is at $z$=0. To achieve this shift we define a concentration autocorrelation function and shift the concentration along the $z$-axis to maximize the overlap with the autocorrelation function. We define a concentration autocorrelation function, $C_{AA}(d)$, by

$$C_{AA}(d) \equiv \sum_{z=0}^{L_z} \Delta x_A(z)\, \Delta x_A(z-d) \tag{2.1}$$

where $\Delta x_A(z) \equiv x_A(z) - \langle x_A \rangle$, $x_A(z)$ is the molecule fraction of species $A$, and $\langle x_A \rangle = N_A/V$ is the average value of $x_A(z)$ in the simulation cell, and $V$ is the volume. We use a summation instead of an integral because the concentration profile is obtained by binning in the $z$ direction. The concentration autocorrelation function is a marker of the extent of the coexisting phases because the local mole fraction at the center of $A$-rich phase positively correlates with that in the same

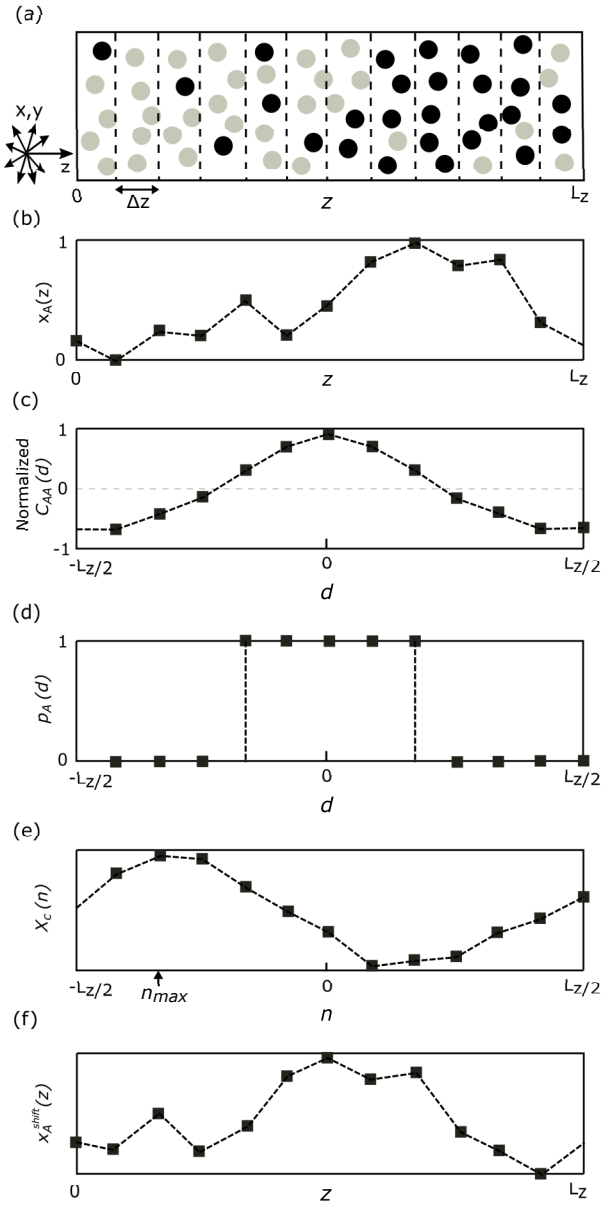


Figure 2.1: Pictorial depiction of the convolution method: (a) Snapshot of $A$ (black) and $B$ (gray) particles, (b) the instantaneous mole fraction profile $x_A(z)$, (c) the mole fraction autocorrelation function $C_{AA}\,(d)$ (Eq. 2.1), (d) the pulse function $p_A(z)$ which has the same domain size as that shown in $C_{AA}\,(d)$ (e) the function $X_c(n)$ (Eq. 2.3), and (f) the optimally shifted mole fraction profile $x_A^{shift}(z)$.

bulk domain, weakly correlates with that near interface, and negatively correlates with that in the opposite phase ($A$-poor phase). In other words, the (normalised) autocorrelation monotonically decays from 1 at the origin to -1 at $-L_z/2$ and $L_z/2$. The pulse function, $p_A(d)$, defined as

$$p_A(d) \equiv \begin{cases} 1 & if \quad C_{AA}(d) \geq 0 \\ 0 & if \quad C_{AA}(d) < 0 \end{cases} \tag{2.2}$$

has the same width as $C_{AA}(d)$ and we use this function to shift the concentration profile as follows.

To shift the concentration profile optimally we find the overlap of the concentration profile with $p_A(d)$ and shift the former to maximize the overlap. We define the function

$$X_c(n) \equiv \sum_{z=0}^{L_z} x_A(z)\, p_A(n-z) \tag{2.3}$$

where $n$ is a shift distance along $z$-direction and choose $n$ so that this overlap is maximum. If $n_{max}$ is the value of $n$ for which $X_c(n)$ is a maximum, then the desired shifted concentration profile is given by

$$x_A^{shift}(z) = x_A(z + n_{max}) \tag{2.4}$$

which is the central result of this method. Concentration profiles from subsequence snapshots are therefore aligned so that the center of the bulk A phase is at the origin.

Once the concentration profiles from different snapshots are aligned we can obtain an average concentration profile from the simulations. The co-existing "bulk" concentrations are then obtained by fitting this concentration profile to an error function.[38, 39, 40] One could, alternatively, just take the concentration at the center of the bulk phases as the co-existing concentration but the statistical uncertainties are larger.

## 2.3 Models and simulation methods

We test the method by applying it to two model systems for which the phase diagram is already available: The Widom Rowlinson mixture and a symmetric blend of freely-jointed polymer chains.

The WR mixture has two components A and B where the interaction potentials, $u_{ij}(r)$, are given by $u_{AA}(r) = u_{BB}(r) = 0$ and $u_{AB}(r) = 0$ for $r > \sigma$ and $u_{AB}(r) = \infty$ for $r < \sigma$. This system phase separates when the total density $\rho \equiv (N_A + N_B)/V$ of the system is large enough.

We use canonical ensemble Monte Carlo simulations for the WR mixture. The simulation cell has $L_x = L_y$ and $L_z/L_x = 5$ with up to $N = 131,072$ particles and $L_z$ chosen to achieve the desired density. Initial configurations are constructed with perfectly separated systems with a flat interface. The system is propagated via single particle moves, i.e., a particle is chosen at random and translated in a randomly chosen direction by an amount chosen uniformly on (0,$\sigma$). The move is accepted if there is no overlap with a particle of the other species and rejected otherwise. The system is equilibrated until the coexisting concentrations reach a steady value, approximately $5\times10^{11}$ steps. Properties are then averaged over $5\times10^{11}$ steps. Statistical uncertainties are reported as one standard deviation about the mean from 10 independent runs.

The two components of the symmetric polymer blend model are freely-jointed tangent sphere chains with $N_{pol}$ sites of mass $m$. Neighboring beads along the chain backbone interact via a harmonic spring $U_{bond}(r) = k(r - b_{eq})^2$, where $k$ is a spring constant and $b_{eq}$ is equilibrium bond length. We use $k = 1000$ and $b_{eq} = \sigma$. All other beads interact via a cut-and-shifted Lennard-Jones potential, i.e.,

$$u_{ij} = \begin{cases} 4\varepsilon_{ij}\left[\left(\frac{\sigma_{ij}}{r}\right)^{12} - \left(\frac{\sigma_{ij}}{r}\right)^{6}\right] - U_{shift}, & r \leq 2.5\sigma \\ 0, & r \geq 2.5\sigma \end{cases} \tag{2.5}$$

where $U_{shift}$ is the LJ potential at $r = 2.5\sigma$. We consider the system studied by Gromov and de Pablo [37] where $\sigma_{AA} = \sigma_{AB} = \sigma_{BB} = \sigma$ and $\epsilon_{AA} = \epsilon_{BB} = \epsilon$ and $\epsilon_{AB} = 0.9\epsilon$.

We perform molecular dynamics simulations using the GROMACS 2016.3 software pack-

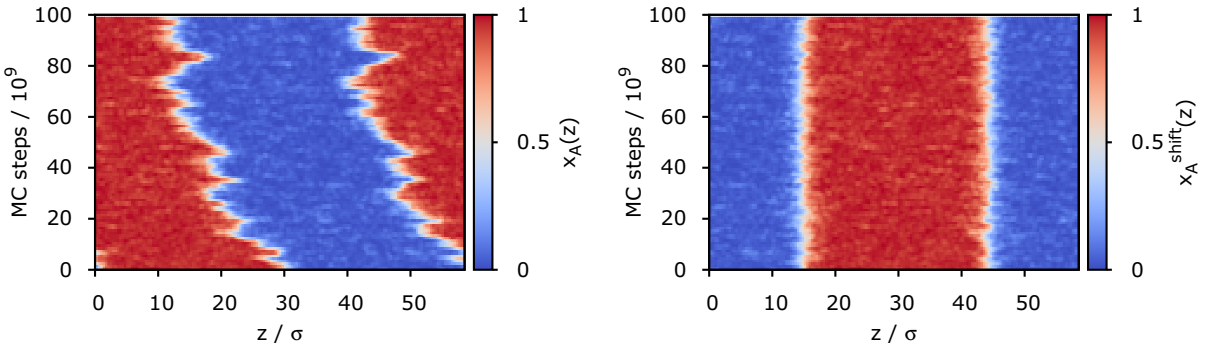


Figure 2.2: Time evolution of the concentration profile of the WR model with $\rho\sigma^3 = 0.9998$ and $N = 8,192$ particles: (left) raw concentration profile and (right) aligned concentration profile. Blue and red regions denote A and B species, respectively.

age[41] to obtain the properties of the symmetric polymer blend. We investigate $N_{pol} = 32$ and $64$ with up to 4096 polymer chains for 32-mers and 2048 polymer chains for 64-mers. Initial configurations are generated by placing the chains on a lattice with the mole fraction on the left half of the box fixed at 0.95 and with $L_x = L_y$ and $L_z/L_x = 10$. The system is equilibrated in the isothermal-isobaric ensemble with fixed cross-sectional area and constant normal pressure. The temperature and normal pressure are controlled using a Nose-Hoover thermostat and a Parrinello-Rahman barostat with $P_z = 1\epsilon/\sigma^3$. The system is propagated using the Verlet integration with a reduced time step of $0.004\sigma\sqrt{m/\varepsilon}$. The equilibrated systems has a ratio $L_z/L_x \approx 5.0$. Approximately $12 \times 10^7$ time steps are required for equilibration and average properties are collected over $25 \times 10^7$ time steps. Statistical uncertainties are obtained via block averaging.

## 2.4 Results and Discussions

The convolution method successfully aligns the concentration profiles from different snapshots. Figure 2.2 depicts the instantaneous concentration profile (top) and the aligned concentration profile (bottom) for the WR mixture. The position of the interfaces is clearly time independent in (b) as required for the estimation of the concentration profiles and coexistence concentrations.

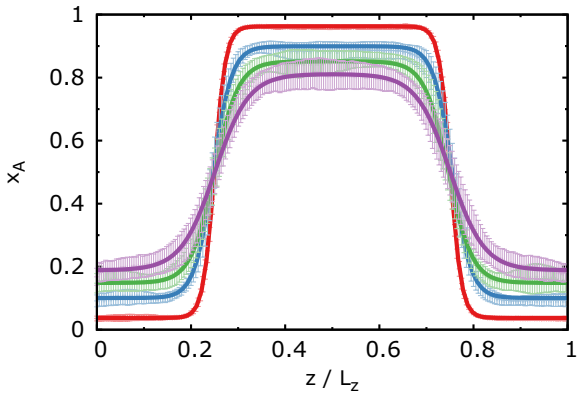


Figure 2.3: Concentration profiles of the WR mixture for $\rho\sigma^3 = 0.9998$ (red), $0.8546$ (blue), $0.8106$ (green), and $0.7831$ (purple). Solid lines are fits to the error function.

The average concentration profiles for the WR mixture are depicted in figure 2.3 for various values of the density. As might be expected, the interface is sharp at high densities and becomes broader as one approaches the critical point. Also shown are fits to the error function from which the co-existing concentrations are determined. A good fit is obtained in all cases, although reading off the concentration from the flat part of the concentration profile is also feasible.

The alignment of concentration profiles and fit to the average concentration profiles works equally well for the symmetric polymer blend and these results are therefore not explicitly shown.

The phase diagrams obtained from direct interfacial simulations are in good agreement with previous simulations. Figure 2.4 compares the results of this work to previous semi-grand canonical ensemble simulations of Shew and Yethiraj (SY)[35] Miguel, Almarza, and Jackson (MAJ),[23], and Djikaev.[36]. The statistical uncertainties are smaller than the size of the symbols and the agreement with previous simulations is excellent. The single cell method of this work fails very close to the critical point because of the large concentration fluctuations, but we are able to obtain results to within $\sim$6% of the critical density.

Figure 2.5 compares direct interfacial simulation results for the phase diagram of symmetric polymer blends to expanded Gibbs ensemble simulations of Gromov and de Pablo [37] for 32-mers and 64-mers. As with the WR mixture results from the direct simulations are in excellent

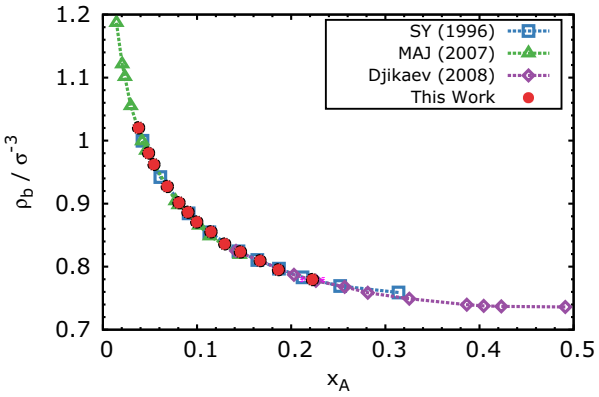


Figure 2.4: The phase diagram of the Widom-Rowlinson mixture from this work (red circles) compared to previous results from Shew and Yethiraj (SY),[35] Miguel, Almarza, and Jackson (MAJ),[23] and Djikaev.[36] Note that $\rho_b$ is the density of the co-existing phases.

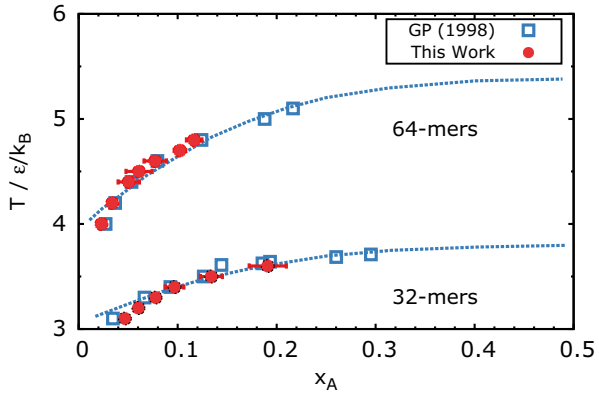


Figure 2.5: Phase diagrams of the symmetric polymer blends from this work compared to the results of Gromov and de Pablo (GP)[37]. Dotted lines are best fits to Ising scaling expressions[37].

agreement with previous work, within statistical uncertainties. The method has challenges near the critical point, but the method is successful to within $\sim$5% of the critical temperature for 32-mers and $\sim$11% of the critical temperature for 64-mers.

## 2.5 Conclusions

We present a method to obtain the phase behavior of complex fluids from direct interfacial simulations. The key idea is that a method to align the interface from different snapshots in order to

obtain average concentration profiles. The simulation results for the phase diagram are in excellent agreement with previous simulations for the Widom-Rowlinson mixture and symmetric polymer blends. These are stringent tests because in the first case concentration fluctuations are large, and in the second case Gibbs ensemble simulations, although feasible, are challenging.

The only drawback is that the method fails near the critical point and to obtain the critical properties accurately one would have to combine the method with another techniques which do not simulate interfaces. As the critical point is approached, interface thickness $w$ diverges as $w \sim (T - T_c)^{-\nu}$ where $T_c$ is the critical temperature and $\nu$ is the critical exponent,[42, 43] and direct interfacial simulations are not computationally feasible. Far from the critical point, however, we estimate the computational costs are comparable to Gibbs ensemble simulations. In practice, Gibbs ensemble simulations are more computationally intensive than NVT simulations.[44] If one assumes the computational time is proportional to the number of steps, for Lennard-Jones particles an NVT simulation of 131,072 particles takes the same time as a Gibbs ensemble simulation of 4096 particles. For the systems studied here, the simulations with an interface required roughly 8 times the number of particles as in previous Gibbs ensemble simulations, suggesting the computational demands will be similar.

The method is expected to be particular useful for complex interacting systems such as mixtures of polymers in room temperature ionic liquids. These systems are complicated by the necessity of using atomistic polarizable models. In addition, the species are strongly interacting and bulky and the combination of these factors makes standard Gibbs ensemble simulations daunting. Another advantage of interfacial simulations is that the properties of the interface, such as interface width, surface tension, molecular orientations and structures at interfaces, can also be investigated. The convolution method might also be useful in simulations of crystal-liquid interfaces, especially when crystal growth rates are of interest. In this case the location of the interface can be accurately determined from the number fluctuation of solid molecules.[45, 46, 47] The method is trivially implemented on standard simulation packages and only requires post-processing of simulation

data.

# References


[1] Hau-Nan Lee et al. “Unusual Lower Critical Solution Temperature Phase Behavior of Poly(ethylene oxide) in Ionic Liquids”. In: *Macromolecules* 45.8 (2012), pp. 3627–3633.

[2] M. Heskins and J. E. Guillet. “Solution Properties of Poly(N-isopropylacrylamide)”. In: *Journal of Macromolecular Science: Part A - Chemistry* 2.8 (1968), pp. 1441–1455.

[3] H.G. Schild. “Poly(N-isopropylacrylamide): experiment, theory and application”. In: *Progress in Polymer Science* 17.2 (1992), pp. 163 –249.

[4] Ueki Takeshi and Watanabe Masayoshi. “Upper Critical Solution Temperature Behavior of Poly(N-isopropylacrylamide) in an Ionic Liquid and Preparation of Thermo-sensitive Nonvolatile Gels”. In: *Chemistry Letters* 35.8 (2006), pp. 964–965.

[5] Takeshi Ueki and Masayoshi Watanabe. “Polymers in Ionic Liquids: Dawn of Neoteric Solvents and Innovative Materials”. In: *Bulletin of the Chemical Society of Japan* 85.1 (2012), pp. 33–50.

[6] Hanako Asai et al. “Structural Study on the UCST-Type Phase Separation of Poly(N-isopropylacrylamide) in Ionic Liquid”. In: *Macromolecules* 46.3 (2013), pp. 1101–1106.

[7] Zhangwei Wang and Peiyi Wu. “Spectral Insights into Gelation Microdynamics of PNIPAM in an Ionic Liquid”. In: *The Journal of Physical Chemistry B* 115.36 (2011). PMID: 21834526, pp. 10604–10614.

[8] Susumu Saeki et al. “Upper and lower critical solution temperatures in poly (ethylene glycol) solutions”. In: *Polymer* 17.8 (1976), pp. 685 –689.

[9] Y. C. Bae et al. “Representation of vapor–liquid and liquid–liquid equilibria for binary systems containing polymers: Applicability of an extended flory–huggins equation”. In: *Journal of Applied Polymer Science* 47.7 (1993), pp. 1193–1206.

[10] Ana Saraiva, Ole Persson, and Aage Fredenslund. “An experimental investigation of cloud-point curves for the poly(ethylene glycol)/water system at varying molecular weight distributions”. In: *Fluid Phase Equilibria* 91.2 (1993), pp. 291 –311.

[11] Piotr Knychała et al. “50th Anniversary Perspective: Phase Behavior of Polymer Solutions and Blends”. In: *Macromolecules* 50.8 (2017), pp. 3051–3065.

[12] Ronald P. White and Jane E. G. Lipson. “Origins of Unusual Phase Behavior in Polymer/Ionic Liquid Solutions”. In: *Macromolecules* 46.14 (2013), pp. 5714–5723.

[13] Eunsong Choi and Arun Yethiraj. “Entropic Mechanism for the Lower Critical Solution Temperature of Poly(ethylene oxide) in a Room Temperature Ionic Liquid”. In: *ACS Macro Letters* 4.7 (2015), pp. 799–803.

[14] A.Z. Panagiotopoulos et al. “Phase equilibria by simulation in the Gibbs ensemble”. In: *Molecular Physics* 63.4 (1988), pp. 527–545.

[15] Athanassios Z. Panagiotopoulos. “Direct Determination of Fluid Phase Equilibria by Simulation in the Gibbs Ensemble: A Review”. In: *Molecular Simulation* 9.1 (1992), pp. 1–23.

[16] Mohammadhasan Dinpajooh et al. “Accurate and precise determination of critical properties from Gibbs ensemble Monte Carlo simulations”. In: *The Journal of Chemical Physics* 143.11 (2015), p. 114113.

[17] B. Smit, Ph. De Smedt, and D. Frenkel. “Computer simulations in the Gibbs ensemble”. In: *Molecular Physics* 68.4 (1989), pp. 931–950.

[18] In: *Understanding Molecular Simulation: From Algorithms to Applications*. Ed. by Daan Frenkel and Berend Smit. 2ed. San Diego: Academic Press, 2002.

[19] Manoj Mehta and David A. Kofke. “Molecular simulation in a pseudo grand canonical ensemble”. In: *Molecular Physics* 86.1 (1995), pp. 139–147.

[20] Fernando A. Escobedo and Juan J. de Pablo. “Expanded grand canonical and Gibbs ensemble Monte Carlo simulation of polymers”. In: *The Journal of Chemical Physics* 105.10 (1996), pp. 4391–4394.

[21] David A. Kofke. “Semigrand Canonical Monte Carlo Simulation; Integration Along Coexistence Lines”. In: *Advances in Chemical Physics*. John Wiley and Sons, Inc, 2007, pp. 405–441.

[22] David A. Kofke and Eduardo D. Glandt. “Monte Carlo simulation of multicomponent equilibria in a semigrand canonical ensemble”. In: *Molecular Physics* 64.6 (1988), pp. 1105–1131.

[23] Enrique de Miguel, Elvira Martín del Río, and Margarida M. Telo da Gama. “Liquid–liquid phase equilibria of symmetrical mixtures by simulation in the semigrand canonical ensemble”. In: *The Journal of Chemical Physics* 103.14 (1995), pp. 6188–6196.

[24] A. Sariban and K. Binder. “Phase separation of polymer mixtures in the presence of solvent”. In: *Macromolecules* 21.3 (1988), pp. 711–726.

[25] Keith E. Gubbins. “The Role of Computer Simulation in Studying Fluid Phase Equilibria”. In: *Molecular Simulation* 2.4-6 (1989), pp. 223–252.

[26] Athanassios Z Panagiotopoulos. “Monte Carlo methods for phase equilibria of fluids”. In: *Journal of Physics: Condensed Matter* 12.3 (2000), R25.

[27] F. P. Buff, R. A. Lovett, and F. H. Stillinger. “Interfacial Density Profile for Fluids in the Critical Region”. In: *Phys. Rev. Lett.* 15 (15 1965), pp. 621–623.

[28] Vladimir Privman. “Finite-Size Properties of the Angle-Dependent Surface Tension of Rough Interfaces”. In: *Phys. Rev. Lett.* 61 (2 1988), pp. 183–186.

[29] Fabian Schmitz, Peter Virnau, and Kurt Binder. “Logarithmic finite-size effects on interfacial free energies: Phenomenological theory and Monte Carlo studies”. In: *Phys. Rev. E* 90 (1 2014), p. 012128.

[30] E. S. Boek et al. “Molecular-dynamics simulations of interfaces between water and crystalline urea”. In: *The Journal of Chemical Physics* 96.9 (1992), pp. 7010–7018.

[31] E. S. Boek, W. J. Briels, and D. Feil. “Interfaces between a Saturated Aqueous Urea Solution and Crystalline Urea: A Molecular Dynamics Study”. In: *The Journal of Physical Chemistry* 98.6 (1994), pp. 1674–1681.

[32] Ranjit Bahadur et al. “Void-induced dissolution in molecular dynamics simulations of NaCl and water”. In: *The Journal of Chemical Physics* 124.15 (2006), p. 154713.

[33] Kazuya Kobayashi et al. “Molecular dynamics study of salt–solution interface: Solubility and surface charge of salt in water”. In: *The Journal of Chemical Physics* 140.14 (2014), p. 144705.

[34] Michael P. Allen and Dominic J. Tildesley. “Computer Simulation of Liquids: Second Edition”. In: Oxford Scholarship, 2017, pp. 1–640.

[35] Chwen-Yang Shew and Arun Yethiraj. “Phase behavior of the Widom–Rowlinson mixture”. In: *The Journal of Chemical Physics* 104.19 (1996), pp. 7665–7670.

[36] Yuri Djikaev. “The interfacial tension and phase diagram of the Widom-Rowlinson mixture via Monte Carlo simulations”. In: *The Journal of Chemical Physics* 128.1 (2008), p. 014712.

[37] Dmitry G. Gromov and Juan J. de Pablo. “Phase equilibria in binary polymer blends: Integral equation approach”. In: *The Journal of Chemical Physics* 109.22 (1998), pp. 10042–10052.

[38] Scott W. Sides, Gary S. Grest, and Martin-D. Lacasse. “Capillary waves at liquid-vapor interfaces: A molecular dynamics simulation”. In: *Phys. Rev. E* 60 (6 1999), pp. 6708–6713.

[39] Ahmed E. Ismail, Gary S. Grest, and Mark J. Stevens. “Capillary waves at the liquid-vapor interface and the surface tension of water”. In: *The Journal of Chemical Physics* 125.1 (2006), p. 014702.

[40] J. S. Huang and W. W. Webb. “Diffuse Interface in a Critical Fluid Mixture”. In: *The Journal of Chemical Physics* 50.9 (1969), pp. 3677–3693.

[41] Mark James Abraham et al. “GROMACS: High performance molecular simulations through multi-level parallelism from laptops to supercomputers”. In: *SoftwareX* 1–2 (2015), pp. 19 –25.

[42] B. Widom. “Surface Tension and Molecular Correlations near the Critical Point”. In: *The Journal of Chemical Physics* 43.11 (1965), pp. 3892–3897.

[43] D. Beysens and M. Robert. “Thickness of fluid interfaces near the critical point from optical reflectivity measurements”. In: *The Journal of Chemical Physics* 87.5 (1987), pp. 3056–3061.

[44] Jason Mick et al. “GPU-accelerated Gibbs ensemble Monte Carlo simulations of Lennard-Jonesium”. In: *Computer Physics Communications* 184.12 (2013), pp. 2662 –2669.

[45] W. J. Briels and H. L. Tepper. “Crystal Growth of the Lennard-Jones (100) Surface by Means of Equilibrium and Nonequilibrium Molecular Dynamics”. In: *Phys. Rev. Lett.* 79 (25 1997), pp. 5074–5077.

[46] Ulf R. Pedersen, Felix Hummel, and Christoph Dellago. “Computing the crystal growth rate by the interface pinning method”. In: *The Journal of Chemical Physics* 142.4 (2015), p. 044104.

[47] Vikram Thapar and Fernando A. Escobedo. “Extensions of the interfacial pinning method and application to hard core systems”. In: *The Journal of Chemical Physics* 141.12 (2014), p. 124117.

# Chapter 3

# Supervised Machine Learning of Binary Off-lattice Systems for Prediction of Phase Separation

## 3.1 Introduction

Machine learning has been greatly successful in predicting phase transitions in physics. Recently, the convolutional neural network (ConvNet or CNN), one of popular deep learning models, can effectively predict phase transition of two-dimensional Ising model utilizing local positions of spins in lattice.[1] Beyond the Ising model, when one tries to apply the ConvNet to more general systems such as three dimensional off-lattice systems, followings are considerable; what data is fed to machine learning and how to set an effective ML model up. To solve those questions, we develop a machine learning scheme based on the ConvNet to systematically construct a good ML model and confirm the model comparing the results of two binary off-lattice models of which phase separation diagrams are available from previous simulation studies.

With the growth of deep learning tools and recent developments of graphics processing unit

(GPU), the new idea of phase prediction by ML have been widely applied from simple toy models to complex systems.[2] Moving toward applications of off-lattice models from the Ising model, one must decide how the positions of molecules are fed into the neural network. Wei and Chen[3] pointed out that, while spin labels in Ising model represents spatial locations, input data of complex systems such as liquid crystals should be defined in a standard way of constructing correlations of index, position, and component of molecules. Naively, one can adopt an image recognition idea by digitizing the continuum space into a grid and assigning a value of "occupied" or "unoccupied" to a particular grid point, describing the occupancy of atoms and atom identity for detection of polymer states and crystal structures of Lennard Jones particle and water.[4, 5]

Beside raw positions, input ML data can be constructed with structural descriptors or features. The choice of features depends on what kind of ML models is used and what kinds of properties are interested in, but structural order parameters are mostly chosen such as distance, bond, and angle histograms.[6, 7, 8] In the case of off-lattice models, Jadrich and coworkers used a set of close distances of neighbors as the feature of phase transition.[9, 10] However, maximum distance criteria of two molecules chosen as a phase transition feature is system-specific and distance computation is expensive, thus becomes vulnerable when long-ranged correlation dominates phase transition of system such as the Widom-Rowlinson (WR) model. Alternatively, the learning-by-confusion scheme can be considered so that it classifies phases utilizing the performance of the neural network after training with deliberately incorrectly labeled data.[11] In this work, we use raw positions of molecules for input ML data to avoid prior knowledge and, instead, the ConvNet will capture features of phase transition such as molecular positioning patterns by training.

Typically, the ConvNet has been a good choice of machine learning algorithms to capture local features of a pattern in phase transition of condensed matters. Although the tool as a supervised machine learning requires labelled data to train, it readily takes the advantage of spatial structure by doing the convolution of relatively small size feature maps with coordinate images. ConvNet studies show a highly accurate prediction of phase transition of 2D lattice models, e.g. ferromag-

netic Ising model,[1, 12] Hubbard model,[13, 14] XY model,[15] and Anderson model.[16, 17] Thus, it is worth to apply such a successful ML algorithm to the phase prediction of 3D off-lattice models as well.

In this paper, we develop a ML framework which relies on the ConvNet to do the task of identifying the phase separation point in binary mixture models: the WR model and a freely-jointed polymer blend. To provide molecular positions into a neural network learning process, we interpolate it into single values on grid points between -1 and 1. Then, we figure out the optimal ConvNet filter size, one of hyperparameters for ConvNet, in a systematic way to build a good machine learning model which is capable to predict phase transition points. We show the features of phase behaviors of two models which machine learns and a good agreement with phase boundary of two binary mixture models reported in past. We conclude with a discussion on general application and limitation of our scheme.

## 3.2 Convolutional neural network approach for phase separation of off-lattice systems

We describe our machine learning scheme including data pre-/post-processing. (see Figure 3.1) We consider coordinates of a binary mixture of $A$ and $B$ components with the total number of molecules $N$ and the mole fraction of $A$, e.g. $x_A$. For the simplicity of explanation, we focus on the WR model that shows phase separation behavior as density ($\rho = N/V$ where $V$ is simulation cell volume) increases.

In brief, our supervised machine learning scheme consists of the following procedures. Once we obtain equilibrium (continuum) coordinates of molecules from molecular simulations at various densities and a certain $x_A$, we do data pre-processing to convert coordinates into a three dimensional color map in an appropriate format for the convolution neural network. Finding the optimal size of feature map for an effective ML model, machine learning is able to properly predict

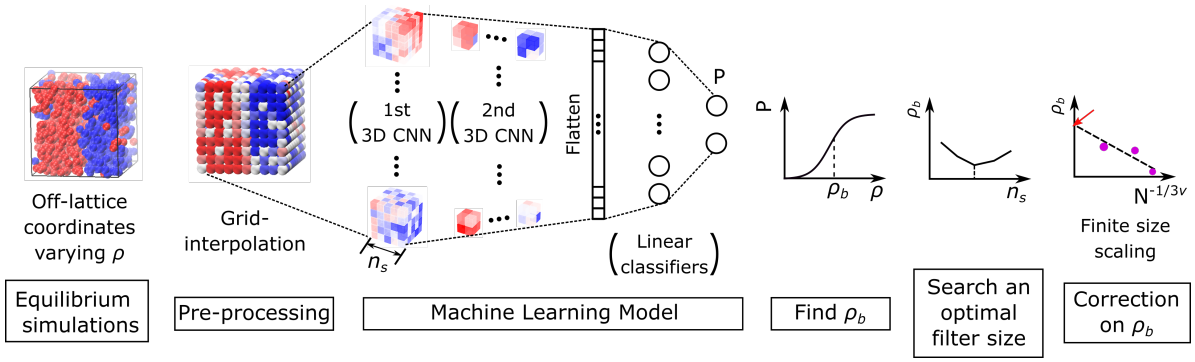


Figure 3.1: The Supervised machine learning scheme from equilibrated coordinates of the WR model with various densities ($\rho$) to get the corrected transition density (red arrow on the rightmost graph) using finite size scaling method at a given mole fraction. Details are described in Sec. 4.2.3.

a (finite-size) transition density at $x_A$ for a system size $N$. Finally, using transition densities with different $N$'s, we can estimate the corrected coexisting density at $x_A$ via finite-size scaling method.

Let us go over details of construction of input ML data. Molecular simulations at various densities and mole fractions output coordinates of molecules at equilibrium. Unlike lattice models, coordinates of off-lattice models have continuous values. Rather than taking continuum values as input, we interpolate both the molecular positions and components into values in single column, which allows to reduce data dimension for efficiency. For assignment of values on grids, we apply a three-dimensional linear interpolation by triangulating the coordinates with three values, such as 1 for $A$ molecules, 0 for $B$ molecules, and 0.5 for vacant on grids. As a result, a 3d image for $i$-th simulation output has a set of values in a range between 0 and 1, which is, in mathematical expression for a given density and mole fraction of $A$,

$$S_i\left(\rho, x_A\right) = \left[s_1, \cdots s_{{n_g}^3}\right] \tag{3.1}$$

where $n_g$ is the number of grids on an axis. We choose $n_g$ which is close to $\sqrt[3]{N}$ for simplicity.

When converting raw positions of particles into 3d images with any value between 0 and 1, we split the collection of data depending on data set purposes; training CNN neural network and predicting the probability of immiscible phase. We train our neural network with $S$'s at two density

far from phase transition density. We do not know where phase transition density is located exactly yet and instead we can easily figure out which phase dominates at an very high and low density in our eye. At those extreme temperatures, we are able to label on the system with the dominated phase, e.g. mixing or separation which digitized as 0 and 1. As a result, the training data set $X_{known}$ would be a set of $j$ images with the known $j$ labels at two different temperatures;

$$X_{known} = [S_1(\rho_{mix}), \quad \cdots, \quad S_j(\rho_{sep})] \tag{3.2}$$

where $\rho_{mix}$ and $\rho_{sep}$ are the densities where mixing and separation phase clearly dominates, respectively. The rest of images at other densities between $\rho_{mix}$ and $\rho_{sep}$ will be used for the prediction of phase transition;

$$X_{unknown} = [S_{j+1}(\rho_1), \quad \cdots, \quad S_k(\rho_m)] \tag{3.3}$$

where $m$ is total number of images for various $\rho$'s at $x_A$.

The supervised machine learning algorithm mainly goes two steps: training and prediction. In training step, our goal is to obtain an optimized neural network model ($F$) that contains many weights and biases to predict correct phases for training data set;

$$F(X_{known}) = Y_{labels} = [0, \quad \cdots, \quad 1] \tag{3.4}$$

. Note that we use 1 and 0 for mixing and separation phase of the PB model. Our ML model consists of two CNN layers and two linear classifier layers. CNN layers have $n_f$ feature maps (or filters) to capture relatively small patterns on image. The $i$-th 3D feature map contains a set of weights with a shape of $n_s$ x $n_s$ x $n_s$, and and single bias $b_i$, where $n_s$ is the filter size. Next to CNN layers, at least two linear classifier layers with weights and $n_p$ scalar-valued bias will finally predict the probability of mixing and separation phase, $P(\rho)$ activated by Softmax function. Those weights and biases will be optimized by minimizing loss function with training data set by the

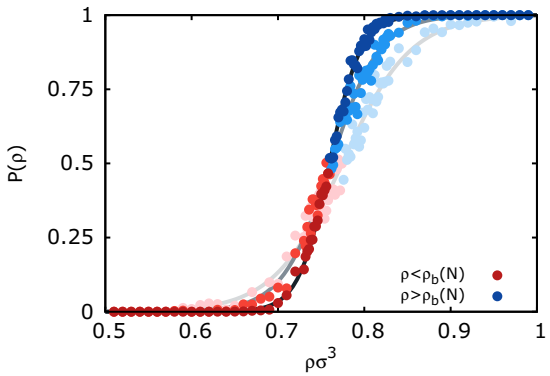


Figure 3.2: Probability distributions of finding separation phase, P($\rho$), as a function of system density for Widom-Rowlinson model with $N = 1024$ (lightest colors), 2048, 4096 (darkest colors) at $x_A = 0.3125$ using filter size $n_s = 4$. We define the system density with 50% probability of separation as $\rho_b(N)$. Solid lines are results of fitting to sigmoid curve.

backpropgation algorithm. In prediction process, the trained ML model, e.g. $F$ in Eq. 3.4 will use the prediction data set $X_{unknown}$ like $F\left(X_{unknown}\right) = Y_{predict}$ where $Y_{predict}$ is a set of probability of phases for images in a range of [0,1]. Then, the (finite) transition density, $\rho_b(N)$, can be inferred by fitting the probability distribution as a function of densities with sigmoid function as shown in Figure 3.2.

Unlike parameters (weights and biases) of machine learning are optimized with training set, hyperparameters such as $n_s$, $n_f$, and $n_p$ have to be determined in prior machine learning. The filter size $n_s$ determines the correlation or patterning range of small spatial features to help to predict phase separation. Many studies of predicting phase transition of simple models used very small values such as 2 or 3 for $n_s$.[1, 12, 18, 19, 14] Such a tiny feature map could be enough for studying the phase behavior of lattice models because interaction is very weak such as interacting adjacent neighbors for Ising model. At least for the Widom-Rowlinson model, a small size of feature map seems not to work because of their long range correlations.[10]. Using too large $n_s$ would become worse because a large feature map would contain extra, unnecessary weights to force training and give a slow learning rate. That is why we develop a scheme to find an appropriate hyperparamter, filter size $n_s$ for complex systems.

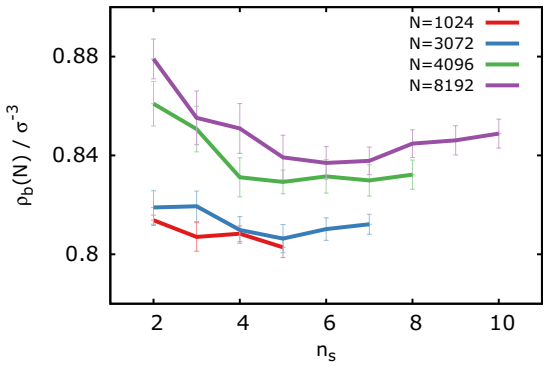


Figure 3.3: The V-shape trends of phase transition densities with a function of CNN filter size $n_s$ at $x_A = 0.125$ of the WR model.

The choice of the filter size $n_s$ affects on prediction quality. To see the dependency of $n_s$ on predicted transition points, we get transition points varing from 2 to the maximum size of patterns, e.g. $\frac{n_g}{2}$ because of periodic boundary condition. As you can see Figure 3.3, the V-shaped trend suggests two scenarios. Too small filter size would be weak to hold pattern information of such a strong correlation of spatial distribution of molecules, which gives bias error because of too simple ML model. In contrast, because additional unrelated colors would disturb learning patterns and increase variance error, the optimized ML model with too large $n_s$ would be be vulnerable. Thus, we choose the $n_s$ which has the lowest transition density in V-shaped trend. In the case of the PB model, we see an inverse V-shaped trend and choose the highest transition temperature. Note that we keep other hyperparameters $n_f$ and $n_p$ constant for simplicity.

Once we decide the transition density varying $n_s$, we can extrapolate the transition density for infinite system using finite-size scaling (FSS).[20, 21, 22] Because transition density is suppressed in finite systems, the scaling method provides the way to correct the transition density without finite size effect, $\rho(N = \infty; x_A)$;

$$\rho_b(N) - \rho_b(\infty) \sim L^{-1/\nu} \sim N^{-1/3\nu} \tag{3.5}$$

where $\rho_b(N)$ and $\rho_b(\infty)$ are the transition density of the finite and infinite system, respectively.

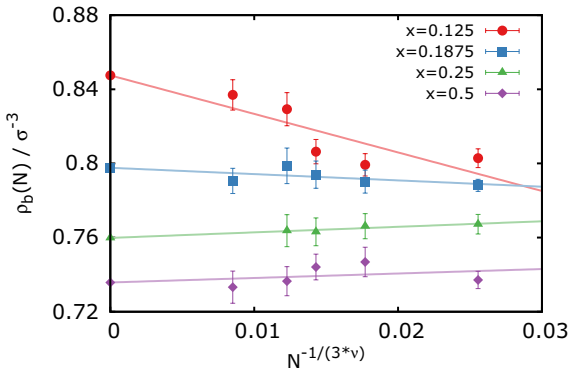


Figure 3.4: The system size dependence on transition densities of the WR model predicted by machine learning. The infinite transition densities $\rho(\infty)$'s (or $\rho_b$ in Fig. 3.7) are extrapolated as y-intercepts by finite-size scaling method with universal critical exponents, $\nu = 0.63012$.[23]

Also, $L$ is the cell length in the simulation, and $\nu$ is a universal exponent, e.g. 0.63012 for 3D Ising universality class.[23] The results using FSS method for the WR model are shown in Fig. 3.4.

For a specific case with intermediate (plausible) phases during transition, we need to reset $T_{sep}$ as you can see our polymer blend model. For example of lamella transition, one may expect phase separation transition smoothly occurs from lamellar structure to disordered phase, but we found several intermediate structures during phase separation transition; perforated lamellar, two dimensional channels, three dimensional channels, and then mixing phase. In fact, these partially transformed network structures are plausible and appear instantly (not to form macro-phase). Thus, if the structures appear frequently in coordinates and supervised machine learning learns only lamellar and mixing structure, the predicted transition temperature would not feasible due to not learned shape. In particular, we found considerable proportion of plausible domain structures at intermediate temperatures with $0.375 \leq x_A \leq 0.5$. To solve such multi-structure problem, we employ an additional training set with the coordinate which has three dimensional percolating channels (3C). Using three categories (lamellar, mixing, and 3C) in ML, we can roughly estimate a temperature where 3C structure mostly appears.

In Fig. 3.5, we plot probability of three phases as F($X_{known}$) is either 0, 1, or 2 for separation, mixing, and 3C phase. While the training sets are chosen as coordinates which of $T_{sep}$ = 1.0 and

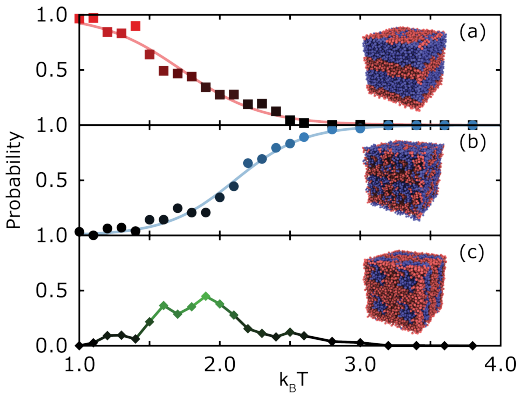


Figure 3.5: The probability of finding (a) lamellar structure, (b) mixing phase, and (c) three dimensional channel (3C) with respect to system temperature for $x_A = 0.4375$ and $N = 64$ of polymer blend model. Due to the appearance of such a plausible, intermediate structure, we consider phase separation transition for systems would be a (b)-(c) transition (3C to mixing phase) for our ML detection of phase boundary, instead of lamella-mixing transition. The example images for training data with 2x2x2 supercell are shown on right side.

4.0, single coordinate which has 3C phase in eye is used for 3C phase. Then, we generate the total number of the 3C (augmented) images will be the same as the amount of other training sets to avoid data amount bias. Varying the filter size of the first CNN layer, we find the optimal filter size which shows maximum probability of 3D channel to distinguish 3C phase. With the optimal filter size, we can get a new $T_{sep}$ where maximum probability of 3D channel phase locates. As you see Fig. 3.5, the $T_{sep}$ is 1.9 for $x_A$ = 0.435 and N = 64 which will be used for obtaining the transition temperature.

With the new $T_{sep}$ and $T_{mix}$ for $0.375 \leq x_A \leq 0.5$, we train a new ML model with two outputs (0 or 1 for 3C and mixing phase) in order to obtain the transition temperature between 3C phase and mixing phase by varying the first CNN filter size. Note that for other concentrations $x_A <$ 0.375, we use $T_{sep}$ = 0.6 - 1.0 without considering intermediate phases. Also, we do the FSS method for some system sizes to extrapolate $T_b(\infty)$.

## 3.3 Computational details

We study the phase classification of off-lattice models, labeling configurations as belonging to either mixing or separation phases. Our goal is to answer the question whether supervised machine learning with our bias-training method is capable of correctly classifying two phases of continuum models; the Widom-Rowlinson mixture and a symmetric blend of freely jointed polymer chains.

The Widom-Rowlinson (WR) model is a binary (A/B) mixture model which shows phase separation under low density and mixing at high density. Their interactions are governed by a kind of species; overlapping between same species are available without energy cost, otherwise different species are repulsive within distance $\sigma$ like hard sphere model. We prepared 100 ensembles per temperature per concentration, which initially have randomly distributed particles in cubic cell with $N = 1024$, $2048$, $3072$, $4096$, and $8192$ where $N$ is total number of particles. We employ standard Monte Carlo simulation methods to run up to $\sim$ 7 x $10^5$ MC steps per number of particles at 7 different concentrations, $x_A = N_A/N = [0.125, 0.1875, 0.25, 0.3125, 0.375, 0.4375, 0.4863, 0.5]$, and at least 51 number densities ranging from $\rho$ = 0.5, 0.51, ..., 0.75, 0.752, ..., 0.82, 0.83, ..., 1.0 $\sigma^{-3}$ where $V$ is the cell volume. The WR particles can move within $\sigma$ distance except overlapping with different species under periodic boundary condition.

We test our ML scheme for not only Widom-Rowlinson model but also a symmetry polymer blends (PB) model. The model shows the upper critical separation temperature (UCST) behavior as a function of temperature and mole fraction under constant pressure. The symmetric polymer blend model we used is composed of binary components (A/B) with freely jointed polymer chains. We consider a system that each polymer has 32 sites of mass $m$. Along the chain backbone, neighbor beads are connected under a harmonic spring potential and all other beads interacts a cut-and-shifted Lennard-Jones (LJ) potential, that is, the non-bonding potential is shifted to be zero at any distance greater than $2.5\sigma$. As for non-bonding interactions of beads, we use following LJ parameters, $\sigma_{A-A} = \sigma_{A-B} = \sigma_{B-B} = \sigma$, $\varepsilon_{A-A} = \varepsilon_{B-B} = \varepsilon$, and $\varepsilon_{A-B} = 0.9\varepsilon$ (see details in

Gromov and de Pablo's paper).[24] We run 30 simulations from 64 molecules up to 128 molecules for each temperature and mole fraction, $x_A$ = [0.125, 0.1875, 0.3175, 0.375, 0.4375, 0.5 ] by randomly inserting polymers on a cubic lattice at a large cell volume.

We perform molecular dynamics simulations of polymer molecules using GROMACS 5.1.2 software package[25] at a range of reduced temperature ($\sim$ 25 reduced temperatures we use) from 0.6 $k_BT$ to 4.0 $k_BT$. Note that below 0.6 $k_BT$ the system becomes freezing, thus we avoid those temperatures due to inaccessible to equilibrium. We run the isothermal-isobaric (NPT) simulations using a Nose-Hoover thermostat and a Parrinello-Rahman barostat with pressure $P = 1\sigma^{-3}$. The system is propagated using the Verlet integration with a reduced time step of 0.004 $\sigma\sqrt{m^{-1}}$. Once we get stable densities from NPT simulations with $3 \times 10^6$ time steps, we perform isothermal-isochoric (NVT) ensemble simulations up to $10^8$ time steps to obtain equilibrium coordinates.

In pre-processing of coordinates, we do three-dimensional grid interpolation with linear interpolation by assigning values for A and B particles and vacant grids; 1, 0, 0.5 for the WR model and 1, 0, -1 for the polymer blends model, respectively. In addition, with few tens or hundreds of coordinates, optimization of $\sim$ 200,000 parameters of ML model might be unfeasible to train ML models. To enlarge the amount of coordinates, we produce virtual coordinates using an augmentation method which generates a number of data sets by flipping, translating, and rotating images. We make 100 and 400 augmented images per original image for training dataset of the WR model and the PB model. We make 10 augmented images per original image for the prediction data of the PB model as well. We implement these pre-processings with the Scipy intepolation library.[26]

Our convolutional neural network (CNN) is trained to minimize a loss function, standard cross entropy function. Our data are composed of a set of coordinates obtain at number density 0.5 - 1.0 number densities for the WR model and 0.6 - 4.0 reduced temperatures for mixing phase of PB model. The weights and biases of our CNN model are then optimized through back-propagation with Adam algorithm[27, 28] to minimize the loss function on the training data during 30 epoches through entire dataset with every 200 and 50 images per batch for the WR model and the PB

model, respectively. Our ML model takes grid-interpolated color maps with periodic 3D padding as input data. Utilizing the successful ML model architecture for critical exponents of 2D electron system,[29] we use two CNN layers with 16 filters (e.g. $n_f = 16$) and vary filter size for first CNN layer to find the optimal size, but keep $n_s = 2$ for second CNN layer. All scores as outputs of CNN layers are activated by rectified linear (ReLu) activation function, e.g. $f(x) = \max(0, x)$. Through linear classifier layers with $n_p = 256$, we utilize the normalized exponential function (called softmax function) to get a set of the probability of mixing and separation phase. We implement the networks with the Keras library using the Tensorflow backend.[30]

## 3.4 Results and discussions

The general procedures of how CNN works for a problem such as phase separation is that one can visualize the weights of CNN filters, which were also shown in studies of lattice models. In Fig. 3.6, we found there are roughly two types of CNN filters that show the spatial gradient of weights and random weight parameter distributions, which is good agreement with previous studies of lattice models.[19]. Interestingly, when sorted in ordering of bias, the filters indicates that most of filters which have two large domains of weights even small filter size are likely to have a high bias. This is because, when the weight distribution of filters matches to distribution of particles in a cell, convolution calculation comes out a high score. Then, the score will be corrected by adding bias and only positive score will be fed to the next ML layer. The high positive value is likely to conclude this system is under separation state as we set 0 as output for mixing phase and 1 for separated phase.

As mentioned in section 4.2.3, we independently train parameters of the ML model with data obtained at a certain mole fraction for single transition density, not certain density for single transition mole fraction. As mole fraction of the WR system increases, the separated domain forms sphere, cylinder, and lamellar structure, which is well known in gas-liquid transition of Lennard-

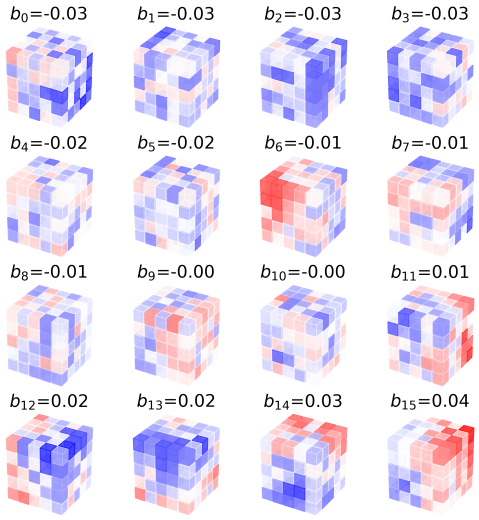


Figure 3.6: The sorted 3D color maps of weights of CNN filters by values of bias at $x_A = 0.5$ and $N = 1024$ of the WR model. Most of separation and mixing patterns can be found with high bias and low bias, respectively. Because CNN layers gives high scores by convolution (or matching) the pattern of images with filters, CNN filters shows characteristics of separation and mixing patterns within optimal filter size. For convenience, red to blue colors of voxels correspond normalized weights in a range of -1 and 1 obtained by the largest magnitude of weights of all CNN filters.

Jone particles.[31] The domain shape dependency gives us to input simulation data under constant mole fraction into ML rather than under constant density. Under constant density, the data will have four different spatial patterns from mixing to lamella shape, which may require at least four classifiers for prediction accuracy. Thus, we choose to use data under constant mole fraction but various densities. As you can see in Fig. 3.7, our ML results of Widom-Rowlinson model shows excellent agreement with previous simulation studies.[32, 33] Also, Fig. 3.8 shows the result of polymer blend models agrees with previous simulation studies.

## 3.5 Conclusions

We have presented a machine learning framework fed by coordinates of molecular simulations for obtaining the phase diagram of off-lattice models. To apply convolutional neural network (CNN) for detection of phase transition, our idea is that we choose a good CNN filter size by checking

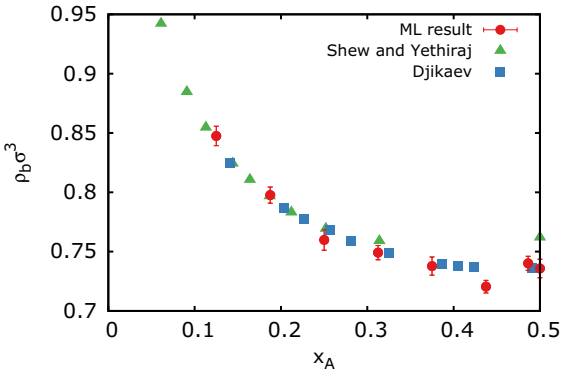


Figure 3.7: Phase diagrams of the WR model from our work and compared with that from simulation studies of Shew and Yethiraj[32] and Djikaev.[33] Error bars are the standard deviations for (finite) transition density for the largest system size.

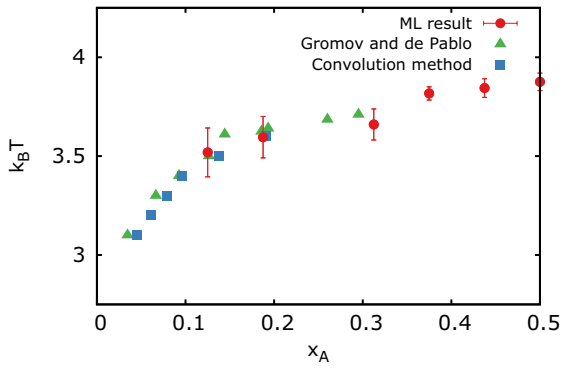


Figure 3.8: Phase diagram of polymer blends model from our work and compared with that from simulation studies of Gromov and de Pablo[24] and Jung and Yethiraj.[34] Error bars are the largest standard deviations for $N$'s.

the V-shaped dependency of predicted phase transition point with various filter sizes. Our ML results for Widom-Rowlinson model and a freely-jointed symmetric polymer blend model show good consistency with results of previous simulation studies.

When applying our supervised machine learning for phase behavior studies of complex systems, the input data is necessary to be constructed to contain two neighboring phases. Multi-phase transition of block copolymer solution or aqueous surfactants can have three or more phases at a fixed concentration and various temperatures; disordered (D), cylinder (C), gyroid (G), lamellar (L) phase for block copolymer solution. To work the ML method, the input data consists of coordinates in D and C, C and G, or G and L to get transition temperature for D-C, C-G, or G-L, respectively. Also, we believe three or more component systems may be studied as extension of our ML method. The color map for three components system can be represented by three kinds of color maps for pairs of components, e.g. component 1/2, 2/3, and 1/3 pairs.

However, to apply other systems, the good choice of not only some hyperparameters such as $n_f$ and $n_p$ but also ML architectures such as the number of layers seems to be somewhat trial-error. We take a ML model for the phase prediction of a quantum 2D model[29], but it is not easily transferred to other cases. One way to construct a good ML model is to manually try reasonable values depending on the complexity of systems to show good agreement with reference using another method such as Gibbs ensemble simulation,[35, 36, 37, 38, 39] Gibbs-Duhem techniques,[40, 41, 42, 43] and Convolution method.[34] Usually, a deeper ML architecture is considerable for prediction of two more phases in complicate systems. The phase prediction of the 2D Ising model was done by single CNN layer with 64 2x2 filters.[1] In the WR model, a deeper ML with at least two CNN layers should be necessary from our preliminary result of single CNN layer. To reduce the effort of finding a ML architecture, automated ML (AutoML) techniques are recently developed such as Cloud AutoML by Google and AutoKeras by DATA Lab at Texas A&M University[44] because it automatically tune deep neural networks by searching ML algorithms.

One of challenges to apply ML technique utilizing molecular simulation data is that running

numerous simulations is not cheap. While it is open question about how many amount of input data is necessary for scientific research, the amount of simulation data is usually limited due to computation performance and resources. In case of the WR model, we simulate at least 5100 simulations per system size per concentration, which means at least $\sim$ 15,000 runs with three system sizes to get single point on phase boundary. The estimated time would be about 10 days for Intel Core i7 6-core processor with base frequency 3.2 GHz when using 6 processors.

Beside, running molecular dynamics of polymers would be serious. In this work, we use GPU-supported GROMACS software to speed up. It takes 280 minutes for single run with 64 polymer molecules when using single NVIDIA GTX 1080 GPU and 2 Intel Xeon CPU cores. Because we run at least 1400 simulations for two system sizes per concentration, total wall-time would be $\sim$ 272 days with single GPU. This lead us to be granted for powerful GPU resources such as Summit located at the Oak Ridge Leadership Computing Facility. Compared with performance with NVIDIA GTX 1080, the result from our benchmark shows that simulation speed increases by almost two times when using single NVIDIA Tesla V100 SXM2 GPU and 7 cores of Power9 CPU. In addition, Summit cluster is a good resource in that up to a few tens of thousands of GPUs is available. Instead of using a few hundreds of GPUs, it might be considerable to alternatively use transfer learning method with even relatively small amount of simulation data.[45] The idea is to transfer the well pre-trained knowledge in a certain domain to solve closely related problems. There is a few recent transfer learning studies for phase prediction of 3D Hubbard model[14] and axial next-nearest-neighbor Ising model,[46] thus transfer learning studies would be interesting when utilizing the universality of phase transition behavior.

# References

[1] Juan Carrasquilla and Roger G. Melko. “Machine learning phases of matter”. In: *Nature Physics* 13 (2017), 431 EP –.

[2] Lorenza Saitta and Michele Sebag. “Phase Transitions in Machine Learning”. In: *Encyclopedia of Machine Learning*. Ed. by Claude Sammut and Geoffrey I. Webb. Boston, MA: Springer US, 2010, pp. 767–773.

[3] Michael Walters, Qianshi Wei, and Jeff Z. Y. Chen. “Machine learning topological defects of confined liquid crystals in two dimensions”. In: *Phys. Rev. E* 99 (6 2019), p. 062701.

[4] Ryan S. DeFever et al. “A generalized deep learning approach for local structure identification in molecular simulations”. In: *Chem. Sci.* 10 (32 2019), pp. 7503–7515.

[5] Qianshi Wei, Roger G. Melko, and Jeff Z. Y. Chen. “Identifying polymer states by machine learning”. In: *Phys. Rev. E* 95 (3 2017), p. 032504.

[6] Philipp Geiger and Christoph Dellago. “Neural networks for local structure detection in polymorphic systems”. In: *The Journal of Chemical Physics* 139.16 (2013), p. 164105.

[7] Hideo Doi et al. “Machine learning-aided analysis for complex local structure of liquid crystal polymers”. In: *Scientific Reports* 9.1 (2019), p. 16370.

[8] E. D. Cubuk et al. “Identifying Structural Flow Defects in Disordered Solids Using Machine-Learning Methods”. In: *Phys. Rev. Lett.* 114 (10 2015), p. 108001.

[9] R. B. Jadrich, B. A. Lindquist, and T. M. Truskett. “Unsupervised machine learning for detection of phase transitions in off-lattice systems. I. Foundations”. In: *The Journal of Chemical Physics* 149.19 (2018), p. 194109.

[10] R. B. Jadrich et al. “Unsupervised machine learning for detection of phase transitions in off-lattice systems. II. Applications”. In: *The Journal of Chemical Physics* 149.19 (2018), p. 194110.

[11] Evert?P ?L van Nieuwenburg, Ye-Hua Liu, and Sebastian?D Huber. “Learning phase transitions by confusion”. In: *Nature Physics* 13.5 (2017), pp. 435–439.

[12] Akinori Tanaka and Akio Tomiya. “Detection of Phase Transition via Convolutional Neural Networks”. In: *Journal of the Physical Society of Japan* 86.6 (2017), p. 063001.

[13] Peter Broecker et al. “Machine learning quantum phases of matter beyond the fermion sign problem”. In: *Scientific Reports* 7.1 (2017), p. 8823.

[14] Kelvin Ch’ng et al. “Machine Learning Phases of Strongly Correlated Fermions”. In: *Phys. Rev. X* 7 (3 2017), p. 031038.

[15] Philippe Suchsland and Stefan Wessel. “Parameter diagnostics of phases and phase transition learning by neural networks”. In: *Phys. Rev. B* 97 (17 2018), p. 174435.

[16] Tomi Ohtsuki and Tomoki Ohtsuki. “Deep Learning the Quantum Phase Transitions in Random Electron Systems: Applications to Three Dimensions”. In: *Journal of the Physical Society of Japan* 86.4 (2017), p. 044708.

[17] Tomohiro Mano and Tomi Ohtsuki. “Phase Diagrams of Three-Dimensional Anderson and Quantum Percolation Models Using Deep Three-Dimensional Convolutional Neural Network”. In: *Journal of the Physical Society of Japan* 86.11 (2017), p. 113704.

[18] Patrick Huembeli, Alexandre Dauphin, and Peter Wittek. “Identifying quantum phase transitions with adversarial neural networks”. In: *Phys. Rev. B* 97 (13 2018), p. 134109.

[19] Philippe Suchsland and Stefan Wessel. “Parameter diagnostics of phases and phase transition learning by neural networks”. In: *Phys. Rev. B* 97 (17 2018), p. 174435.

[20] Kurt Binder and DP Landau. “Finite-size scaling at first-order phase transitions”. In: *Physical Review B* 30.3 (1984), p. 1477.

[21] JT Chayes et al. “Finite-size scaling and correlation lengths for disordered systems”. In: *Physical review letters* 57.24 (1986), p. 2999.

[22] Nigel B. Wilding. “Critical-point and coexistence-curve properties of the Lennard-Jones fluid: A finite-size scaling study”. In: *Phys. Rev. E* 52 (1 1995), pp. 602–611.

[23] Massimo Campostrini et al. “25th-order high-temperature expansion results for three-dimensional Ising-like systems on the simple-cubic lattice”. In: *Phys. Rev. E* 65 (6 2002), p. 066127.

[24] Dmitry G. Gromov and Juan J. de Pablo. “Phase equilibria in binary polymer blends: Integral equation approach”. In: *The Journal of Chemical Physics* 109.22 (1998), pp. 10042–10052.

[25] Mark James Abraham et al. “GROMACS: High performance molecular simulations through multi-level parallelism from laptops to supercomputers”. In: *SoftwareX* 1-2 (2015), pp. 19 –25.

[26] Eric Jones, Travis Oliphant, Pearu Peterson, et al. *SciPy: Open source scientific tools for Python*. [Online; accessed ]. 2001–.

[27] Diederik P. Kingma and Jimmy Ba. *Adam: A Method for Stochastic Optimization*. 2014.

[28] Sashank J. Reddi, Satyen Kale, and Sanjiv Kumar. “On the Convergence of Adam and Beyond”. In: *International Conference on Learning Representations*. 2018.

[29] Zhenyu Li, Mingxing Luo, and Xin Wan. “Extracting critical exponents by finite-size scaling with convolutional neural networks”. In: *Phys. Rev. B* 99 (7 2019), p. 075418.

[30] François Chollet et al. *Keras*. `https://keras.io`. 2015.

[31] Kurt Binder et al. “Beyond the Van Der Waals loop: What can be learned from simulating Lennard-Jones fluids inside the region of phase coexistence”. In: *American Journal of Physics* 80.12 (2012), pp. 1099–1109.

[32] Chwen-Yang Shew and Arun Yethiraj. “Phase behavior of the Widom–Rowlinson mixture”. In: *The Journal of Chemical Physics* 104.19 (1996), pp. 7665–7670.

[33] Yuri Djikaev. “The interfacial tension and phase diagram of the Widom-Rowlinson mixture via Monte Carlo simulations”. In: *The Journal of Chemical Physics* 128.1 (2008), p. 014712.

[34] Hyuntae Jung and Arun Yethiraj. “A simulation method for the phase diagram of complex fluid mixtures”. In: *The Journal of Chemical Physics* 148.24 (2018), p. 244903.

[35] A.Z. Panagiotopoulos et al. “Phase equilibria by simulation in the Gibbs ensemble”. In: *Molecular Physics* 63.4 (1988), pp. 527–545.

[36] B de Smit, Ph De Smedt, and D Frenkel. “Computer simulations in the Gibbs ensemble”. In: *Molecular physics* 68.4 (1989), pp. 931–950.

[37] Athanassios Z Panagiotopoulos. “Direct determination of fluid phase equilibria by simulation in the Gibbs ensemble: a review”. In: *Molecular simulation* 9.1 (1992), pp. 1–23.

[38] KK Mon and Kurt Binder. “Finite size effects for the simulation of phase coexistence in the Gibbs ensemble near the critical point”. In: *The Journal of chemical physics* 96.9 (1992), pp. 6989–6995.

[39] Mohammadhasan Dinpajooh et al. “Accurate and precise determination of critical properties from Gibbs ensemble Monte Carlo simulations”. In: *The Journal of chemical physics* 143.11 (2015), p. 114113.

[40] David A Kofke. “Gibbs-Duhem integration: a new method for direct evaluation of phase coexistence by molecular simulation”. In: *Molecular Physics* 78.6 (1993), pp. 1331–1336.

[41] A Van’t Hof, CJ Peters, and SW De Leeuw. “An advanced Gibbs-Duhem integration method: Theory and applications”. In: *The Journal of chemical physics* 124.5 (2006), p. 054906.

[42] R Schuhmann Jr. “Application of Gibbs-Duhem equations to ternary systems”. In: *Acta Metallurgica* 3.3 (1955), pp. 219–226.

[43] Fernando A Escobedo and Juan J de Pablo. “Pseudo-ensemble simulations and Gibbs–Duhem integrations for polymers”. In: *The Journal of chemical physics* 106.7 (1997), pp. 2911–2923.

[44] Haifeng Jin, Qingquan Song, and Xia Hu. *Auto-Keras: An Efficient Neural Architecture Search System*. 2018.

[45] S. J. Pan and Q. Yang. “A Survey on Transfer Learning”. In: *IEEE Transactions on Knowledge and Data Engineering* 22.10 (2010), pp. 1345–1359.

[46] Askery Canabarro et al. “Unveiling phase transitions with machine learning”. In: *Phys. Rev. B* 100 (4 2019), p. 045129.

# Chapter 4

# Entropy-driven Phase Separation Behaviors of Poly(ethylene oxide) in C2 Methylated Imidazolium Ionic Liquids: A Molecular Simulation and Deep Neural Network Study

## 4.1 Introduction

There has been considerable interest in ionic liquids (ILs) due to their unique properties such as low melting points and large liquid range with high thermal stability and a low vapor pressure.[1, 2, 3, 4, 5] As a mechanical supporter for IL-based systems, polymers in ILs have potentially wide application such as fuel cells, temperatures-sensitive sensor, electromechanical actuators, gas permeation membrane, and batteries.[6, 7, 8, 9, 10, 11] Especially, poly(ethyelen oxide) or PEO is a polymer used in wide variety of applications ranging from biomedical to viscosity modifications.[12, 13, 14, 15] To realize hybrid systems composed of PEO and ILs, understandings of its miscibility is necessary. In this work, we use molecular dynamics simulations and deep neural

network techniques to study modification effects of ionic liquid cations on the miscibility behavior of PEO/IL mixtures.

Incorporation of ILs with PEOs can result in lower critical solution temperature (LCST) behavior. The LCST behavior is that, above critical point, a homogeneous solution of polymer separates into the two equilibrium phases; polymer-rich phase and solvent-rich phase. In such LCST systems, the phase separation is driven by the unfavorable entropy of mixing and is mainly caused by directional interactions. Typically, hydrogen bonding between unlike components interferes with the rotational freedom. At low temperatures, the predominant species feel attractive with unlike segments with many rotational degrees of freedom effectively frozen out. For higher temperatures, the orientations will be essentially random and the like intermolecular forces will dominate, possibly leading to entropic driven LCST behavior.

These LCST behaviors of various PEO/ILs have been experimentally studied in terms of hydrogen bonding. Watanabe et al. investigated the LCST phase behavior of different polyethers in various classes of ILs.[16] They showed that polyethers are miscible in imidazolium- and pyridinium-based ILs, whereas they were insoluble in the ammonium- and phosphonium-based ILs. For a given IL, LCST increases with the polarity of polyethers and decreases by replacing the hydrogen atom on imidazolium cation by an alkyl group. Lodge et al. studied the LCST phase behavior of poly(ethylene glycol) or PEG in imidazolium-based ILs containing different alkyl chain length of cation and polymer terminal group.[17, 18] They observed an increase in the cloud point temperature with the proportion of long alkyl chain of imidazolium in mixtures of two mixture. And lower molecular weights of PEG are likely to largely increase critical point rather than high molecular weights due to high portion of hydroxyl terminal group.

Also, these H-bonds on IL cation leads to peculiar dynamical phenomena near the phase separation of PEO/ILs. Li and Wu found during cooling process slightly blue-shift of unsaturated C-H's on imidazolium cations, then bounds back to red-shift of C-H during cooling through phase transition temperature.[19] The interesting behaviour could be explained due to the existence of

several hydrogen bonding types such as C2-H. When gradually forming the hydrogen bonds of unsaturated C-H with oxygen of PEOs, the H-bonds would reach saturation, then extra free [$BF_4$] anions tend to form another hydrogen bonds with cations which induce negative effect. Xiao and coworkers studied rheological behavior of PEO in [BMIM][$BF_4$] and [EMIM][$BF_4$].[20] They found a V-shaped dips of storage modulus with respect to temperature. They suggested that during heating the behavior might be a result of breaking of not only the H-bonds between PEO and ILs but also their heterogeneous associations such as hydrogen-bonded clusters as analogy to the PEO/water system.

By far, some theoretical studies have interested in asymmetric LCST behaviors of PEO/ILs using properties of pure components. White and Lipson used a lattice-based theory and investigated ideal and excess contributions for the overall entropy of mixing.[21] Comparing with typical polymer solvents or melts, they found that the stronger cohesive energy density and less free volume of IL component result in unfavorable entropic effects. Also, the aggregation of the IL component reduces the entropy of mixing. Nakamura studied spinodal decomposition of PEO/ILs with various theory levels.[22, 23] The result indicated that the dielectric constant difference between the polymer and the ionic liquid is essential to explain such the shift of the critical point toward polymer-rich regions, rather than hydrogen bonding effect. Because those studies focus on the pure component properties to explain the LCST behaviors, it is worth to discuss about how such the hydrogen bonding affects on mixture properties and connects to phase behaviors of PEO/ILs, which is still an open question.

Molecular simulation is a good tool to study the phase behaviors. For example, our previous study run atomistic simulations of PEO/ILs to see hydrogen bonding effect on phase behavior.[24] Although simulations are performed at two temperatures and single concentration of system, the result suggested that the phase separation is driven by the hydrogen bonding of C2-H on the imidazolium cation ring. However, such an molecular simulation with high degree of freedom would not appropriate for obtaining entire phase diagram due to slow performance. Especially near critical

point, the phase boundary is suppressed by finite system size effect. Therefore, molecular simulations of polymer solution typically obtain phase coexistence compositions at temperatures far from the critical point using slab geometry.[25] Also, for accurate and fast performance, such an coarsed modeling would be good such as united-atom modeling framework under symmetry-adapted perturbation theory, called SAPT-UA.[26, 27]

To study IL effect on the critical point of PEO/ILs, deep neural network (DNN) technique is a possible solution for the prediction of phase diagram. Recently, DNN arises as a data-driven tool to solve previously unaccessible problems including extrapolating phase boundary. Neural networks (NNs), a class of DNN techniques, showed remarkably predictive power for phase behavior of multicomponent systems.[28, 29, 30, 31, 32, 33, 34] With collective variables from results of molecular simulations, NN can predict phases of system under a wide range of temperatures and compositions. Utilizing good quality of simulation data with improvements such as SAPT-UA force field and Convolution method,[25] we believe that the prediction of phase diagrams of polymer solutions becomes feasible.

Our hybrid way of a molecular simulation and a neural network technique is to investigate cation modification effects on phase behaviors of short PEO chains with tetrafluoroborate anion, [$BF_4$]. To see the C2-H hydrogen bond effect and N-alkyl chain length effect, we use four different cations such as 1-butyl-2,3-dimethylimidazolium [BMMIM], 1-butyl-3-methylimidazolium [BMIM], 1-ethyl-2,3-dimethylimidazolium [EMMIM], and 1-ethyl-3-methylimidazolium [EMIM]. [BMMIM] and [EMMIM] cations, e.g. [$C_n$MMIM] (n = 2,4), would effectively prevent the hydrogen bonding between an unsaturated C2-H on [$C_n$MIM] cation. (see the atomtype name in Fig. 4.1) With varius PEO/IL systems, we obtain collective properties in a wide range of temperature where it is observed from completely mixing phase to separation phase up to staring PEOs decomposition temperature, 580 K[35], and then predict phase boundaries of four PEO/IL mixtures via a neural network. We describe our force field and methology in next section, then discuss shifts on mixture properties and critical points by C2 methylation.

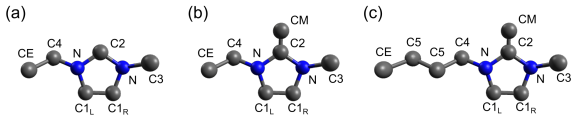


Figure 4.1: A picture of the definition of united atom types of (a) [EMIM], (b) [EMMIM], and (c) [BMMIM] cations.

## 4.2 Methods

### 4.2.1 The SAPT-UA force field for [$C_n$MMIM] cations

Following the force field development procedure described in our previous works[26, 27], we build united atom models of [BMMIM] and [EMMIM] cations. We transfer most of SAPT-UA parameters of [$C_n$MIM] cations from previous studies. Note that, as for a new CM atomtype which bonded to C2 atomtype, we transfer force fields of C3 atomtype which bonded with N atom on the [$C_n$MIM] cation. You can see atomtype names in Figure 4.1. To assign the partial charges of the cations, we fit all charges except atom types of N-alkyl chain with match ab initio electric field. We refer the details of the fitting method in some studies.[26, 36] The partial charges and SAPT-UA parameters are seen in Supporting information. The SAPT-UA parameter set shows a good agreement with interaction energy components calculated by SAPT(PBE0) for [BMMIM][BF4] dimers. Note that our SAPT-UA model does not consider induction parameter (no induced dipole). As the result, the density of neat ILs is 1.161 $g/cm^3$ at 323 K for [BMMIM][$BF_4$] liquids, 1.262 $g/cm^3$ at 323 K for [EMIM][$BF_4$], and 1.251 $g/cm^3$ at 298 K for [EMMIM][$BF_4$], which shows good agreements within $2\%$ error with experiments .[37, 38, 39]

### 4.2.2 Molecular dynamics simulations

All molecular dynamics (MD) simulations are performed using the OpenMM version 7.3.0 software that utilizes GPU-accelerated computing for molecular simulations.[40] The cut-off distance for nonbonded van der Waals interactions is 1.4 nm. Long-range electrostatics are calculated with

the particle mesh Ewald method. The Langevin thermostat is used to constrain system temperatures. For all isothermal-isobaric (NPT) simulations, we adapt Monte Carlo (MC) barostat at 1 atm. We use 4 fs of time step in our united atom model simulations. A PEO/IL system is composed of PEO and [EMIM][$BF_4$], [EMMIM][$BF_4$], [BMIM][$BF_4$], or [BMMIM][$BF_4$]. Note that the chain length of PEOs in this work is n=9 for $CH_3$-[O-C-C]$_n$-O-$CH_3$.

We utilize MD simulations to manipulate input data of deep neural network (DNN) for the prediction of phase boundary of PEO/ILs. Before applying the DNN, we use our Convolution method[25] which obtains the phase boundary at relatively high temperatures (far from the critical point). Initially, we make three independent cells which contain both pure IL phase and arbitrary PEO-rich phase with slab interface but keep the total mole ratio $N_{PEO}/N_{IL} = 0.5$ in the cells. We run 50 $ns$ NPT ensemble simulations with a MC barostat coupling on z-axis under the constraint of constant $x, y$-surface area. To fully reach equilibrium, we run canonical (NVT) simulations for 1.5 $\mu s$ and then get average density profiles for the last 500 $ns$ NVT simulations using the Convolution method. As you can see Fig.4.2, the phase coexistence of PEO/ILs is strongly affected due to the finite system size and becomes saturated for a large system size. To converge the dependency of the finite size effect on x and z axis,[41] we perform simulations by varying cell lengths ($L_{x,y}$ and $L_z$) in a range of $L_x = L_y = 3.5-5$ nm and $L_z/L_x = 3-5$. Below 550 K, our PEO/IL systems with at least 100,000 united atoms are needed for the convergence of phase boundary, which is not feasible with current computation resource. Thus, we take the result of phase coexistence at relatively high temperatures such as 550, 560, 570, and 580 K for PEO/[BMIM][$BF_4$] and PEO/[BMMIM][$BF_4$], and 570 K and 580 K for PEO/[EMIM][$BF_4$] and PEO/[EMMIM][$BF_4$], respectively. Finally, the result allows us to assign the equilibrium phase (e.g. one-phase or two-phases) when a system is under a certain mole fraction and temperature, which will be used with its mixture properties to train NN later.

In addition to obtain the training data, a set of collective properties under a wide range of mole fractions and temperatures are obtained to analyze mixture properties and predict phase boundary.

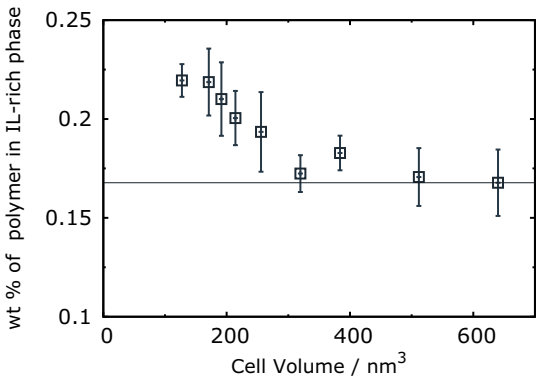


Figure 4.2: The finite size effect of phase boundary of PEO/[BMIM][$BF_4$] mixtures at 580 K. The phase boundary converges to a value as the cell volume ($L_x \times L_y \times L_z$) increase by enlarging it in a range of $L_x = L_y = 3.5 - 5$ nm and $L_z/L_x = 3 - 5$. Gray line in the middle serves as an eye-guide to see its convergence.

We generate cubic cells of $\sim 3,000$ total UA atoms varying 0 - 100 PEO molecules and 0 - 200 IL pairs to have 11 different mole fractions of PEOs, [0.0, 0.0256, 0.811, 0.1243, 0.25, 0.333, 0.429, 0.6, 0.818, 0.905, 1.0]. For equilibrium process, NPT simulations are performed for 600 $ns$ at [420, 430, ..., 570, 580 K] for PEO/[BMIM][$BF_4$] and PEO/[BMMIM][$BF_4$] and [350, 360, ..., 570, 580 K] for PEO/[EMIM][$BF_4$] and PEO/[EMMIM][$BF_4$]. Then, with the last 100 $ns$ NPT simulation trajectories, we calculate some properties we will discuss at next paragraph. Note that we run 10 $ns$ NVT simulations for the calculation of mole cohesive energy

As a component for NN input data, the excess molar volume $V^E$ can depict the non-ideality of a mixture, that is,

$$V^E = V_{mix} - \sum_{j=PEO,IL} x_j V_{j,m} \tag{4.1}$$

where $V_{mix}$ and $V_{j,m}$ represent the molar volume for a mixture and pure component $j$, respectively. $x_j$ represents the mole fraction of component $j$ (1 for ILs and 2 for polymer). As for non-bonding energy deviation in mixtures, we use the molar cohesive energy between polymer and ILs, $E_{coh}$,

$$E_{coh}(PEO - IL) = E_{mix} - \sum_{j=PEO,IL} E_j \tag{4.2}$$

where $E_{mix}$ is the molar non-bonding energy (electrostatic and Van der Waals) of mixture and $E_j$ is the molar non-bonding energy between component $j$'s (PEO-PEO and IL-IL) in the mixture.

To quantify the PEO-cation interactions, we use the weighted coordination number ($N_{cont}$) which is the number of oxygen atoms of single PEO around a given imidazolium cation weighting by the number of unsaturated carbon types (C1 and C2 atomtypes in Fig. 4.1) within 5 $\mathring{A}$, which is similar to $CN^{O}_{BMIM}$ in a previous study.[27] $N_{cont}$ can be characterized by two types of PEO segment conformations such as molar number of PEO-IL pairs with low contact number, $N^{low}_{cont} = \sum_{i=1}^{4} N_{pair}(N_{cont} = i)/\left(N_{pol} + N_{ILs}\right)$ and that with high contact number, $N^{high}_{cont} = \sum_{i=5}^{\infty} N_{pair}(N_{cont} = i)/\left(N_{pol} + N_{ILs}\right)$, which will be used for input NN data later. Also, we calculate the spatial distribution functions, $g\left(r, \phi, \varphi\right)$ of intermolecular pairs via Travis software.[42] Also, as conformation of polymers, the radius of gyration ($R_g$) is defined as

$$R_g{}^2 = \frac{\sum_i m_i (r_i - r_{com})^2}{\sum_i m_i} \tag{4.3}$$

where $r_i$ is the position of site $i$, $m_i$ is the mass of site $i$, and $r_{com}$ is the position of the center-of-mass.

### 4.2.3 Deep neural network

As the result of united-atom molecular simulations with good accuracy and fast performance, we now have a data of quantitative collective properties and known phases under system condition variables for prediction of phases by neural network. As the input layer, we use the normalized values of $V^E$, $E_{coh}$, $N^{low}_{cont}$, $N^{high}_{cont}$, temperature, mole fraction, and cation types, e.g. 0, 0.25, 0.75, and 1.0 for [BMIM], [BMMIM], [EMMIM], and [EMIM], respectively. For the high resolution of phase diagrams, we interpolate those collective quantities with 1 K for temperature interval at 101 mole fractions using following methods. As for interpolation of excess molar volumes and

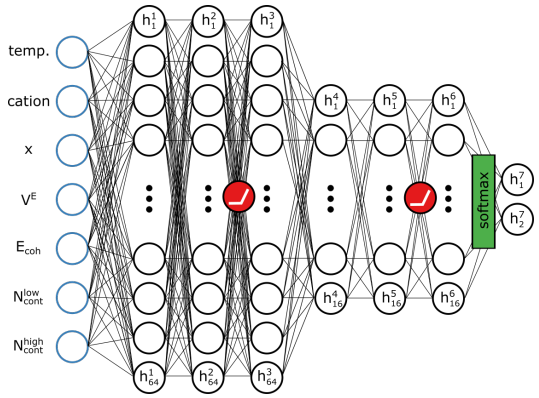


Figure 4.3: Pictorial image of our NN model utilizing mixture properties such as temperature, cation types, mole fractions of PEOs, excess molar volume, molar cohesive energy between polymer and ionic liquids, and molar number of two types of polymer-cation pairs. The hidden layers have 64, 64, 64, 16, 16, 16, 2 neurons from left to right layers. Note that red filled circles and green rectangular box represent ReLu activation and softmax function, respectively.

cohesive energy between PEOs and ILs, we use Redlich-Kister polynomials given below:

$$V^E = x_1 x_2 \sum_{k=1}^{3} A_k (1 - 2x_1)^{k-1} \tag{4.4}$$

where $X$ is the excess molar volume and $A_k$'s are the fitting parameters. Otherwise, other properties are interpolated linearly. With those input data, we set output layer for already known mixing and separated phases; as for PEO/[BMIM][$BF_4$] and PEO/[BMMIM][$BF_4$] systems, mixing phase for any mole fraction at 420 K and mixing/separation phase for certain mole fractions at 550 - 580 K, and as for PEO/[EMIM][$BF_4$] and PEO/[EMMIM][$BF_4$] systems, mixing phase for any mole fraction at 350 K and mixing/separation phase for certain mole fractions at 570 and 580 K. To determine NN architecture, we use AutoKeras, one of Automated Machine Learning (AutoML) libraries which automatically search a good model by testing candidates of NN architectures. One of good NN models is found with seven hidden layers as you can see Fig.4.3. For the prediction step at a given mole fraction, we define the transition temperature where 50% probability of mixing phase . After 200 random initializations on NN weights, the phase diagram results are reported by averaging predicted phase transition temperatures.

## 4.3 Results and discussions

We investigate C2 methylation and alkyl chain length effect on cohesive energy between ILs and PEOs. In Figure 4.4, we find that all mixtures show attractive energetic interaction. The attractive interactions between PEOs and ILs can be understood by electrostatic interactions between negative partial charge of oxygen atoms of PEOs and the positive charge of cations while weaker interactions between ILs and those of PEOs in mixture. Also, the attraction is maximized around 50 % mole fraction of PEOs, which is likely that equal molar ratio of PEO and ILs is preferred to interact. The strength of the polymer-IL attraction can be alleviated by C2 methylation. Compared with results of PEO/[BMIM][$BF_4$], the molar cohesive energy slightly increases by $\sim$ 1 kcal/mol for $x = 0.5$ of PEO/[BMMIM][$BF_4$]. In other hands, C2 methylation leads to energetic repulsion between PEOs and ILs due to loss of attractive interaction of C2-H hydrogen bonding. Because the hydrogen bonding easily weaken by high temperature, we see the increase of molar cohesive energy at the higher temperature. However, the C2 methylation effect is not such large difference on the molar cohesive energy. Also, the attractive energy is pronounced by 2 - 3 kcal/mol for a short alkyl chain length for [EMIM] cations. Due to the relatively small excluded volume or less steric hindrance of the alkyl chain, it may form a closed conformation of PEO - cation pairs.

We calculate excess molar volumes in the whole composition range for the studies temperatures. As you can see Figure 4.5, all the studied binary mixtures show negative $V^E$ with minima near $x = 0.6$ mole fraction of PEOs. This implies that, because our UA model does not explicitly regard the hydrogen bonding of C2-H $\cdots$ to oxygen atoms, electrostatic interaction between ions and PEOs mainly accounts for the contraction behavior of $V^E$. Compared with neat ILs and PEO melts, mixture of PEO with ILs could make effective packing by negative point charge of oxygen atoms of PEOs. Whereas PEOs in melts have a relatively large free volume and weakly interact, previous strong attraction between PEO and ILs may drive packing of PEO-cation packing under IL-rich phase with less free volume and strong cohesive energy of ions. The negative $V^E$ curve is

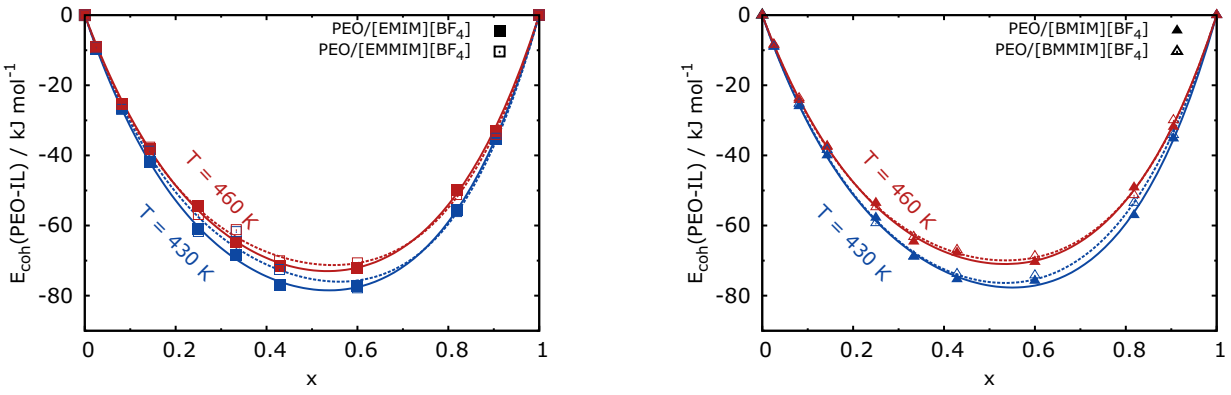


Figure 4.4: Variation of molar cohesive energy of (top) PEO/[EMIM][$BF_4$] and PEO/[EMMIM][$BF_4$] and (bottom) PEO/[BMIM][$BF_4$] and PEO/[BMMIM][$BF_4$] as a function of mole fraction of PEOs at 430 K and 460 K. Solid and dashed curves show fits according to the Redlich-Kister equation.

consistent with studies of polymer or short ethoxy group and imidazole-based ILs;poly(ethylene glycol) or PEG in [BMIM][$BF_4$],[43] [BMIM][$PF_6$],[44] and [$C_n$IM][Br],[45] and diethylene glycol dimethyl ether (or the dimer of PEOs) in [BMIM][$BF_4$],[46] except ethylene glycol/IL mixture which showed positive $V^E$.[47, 48]

The C2 methylation effect on $V^E$ can be seen with comparison of PEOs in [EMIM][$BF_4$] and [EMMIM][$BF_4$]. The top image of Fig. 4.5 shows that $V^E$ of [EMMIM][$BF_4$] is higher than that of [EMIM][$BF_4$] and the gap is smaller as temperature increases. It clearly indicates that the hydrogen bonding on C2 position leads to more negatively reduction on excess molar volume, which is consistent with the results of [BMIM][$BF_4$] or [BMMIM][$BF_4$] + dimethyl sulfoxide mixture.[47, 37]. Also, high thermal energy (high temperature) weaken the hydrogen bonding on C2-H atoms as you can see the smaller gap of $V^E$, which is supported by the MD simulation result of PEO/[BMIM][BF4].[24]

One interesting behavior on $V^E$ is the negative dependency with temperature that the excess molar volume of mixture is smaller as temperature increases. Typically, intermolecular interactions weaken by the thermal motion of molecules which leads to volume expansion and the magnitude of $V^E$ would reduce, as you can see aqueous PEG solutions[49, 50] and PEG in small alcohol

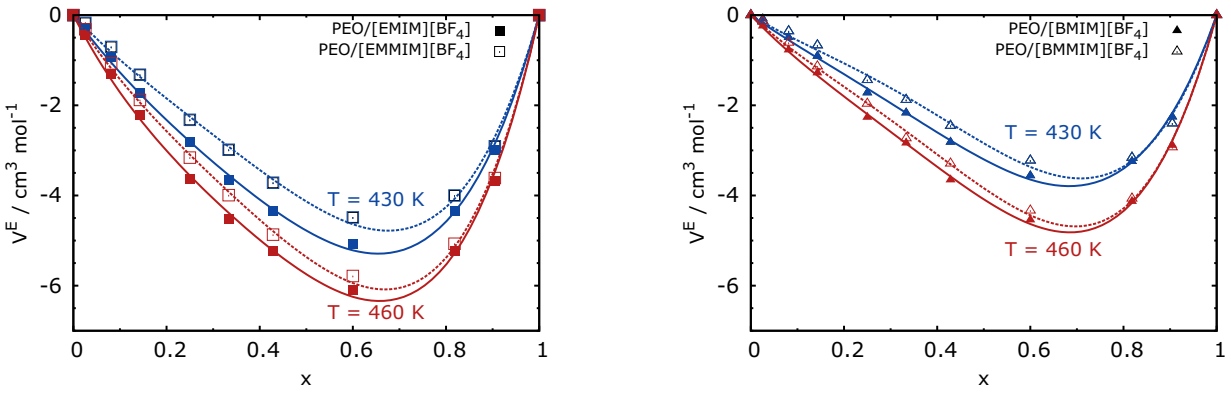


Figure 4.5: Variation of excess molar volume of (top) PEO/[EMIM][$BF_4$] and PEO/[EMMIM][$BF_4$] and (bottom) PEO/[BMIM][$BF_4$] and PEO/[BMMIM][$BF_4$] as a function of mole fraction of PEOs at 430 K and 460 K. Solid and dashed curves show fits according to the Redlich-Kister equation.

solvents.[51] However, there is no reason to increase intermolecular interaction with temperatures for our PEO/ILs systems including ILs with PEG[43], polar organic solvents[52, 47, 37, 53, 54] and water.[55, 56] Because hydrogen bonding weaken as temperature increases, the $\left(\frac{\partial V^E}{\partial T}\right)_P < 0$ could be due to the strong Coulombic interaction which is relatively independent in a range of temperatures we studied. In other words, that electrostatic attractions of PEO - ILs might be sturdy enough to keep the contraction effect on $V^E$ upon mixing although temperature increases by some extent to expand volumes of neat IL and PEO melts.

In terms of alkyl chain length effect on excess molar volume, the shorter alkyl chain length shows more negative $V^E$. It also observed similar results with mixtures of imidazolium based cation and halide with several molecular weights of PEGs.[45] In general, the C-C bond of alkyl chains are freely rotated by thermal motion, thus allows to increase the excluded volume. Thus, longer chain on cations can occupy a large volume to prevent somewhat conformations of polymer close to cations, which may induce less packing between PEOs and cations.

Figure D.14 shows radial distribution functions (RDF) of oxygen atoms of PEOs and fluorine atoms with C1 and C2 atomtypes for PEO/[BMIM][$BF_4$] and PEO/[BMMIM][$BF_4$]. As for the RDFs of PEO/[BMIM][$BF_4$] from the top panel of Fig. D.14, the first peaks of both oxygen atoms

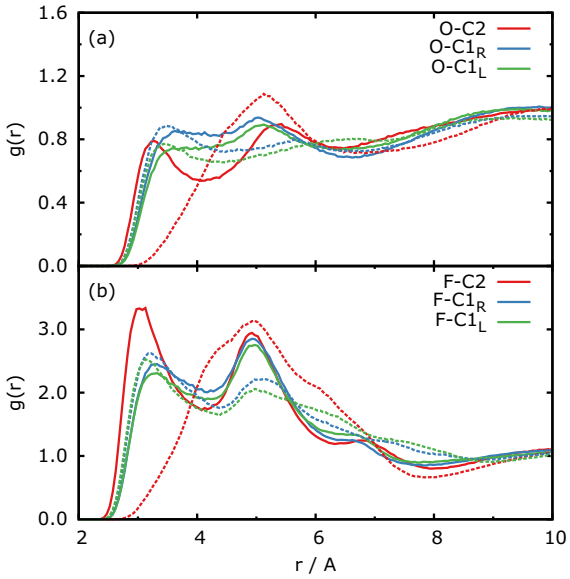


Figure 4.6: Variation of radial distribution functions of (a) oxygen atoms of PEOs and (b) flourine atoms of [$BF_4$] anions at 430 K for x=0.43. Solid lines and dashed lines are for PEO/[BMIM][$BF_4$] mixture and PEO/[BMMIM][$BF_4$] mixtures, respectively.

and flourine atoms of PEO are correlated to C2 atomtypes. Figure 4.7 confirms that oxygen atoms of PEOs mostly prefer the location near C2 atomtype in PEO/[BMIM][$BF_4$], which was reported in previous MD simulation studies.[27, 24, 57] In the case of PEO/[BMMIM][$BF_4$], we find that the probability of oxygen atom and C1 atomtype is pronounced as the shortest neighbor, which are shown as the density map in the bottom panel of Fig. 4.7. It clearly indicates that the methylation not only prevents intermolecular interaction via C2 atomtype but also significanly changes spatial coordination surface of of both PEO and [$BF_4$]. Similarly, the importance of interactions of C1 atomtypes with solute was found in a IR and DFT study of DMSO/[BMMIM][$BF_4$].[58] Note that the similar results are seen from the comparison of PEO/[EMIM][$BF_4$] and PEO/[EMMIM][$BF_4$] and the alkyl chain effect on RDFs and probability density maps of intermolecular pairs is negligibly small except the decrease of first RDF peak of F atom with C2 atomtype with alkyl chain length. (See figures in Appendix D)

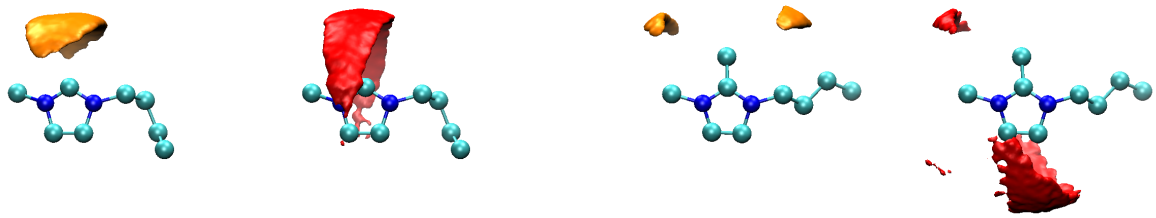

Figure 4.7: The probability density map of fluorine atom (yellow) and oxygen atoms (red) around the C1 and C2 atomtypes of cations of (top) PEO/[BMIM][$BF_4$] and (bottom) PEO/[BMMIM][$BF_4$] at $x$=0.43 and 430 K. Isosurface values are 12.0 $nm^{-3}$ for fluorine atom pair density map and 2.3 $nm^{-3}$ for oxygen atom pair density map.

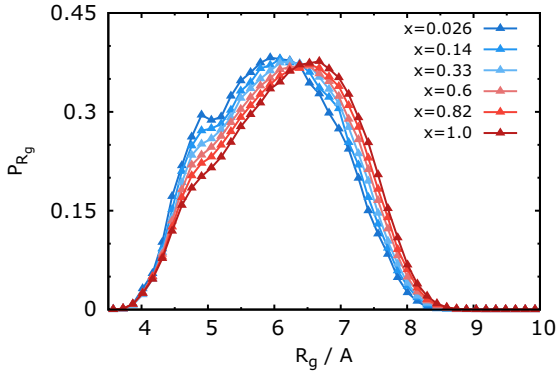


Figure 4.8: Probabilities of $R_g$ of PEOs as a function of mole fractions of PEOs at 420 K for PEO/[BMIM][$BF_4$].

To study the methylation effect on polymer conformation, we calculate radius of gyration and end-to-end distance of polymers for conformation properties of PEOs. As you can see Fig. 4.8 for PEO/[BMIM][$BF_4$] at 430 K, it shows $R_g$ probabilities for $R_g < 6.5$ $\mathring{A}$ increase by adding ILs (from dark red to dark blue lines). In fact, the two $R_g$ peaks near 5 $\mathring{A}$ and 6 $\mathring{A}$ are signatures of PEO conformations as a result of PEO - [BMIM] cation interaction, which are known as ring segment and linear segment of PEOs.[27] The combinations of ring segment and linear segment are pronounced when very dilute solution of PEOs in IL. As a result of the segments, Fig. D.5 indicates the general trend that the average size of polymer increases with the mole fraction of PEOs.

Interestingly, there is no significant change of average values and distributions of $R_g$ by cation

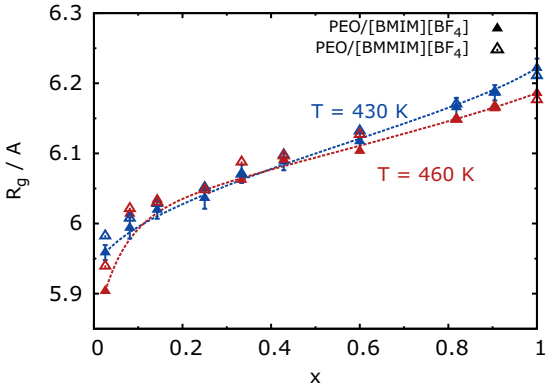


Figure 4.9: Plots of radius of gyration of polymers in PEO/[BMIM][$BF_4$] and PEO/[BMMIM][$BF_4$] as a function of mole fraction of PEOs at 430 K and 460 K. The y-error bar is the block average error of PEO/[BMIM][$BF_4$] at 430 K. Dotted lines serve as eye-guide lines for PEO/[BMIM][$BF_4$] mixture.

C2 methylation although the RDFs of oxygen atoms with IL cations are very different. As for conformations of PEOs in [BMIM][$BF_4$], it is known that the ring segments appear as PEO chains wrap cations around C2 atomtypes.[27] (see on the left of Fig. 4.10) Like wrapping conformation in PEO/[BMIM][$BF_4$], we found that the ring segments of PEOs are also found around [BMMIM] cations with the partial wrapping conformation to the C2-CM plane as shown in the right of Fig. 4.10. (For the 3D animations of the snapshots, see Supporting Materials) It indicates that the wrapping conformation of PEOs around [BMMIM] cation is not necessarily caused by the C2 hydrogen bonding.

In addition to the partial wrapping conformation of PEOs around [BMMIM] cation, we see "crown ether" conformation as another ring segment contributor. Fig. 4.11 shows that some portion of oxygen atoms of single PEO forms crown ether conformation near C1 atomtypes. Unlike single C2 atomtype of [BMIM] cation with alkyl chains on both N atoms, two atoms of C1 atomtypes with positive point charges can have an opportunity for oxygen atoms to occupy space with the crown ether shape and interact the negative charge of N atomtypes at a far distance. Therefore, the crown ether conformation can lead to small $R_g$ of PEO in PEO/[BMMIM][$BF_4$] and not only wrapping conformation but also crown ether formation positively affect on the probability of ring

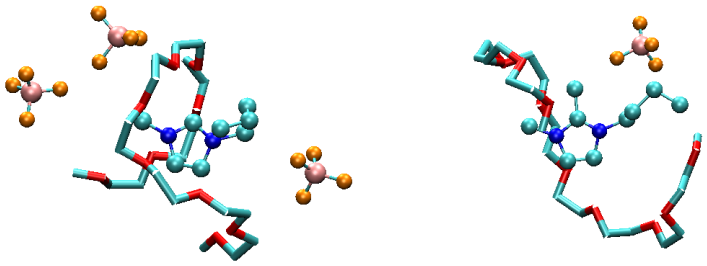

Figure 4.10: Representative snapshots showing ring segment conformations of PEOs in two PEO/IL mixtures. The entire PEO chain is wrapped around a single cation of (left) [BMIM] and (right) [BMMIM]. For colors of atomtypes, blue, cyan, tan, pink, and red represent N, C, F, B, and O atomtypes, respectively.

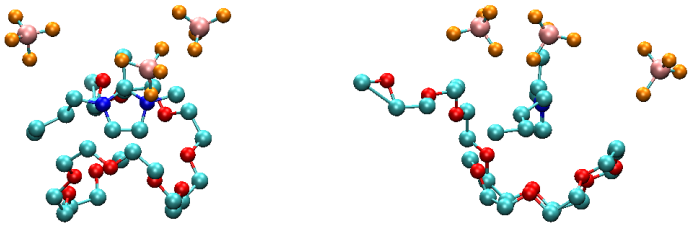

Figure 4.11: Representative snapshot of crown ether conformations of PEO around single [BMMIM] cation in (left) the front view and (right) the left side view. The representative colors are the same as the colors of Fig. 4.10.

segments or small $R_g$ values, e.g. 4.5 - 6 $\AA$ in Fig. 4.8. The appearance of the additional directional hydrogen bonding would be important for understanding of entropic-driven LCST behaviors of PEO/[$C_n$MMIM][$BF_4$].

Those unique conformations of PEOs with ILs can be evaluated utilizing the weighted coordination numbers of oxygen atoms of a particular PEO chain with single IL cation, $N_{cont}$'s. In particular, because PEOs with the high $N_{cont}$ value are likely to have ring segments (wrapping and/or crown ether) around IL cations, we compare molar high contact numbers for $N_{cont} > 4$ as a function of mole fraction. As you can see Fig. 4.12, methylation increase the number of oxygen atoms of PEOs with IL cations with high contacts. In other words, [$C_n$MMIM] cations enhance the

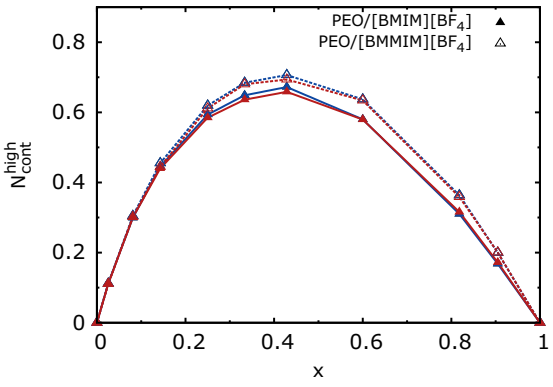


Figure 4.12: Variations of molar high contact numbers of PEOs with IL cation for (filled triangle) PEO/[BMIM][$BF_4$] and (empty) PEO/[BMMIM][$BF_4$] at (blue) 430 K and (red) 460 K. Dashed and dotted lines are the result of linear interpolation of points.

ring segment conformations. It implies that the appearance of crown ether formation of PEOs and two interacting locations of PEO-[$C_n$MMIM], such as near C1 atomtype and C3 atomtype may increase the moiety of ring segments. Also, the $N_{cont}^{high}$ is not changed by methylation for IL-rich compositions but deviated for PEO-rich compositions. It may indicate the dependency of mole fraction on crown ether formation. In addition, a long chain length of cation reduces the moiety of ring segments, which may be also explained by the steric hindrance effect of long alkyl chains as we explained for mixture properties.

Collecting those mixture properties and system conditions, we predict phase boundaries of our four PEO/ILs systems to see effects of methylation and alkyl chain length on their phase diagrams. As shown in Figure 4.13, the result of machine learning (ML) is somewhat promising to predict phase boundaries and critical points. Although phase boundaries at very far critical points are obtained from MD simulations and used to train our NN without any chemistry knowledge, we find that a short alkyl chain length of cations and C2 methylation on cations reduces critical temperatures ($T_c$), which is consistent with previous experimental studies.[17, 18, 20]

Although NN cannot give how our input data is utilized (or weighted) on prediction of phase behaviors, some mixture properties can be accounted for the shift on LCST behaviors. As for a long alkyl chain length of cation, we can explain the high critical temperature due to low density

and cohesive energy of [BMIM] rather than [EMIM] cation in neat ILs.[59] The low density by the flexibility of alkyl chains can hinder PEO-cation packing formation, but the weaker cohesive energy of cation with anions may possibly enhance intermolecular interactions of PEO - cation. Finally, our results indicate long alkyl chain length of cations improve solubility of PEOs in ILs.

Also, in regards of C2 methylation, we found crown ether formation and wrapping structure contributing on ring segments of PEOs, and saw slightly increase of number of PEO-IL contacts for ring segment. In contrast, the methylation leads to less effective packing, then gives higher excess molar volume. As the mixed results by C2 methylation, our result shows slightly decrease of $T_c$ by $\sim$ 10 K. These weak methylation effect is also observed in acidity strength of ILs.[60]

For the effect of modification of cations on critical composition ($wt_c$), we do not see significant change of critical composition. In our PEO/ILs systems, the phase diagram shows asymmetric phase boundary of all PEO/ILs, for example, critical points of our four mixtures are $\sim$ 60 wt% of PEOs, which consistent with experimentally reported critical points of PEG/[EMIM][B$F_4$] systems.[18] In fact, the C2 methylation effect for the critical point ($wt_c$ and $T_c$) is little unlike the result of the experiments. In fact, we do not see significant shifts of peak position toward polymer-rich for our mixture properties by methylation. Considering results of two theoretical studies, cohesive energies of neat methylated ILs are greater by 18 kJ/mol and 9 kJ/mol comparing with [EMIM][$BF_4$] and [BMIM][$BF_4$], which means slightly less attraction between ions. Then, the less difference between cohesive energy of PEO and that of ILs can alleviate the increase of critical composition.[21] Also, due to the similar values of dielectric constants and acidity strength of [BMIM][NTf2] and [BMMIM][NTf2],[61, 60] it seems to appear a small or negligible change on $wt_c$.[22]

Unlike our phase behavior result, Lee and coworkers reported $\sim$ 56 K change of $T_c$ and 20 wt% shift toward high $wt_c$ due to C2 methylation. While PEO polymers only have ethoxy groups as hydrogen bonding acceptors (HBAs), end monomers of PEG are hydroxyl group which typically play a role as a hydrogen bonding donor (HBD). With our small molecular weight of PEOs, the LCST

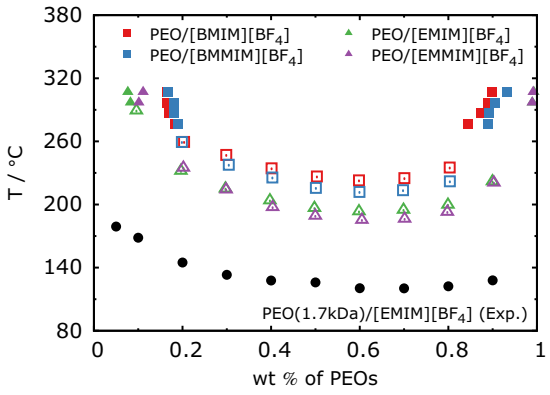


Figure 4.13: Phase diagrams of our PEO/IL mixtures with experimental data. Utilizing (filled colors except black) MD simulation data result, (empty) phase boundary near the critical points are obtained via artificial neural network. Black circle points are taken from clouding points of PEO (Mn = 1.7 kg/mol) in [EMIM][$BF_4$].[18]

result can be changed by the HBD end groups, well known as many aqueous polymer solutions such as PEG,[62] poly(N-isopropylacrylamide),[63, 64, 65, 66] and poly(2-(dimethylamino)ethyl methacrylate).[67] Note that they showed, as hydroxyl end groups of PEGs in [EMIM][$BF_4$] are replaced with methyl group, the $T_c$ decreases by 30 K. It means the LCST behavior can be strongly affected with even a large molecular weights ($\sim$ 2 kg/mol for Mn) of polymers by the small portion of end groups, thus our LCST result may deviate due to such a small molecular weight $\sim$ 0.4 g/mol.

Adding to the possible factor of LCST behavior difference with the experimental study, the weak effect of C2 methylation in our work could be due to the united atom model which does not explicitly consider hydrogen atoms. Typically, three-body interaction is considered to reflect the directional hydrogen bonding in mlecular simulations. However, our united atom model depicts simpler representations by removing hydrogen atoms to improve simulation performance, instead of best accuracy. And we fit parameters of united atom types for non-bonding interactions (without induction energy) using SAPT. Therefore, our SAPT-UA model for the H-bond candidate atom-types would be plausibly interpreted by van der Waals or electrostatic energy, and it is possible to miss some extent of covalent contribution, proton, and/or charge transfer contributions. In the

sense, a study with atomistic or polarizable force fields or first-principle quantum simulation would be worth if H-bonds are well considered for better accuracy.

## 4.4 Conclusions

Our study of utilizing molecular simulation and neural network investigated the effects of methylation on the acidic position (C2 atomtype) and alkyl chain length of imidazole-based ionic liquids on PEO mixture properties and phase behaviors. As for methylation effect, we found that molar cohesive energy between PEO and ILs and excess molar volume increases, which means less attractive interaction between them. Because of lack of C2 hydrogen bonding (see Fig. 4.1) on [$C_n$MMIM] cation, PEOs prefer interacting near C1 positions and between CM and C3 positions to avoid coordination around C2 atomtype. Although there are negligible change on average $R_g$ values by C2 methylation, the polymer conformation is somewhat different. PEOs shows not only wrapping conformation around any single cation but also crowon ether form near [BMMIM] cations, which serves as contributing "ring segment" and increases the molar number of pairs with higher $N_{cont}^{high}$ for PEO/[BMMIM][$BF_4$] compared with PEO/[BMIM][$BF_4$]. These polymer conformation can contribute the entropic-driven LCST behaior of PEO/[$C_n$MMIM][$BF_4$] like the case of PEO/[BMIM][$BF_4$]. In terms of alkyl chain length effect, a short chain length of cations affects smaller excess molar volume (more compact molar volume), which may due to a large excluded volume of alkyl chain by thermal motion, but other properties are changed by a little. Lastly, from predicted phase boundary by neural network, we found that critical temperature decreases due to lack of hydrogen bonding on C2 position and increases with alkyl chain of cation with PEOs, which shows good agreement with experimental studies.

Although some weakness of our united atom force field may exist for complex systems with hydrogen bonding, neural network can predict phase boundary well using calculated properties from simulations. As a result of NN, the critical points of PEO/ILs show consistent trends of

methylation and alkyl chain effect on phase behavior with experimental studies. The NN model is fed in the tremendous amount of data at wide range of temperature and compositions, but prior knowledge is not necessary except small training data at far from the critical point. Although there are some rigorous studies left such as optimizing hyperparameters, finding architecture, and testing the NN reliability, the NN technique combining simulation data would be alternatively promising because it is enough with a number of simulations with small system size regardless of critical points with known phase coexistence points.

# References

[1] Tom Welton. “Ionic liquids: a brief history”. In: *Biophysical Reviews* 10.3 (2018), pp. 691–706.

[2] Robert Hayes, Gregory G. Warr, and Rob Atkin. “Structure and Nanostructure in Ionic Liquids”. In: *Chemical Reviews* 115.13 (2015). PMID: 26028184, pp. 6357–6426.

[3] Binshen Wang et al. “Are Ionic Liquids Chemically Stable?” In: *Chemical Reviews* 117.10 (2017). PMID: 28240867, pp. 7113–7131.

[4] Rohit L. Vekariya. “A review of ionic liquids: Applications towards catalytic organic transformations”. In: *Journal of Molecular Liquids* 227 (2017), pp. 44 –60.

[5] Ksenia S. Egorova, Evgeniy G. Gordeev, and Valentine P. Ananikov. “Biological Activity of Ionic Liquids and Their Application in Pharmaceutics and Medicine”. In: *Chemical Reviews* 117.10 (2017). PMID: 28125212, pp. 7132–7189.

[6] Mariana Díaz, Alfredo Ortiz, and Inmaculada Ortiz. “Progress in the use of ionic liquids as electrolyte membranes in fuel cells”. In: *Journal of Membrane Science* 469 (2014), pp. 379 –396.

[7] Timothy P. Lodge. “A Unique Platform for Materials Design”. In: *Science* 321.5885 (2008), pp. 50–51.

[8] Kye-Si Kwon and Tse Nga Ng. “Improving electroactive polymer actuator by tuning ionic liquid concentration”. In: *Organic Electronics* 15.1 (2014), pp. 294 –298.

[9] Satoru Imaizumi et al. “Printable Polymer Actuators from Ionic Liquid, Soluble Polyimide, and Ubiquitous Carbon Materials”. In: *ACS Applied Materials & Interfaces* 5.13 (2013). PMID: 23738653, pp. 6307–6315.

[10] B Sasikumar, G Arthanareeswaran, and AF Ismail. “Recent progress in ionic liquid membranes for gas separation”. In: *Journal of Molecular Liquids* 266 (2018), pp. 330–341.

[11] Masayoshi Watanabe et al. “Application of Ionic Liquids to Energy Storage and Conversion Materials and Devices”. In: *Chemical Reviews* 117.10 (2017). PMID: 28084733, pp. 7190–7239.

[12] Ian W Hamley and Ian W Hamley. *The physics of block copolymers*. Vol. 19. Oxford University Press Oxford, 1998.

[13] Nikos Hadjichristidis, Stergios Pispas, and George Floudas. *Block copolymers: synthetic strategies, physical properties, and applications*. John Wiley & Sons, 2003.

[14] MM Yallapu and MK Reddy. *Biomedical applications of nanotechnology, ed. V. Labhasetwar and DL Leslie-Pelecky*. 2007.

[15] Elena V Batrakova and Alexander V Kabanov. “Pluronic block copolymers: evolution of drug delivery concept from inert nanocarriers to biological response modifiers”. In: *Journal of controlled release* 130.2 (2008), pp. 98–106.

[16] Koichi Kodama et al. “Structural effects of polyethers and ionic liquids in their binary mixtures on lower critical solution temperature liquid-liquid phase separation”. In: *Polymer journal* 43.3 (2011), pp. 242–248.

[17] Hau-Nan Lee and Timothy P Lodge. “Lower critical solution temperature (LCST) phase behavior of poly (ethylene oxide) in ionic liquids”. In: *The Journal of Physical Chemistry Letters* 1.13 (2010), pp. 1962–1966.

[18] Hau-Nan Lee et al. “Unusual lower critical solution temperature phase behavior of poly (ethylene oxide) in ionic liquids”. In: *Macromolecules* 45.8 (2012), pp. 3627–3633.

[19] Wenlong Li and Peiyi Wu. “Unusual phase transition mechanism of poly (ethylene oxide) in an ionic liquid: opposite frequency shifts in C–H groups”. In: *Soft Matter* 9.48 (2013), pp. 11585–11597.

[20] Zhilin Xiao et al. “Unusual phase separation and rheological behavior of poly (ethylene oxide)/ionic liquid mixtures with specific interactions”. In: *Soft Matter* 12.36 (2016), pp. 7613–7623.

[21] Ronald P White and Jane EG Lipson. “Origins of unusual phase behavior in polymer/ionic liquid solutions”. In: *Macromolecules* 46.14 (2013), pp. 5714–5723.

[22] Issei Nakamura. “Spinodal decomposition of a polymer and ionic liquid mixture: Effects of electrostatic interactions and hydrogen bonds on phase instability”. In: *Macromolecules* 49.2 (2016), pp. 690–699.

[23] Issei Nakamura. “Effects of Dielectric Inhomogeneity and Electrostatic Correlation on the Solvation Energy of Ions in Liquids”. In: *The Journal of Physical Chemistry B* 122.22 (2018), pp. 6064–6071.

[24] Eunsong Choi and Arun Yethiraj. “Entropic mechanism for the lower critical solution temperature of poly (ethylene oxide) in a room temperature ionic liquid”. In: *ACS Macro Letters* 4.7 (2015), pp. 799–803.

[25] Hyuntae Jung and Arun Yethiraj. “A simulation method for the phase diagram of complex fluid mixtures”. In: *The Journal of chemical physics* 148.24 (2018), p. 244903.

[26] Chang Yun Son et al. “First-principles united atom force field for the ionic liquid bmim+ bf4–: An alternative to charge scaling”. In: *The Journal of Physical Chemistry B* 120.14 (2016), pp. 3560–3568.

[27] Chang Yun Son et al. “Conformational and dynamic properties of poly (ethylene oxide) in BMIM+ BF4–: A microsecond computer simulation study using ab initio force fields”. In: *Macromolecules* 51.14 (2018), pp. 5336–5345.

[28] Ljiljana Djekic, Svetlana Ibric, and Marija Primorac. “The application of artificial neural networks in the prediction of microemulsion phase boundaries in PEG-8 caprylic/capric glycerides based systems”. In: *International journal of pharmaceutics* 361.1-2 (2008), pp. 41–46.

[29] Snezana Agatonovic-Kustrin and Raid G Alany. “Role of genetic algorithms and artificial neural networks in predicting the phase behavior of colloidal delivery systems”. In: *Pharmaceutical research* 18.7 (2001), pp. 1049–1055.

[30] Snezana Agatonovic-Kustrin et al. “Prediction of a stable microemulsion formulation for the oral delivery of a combination of antitubercular drugs using ANN methodology”. In: *Pharmaceutical research* 20.11 (2003), pp. 1760–1765.

[31] RG Alany et al. “Use of artificial neural networks to predict quaternery phase systems from limited experimental data”. In: *Journal of pharmaceutical and biomedical analysis* 19.3-4 (1999), pp. 443–452.

[32] Aleksander Mendyk and Renata Jachowicz. “Unified methodology of neural analysis in decision support systems built for pharmaceutical technology”. In: *Expert Systems with Applications* 32.4 (2007), pp. 1124–1131.

[33] Snezana Agatonovic-Kustrin, David W Morton, and Ragini Singh. “Hybrid neural networks as tools for predicting the phase behavior of colloidal systems”. In: *Colloids and Surfaces A: Physicochemical and Engineering Aspects* 415 (2012), pp. 59–67.

[34] Issei Nakamura. “Phase diagrams of polymer-containing liquid mixtures with a theory-embedded neural network”. In: *New Journal of Physics* (2020).

[35] Krzysztof Pielichowski and Kinga Flejtuch. “Non-oxidative thermal degradation of poly (ethylene oxide): kinetic and thermoanalytical study”. In: *Journal of Analytical and Applied Pyrolysis* 73.1 (2005), pp. 131–138.

[36] Eunsong Choi et al. “First-principles, physically motivated force field for the ionic liquid [BMIM][BF4]”. In: *The journal of physical chemistry letters* 5.15 (2014), pp. 2670–2674.

[37] Oana Ciocirlan and Olga Iulian. “Properties of pure 1-butyl-2, 3-dimethylimidazolium tetrafluoroborate ionic liquid and its binary mixtures with dimethyl sulfoxide and acetonitrile”. In: *Journal of Chemical & Engineering Data* 57.11 (2012), pp. 3142–3148.

[38] Wei-Guo Xu et al. “Density, surface tension, and refractive index of ionic liquids homologue of 1-alkyl-3-methylimidazolium tetrafluoroborate [C n mim][BF4](n= 2, 3, 4, 5, 6)”. In: *Journal of Chemical & Engineering Data* 57.8 (2012), pp. 2177–2184.

[39] Xuesheng Hu et al. “Separation of ethyl acetate and ethanol by room temperature ionic liquids with the tetrafluoroborate anion”. In: *Journal of Chemical & Engineering Data* 53.2 (2008), pp. 427–433.

[40] Peter Eastman et al. “OpenMM 7: Rapid development of high performance algorithms for molecular dynamics”. In: *PLoS computational biology* 13.7 (2017), e1005659.

[41] Fabian Schmitz, Peter Virnau, and Kurt Binder. “Logarithmic finite-size effects on interfacial free energies: Phenomenological theory and Monte Carlo studies”. In: *Physical Review E* 90.1 (2014), p. 012128.

[42] Martin Brehm and Barbara Kirchner. *TRAVIS-a free analyzer and visualizer for Monte Carlo and molecular dynamics trajectories*. 2011.

[43] Majid Moosavi and Azadeh Daneshvar. “Synergistic effects and specific molecular interactions in the binary mixtures of [bmim][BF4] and poly (ethylene glycol) s”. In: *Journal of Molecular Liquids* 225 (2017), pp. 810–821.

[44] Shruti Trivedi and Siddharth Pandey. “Densities of 1-Butyl-3-methylimidazolium Hexafluorophosphate+ Poly (ethylene glycol) in the Temperature Range (283.15 to 363.15) K”. In: *Journal of Chemical & Engineering Data* 56.5 (2011), pp. 2168–2174.

[45] Heta Patel et al. “Thermophysical, acoustic and optical properties of binary mixtures of imidazolium based ionic liquids+ polyethylene glycol”. In: *The Journal of Chemical Thermodynamics* 99 (2016), pp. 40–53.

[46] JL Trenzado et al. “Molecular dynamics and experimental characterization of [BMIM][BF4] and [BMIM][PF6] with ether cosolvent binary mixtures”. In: *Journal of Molecular Liquids* 271 (2018), pp. 65–73.

[47] Oana Ciocirlan, Oana Croitoru, and Olga Iulian. “Densities and viscosities for binary mixtures of 1-butyl-3-methylimidazolium tetrafluoroborate ionic liquid with molecular solvents”. In: *Journal of Chemical & Engineering Data* 56.4 (2011), pp. 1526–1534.

[48] A Gutiérrez et al. “Insights on the mixtures of imidazolium based ionic liquids with molecular solvents”. In: *Journal of Molecular Liquids* 255 (2018), pp. 199–207.

[49] Erich A Muller and Peter Rasmussen. “Densities and excess volumes in aqueous poly (ethylene glycol) solutions”. In: *Journal of chemical and engineering data* 36.2 (1991), pp. 214–217.

[50] Na Zhang et al. “Excess molar volumes and viscosities of poly (ethylene glycol) 300+ water at different temperatures”. In: *Fluid phase equilibria* 313 (2012), pp. 7–10.

[51] Zohre Mousavi et al. “Thermophysical Properties Analysis of Poly (Ethylene Glycol) 600+ Methanol, Ethanol, 1-Propanol, and 2-Propanol Binary Liquid Mixtures”. In: *International Journal of Thermophysics* 41.2 (2020), p. 19.

[52] Julia Lehmann et al. “Densities and excess molar volumes for binary mixtures of ionic liquid 1-ethyl-3-methylimidazolium ethylsulfate with solvents”. In: *Journal of Chemical & Engineering Data* 55.9 (2010), pp. 4068–4074.

[53] Jie Wei et al. “Effect of temperature on the minimum excess molar volume and the molar surface Gibbs energy of the binary of the ether-functionalized ionic liquids [C22O1IM][SCN] with monohydric alcohols at T=(288.15–318.15) K”. In: *Journal of Molecular Liquids* (2020), p. 112856.

[54] Ren Ren et al. “Density, excess molar volume and conductivity of binary mixtures of the ionic liquid 1, 2-dimethyl-3-hexylimidazolium bis (trifluoromethylsulfonyl) imide and dimethyl carbonate”. In: *Journal of Chemical & Engineering Data* 56.1 (2011), pp. 27–30.

[55] Ana Navas et al. “Experimental thermodynamic properties of 1-butyl-2-methylpyridinium tetrafluoroborate [b2mpy][BF4] with water and with alkan-1-ol and their interpretation with the COSMO-RS methodology”. In: *Industrial & engineering chemistry research* 48.5 (2009), pp. 2678–2690.

[56] LPN Rebelo et al. “A detailed thermodynamic analysis of [C 4 mim][BF 4]+ water as a case study to model ionic liquid aqueous solutions”. In: *Green Chemistry* 6.8 (2004), pp. 369–381.

[57] Luciano T Costa and Mauro CC Ribeiro. “Molecular dynamics simulation of polymer electrolytes based on poly (ethylene oxide) and ionic liquids. I. Structural properties”. In: *The Journal of chemical physics* 124.18 (2006), p. 184902.

[58] Yan-Zhen Zheng et al. “Hydrogen-bonding interactions between 1-butyl-2, 3-dimethylimidazolium tetrafluoroborate and dimethyl sulphoxide”. In: *Journal of Molecular Structure* 1164 (2018), pp. 70–76.

[59] Jesse G McDaniel et al. “Ab initio force fields for imidazolium-based ionic liquids”. In: *The Journal of Physical Chemistry B* 120.28 (2016), pp. 7024–7036.

[60] Cécile Thomazeau et al. “Determination of an acidic scale in room temperature ionic liquids”. In: *Journal of the American Chemical Society* 125.18 (2003), pp. 5264–5265.

[61] Fabien André, Philippe Hapiot, and Corinne Lagrost. “Dimerization of ion radicals in ionic liquids. An example of favourable “Coulombic” solvation”. In: *Physical Chemistry Chemical Physics* 12.27 (2010), pp. 7506–7512.

[62] Elena E Dormidontova. “Influence of end groups on phase behavior and properties of PEO in aqueous solutions”. In: *Macromolecules* 37.20 (2004), pp. 7747–7761.

[63] JE Chung et al. “Effect of molecular architecture of hydrophobically modified poly (N-isopropylacrylamide) on the formation of thermoresponsive core-shell micellar drug carriers”. In: *Journal of Controlled Release* 53.1-3 (1998), pp. 119–130.

[64] Steven Furyk et al. “Effects of end group polarity and molecular weight on the lower critical solution temperature of poly (N-isopropylacrylamide)”. In: *Journal of Polymer Science Part A: Polymer Chemistry* 44.4 (2006), pp. 1492–1501.

[65] Atsushi Narumi et al. “A Versatile Method for Adjusting Thermoresponsivity: Synthesis and ‘Click’Reaction of an Azido End-Functionalized Poly (N-isopropylacrylamide)”. In: *Macromolecular rapid communications* 29.12-13 (2008), pp. 1126–1133.

[66] Haruhisa Akiyama and Nobuyuki Tamaoki. “Synthesis and photoinduced phase transitions of poly (N-isopropylacrylamide) derivative functionalized with terminal azobenzene units”. In: *Macromolecules* 40.14 (2007), pp. 5129–5132.

[67] Satyasankar Jana, Steven P Rannard, and Andrew I Cooper. “Structure–LCST relationships for end-functionalized water-soluble polymers: an “accelerated” approach to phase behaviour studies”. In: *Chemical Communications* 28 (2007), pp. 2962–2964.

# Chapter 5

# Conclusion Remark

We have presented several methods for obtaining phase coexistence of complex fluid mixtures and study phase behaviors of polymer solutions utilizing molecular simulations and a neural network technique. In Chapter 2, we developed the Interface method to obtain phase boundary of binary mixtures and got good agreement with the result of previous simulation studies except near the critical point of the Widom-Rowlinson model and a symmetric polymer blend model of freely jointed polymer molecules. In Chapter 3, we developed a supervised machine learning scheme with convolutional neural network by optimizing filter sizes to get phase boundaries near the critical point. We tested with previous two toy models using spatial coordinates of molecules and found the importance of understandings of intermediate phases during phase transition. However, these methods need more work to apply for real systems beyond such toy models for validation. In Chapter 4, we used an artificial neural network (NN) fed by collective properties for a study of phase behaviors of polymer in ionic liquids with various cations with simulation data. Although the NN result is needed to validate from future experimental studies, we can see the effect of methylation on C2 position and alkyl chain length of cations on NN-predicted phase behaviors.

These projects described above illustrate our developed method to understand phase behaviors of complex mixtures by finding phase boundaries using computer simulations and machine learn-

ing techniques. With help of fast hardware performance and increasing data size accessible, we can employ modern data-driven technique with less knowledge. Because the present time is a transition period of learning by machine for unknown findings or unsolved problems, I believe these data-driven works would be more pronounced for next years by whom has deep domain knowledge to apply in physics. I refer the phrase “To Infinity and Beyond!” in the Toy Story films.

# Appendix A

# Vapor-Liquid Equilibrium of Lennard-Jones Fluids using Gibbs-Duhem Integration Method

In this appendix, we reproduce the vapor-liquid equilibrium (VLE) of Lennard-Jones (LJ) fluids using Gibbs-Duhem integration.[1] As we discussed in Introduction chapter, the integration method is a powerful tool utilizing properties of phases for estimating next neighbors of phase boundary. Thus, we aim to test the Gibbs-Duhem method with the Clapeyron equation of single component such as Lennard-Jones system before doing trials for binary mixtures.

The potential energy of a pair of Lennard-Jones (LJ) particles as monoatomic non-polar molecules use two parameters following this equation:

$$V\left(r_{ij}\right) = 4\varepsilon\left(\left(\frac{\sigma}{r_{ij}}\right)^{12} - \left(\frac{\sigma}{r_{ij}}\right)^{6}\right) \tag{A.1}$$

where $r_{ij}$ is the distance between $i$-th particle and $j$-th particle. At $2^{1/6}\sigma \approx 1.122\sigma$, the potential reaches its minimum, $-\varepsilon$. In settings GROMACS software package for the simple LJ model, we simply set $\sigma = \varepsilon = m = k_B = 1$ in reduced unit, then many variables and units become simple

with $\sigma$ and $\varepsilon$. As noted in GROMACS manual, use $\frac{x}{k_B} \approx 120.272$ for the reduced temperature 1 where $k_B$ is gas constant. For pressure in GROMACS, use following unit conversion equation from bar to reduced pressure:

$$P\,[bar] = \frac{P^*\varepsilon\,[kJ/mol]}{\sigma^3\,[nm^3]} \frac{100}{N_{AV}\,[mol^{-1}] \cdot 10^{-23}} \tag{A.2}$$

where $N_{AV}$ is the Avogadro constant. For convenience, I upload the topology and force field files for VLE of a LJ model and argon models in my Github repository: `https://github.com/jht0664` Our simulation system consists of up to 10,000 LJ particles which are randomly distributed in a parallelepiped box, $L \times L \times 4.5L$, $L = 22.82630\sigma$. We use GROMACS 5.1.2 software package with Verlet integration algorithm.

Because the Gibbs-Duhem method starts at a stable state condition for which the two phases are known to be in equilibrium, we perform a simulation with coexisting phases as initial data. The simulation in the canonical ensemble starts at $T^* = 0.7$ above the triple point, $T_c = 0.694$. Temperature is kept constant using a Nose-Hoover thermostat. In order to simulate the heterogeneous system with vapor-liquid interface, not only electrostatic interactions but also Van der Waals interactions are treated using the particle mesh Ewald summation (PME)[2, 3]: real space cut-off distance of $5\sigma$, grid spacing of $1.2\sigma$, and interpolation order of 6. Figure A.1 is the final coordinate from $10,000\sigma^{-1}$ (in reduced time unit) NVT simulation. The last $5,000\sigma^{-1}$ trajectory is used for density profile of LJ fluid in Figure A.2. Our result of densities, $\rho_{liq} = 0.843$ and $\rho_{gas} = 0.002$, shows good agreement with that of grand-canonical transition-matrix Monte Carlo (TMMC).[4, 5]. From the result, we run a new simulation with the coexistence vapor density $\rho_{vap}$ in NVT ensemble to calculate the vapor pressure which will use for next NPT ensemble simulations.

For prediction and correction of coexistence conditions on VLE, simulations of each phase in isothermal-isobaric (NPT) ensemble are performed, applying to Gibbs-Duhem integration method with a simple forward Euler formula and Variable-Step-Size Corrector formula .[6] A cubic simulation box has 5,000 or 10,000 LJ particles for vapor or liquid phase, respectively. We compute

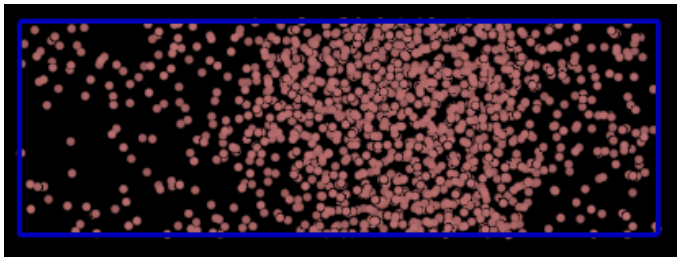

Figure A.1: A LJ fluid system with gas phase and liquid phase: (pink) LJ particles and (blue line) a simulation cell.

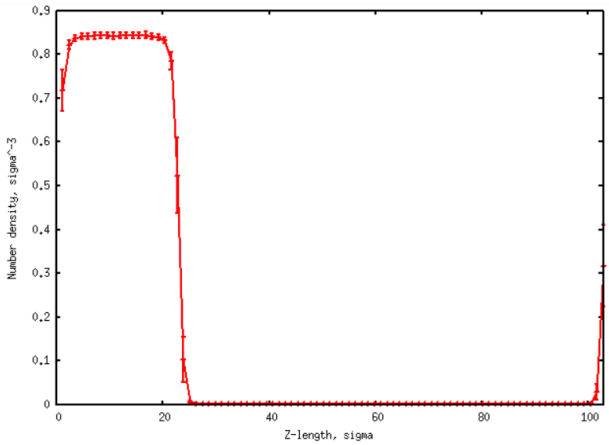


Figure A.2: An averaged density profile of 10,000 LJ particles at reduced temperature $T^* = 0.7$.

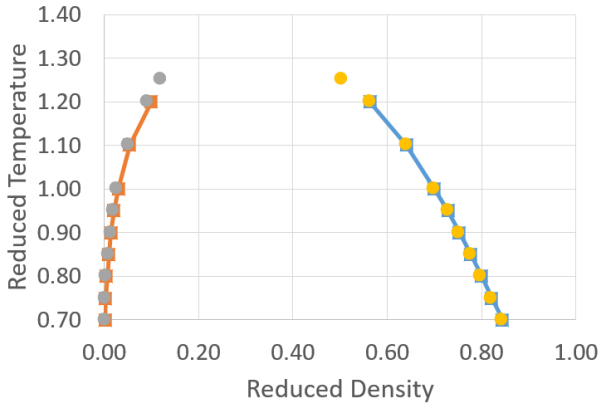


Figure A.3: The vapor-liquid equilibrium of LJ fluid: coexisting (gray circle) vapor phase and (yellow circle) liquid phase in this work and (square and line) a reference data using TMMC.[4] Error bars is small enough be within marks.

the averages of instantaneous enthalpy and volume which are acquired during 5,000 $\sigma^{-1}$. Nose-Hoover thermostat and Parrinello-Rahman barostat are used for NPT simulations at $T^*$ = 0.7, 0.75, 0.8, 0.85, 0.9, 0.95, 1, 1.1, 1.2, and 1.25.

As the result of the Gibbs-Duhem integration, Figure A.3 and Figure A.4 indicate that this preliminary study using the Gibbs-Duhem integration shows excellent agreement with a reference.[4]

# References

[1] David A Kofke. “Direct evaluation of phase coexistence by molecular simulation via integration along the saturation line”. In: *The Journal of chemical physics* 98.5 (1993), pp. 4149–4162.

[2] Rolf E Isele-Holder, Wayne Mitchell, and Ahmed E Ismail. “Development and application of a particle-particle particle-mesh Ewald method for dispersion interactions”. In: *The Journal of chemical physics* 137.17 (2012), p. 174107.

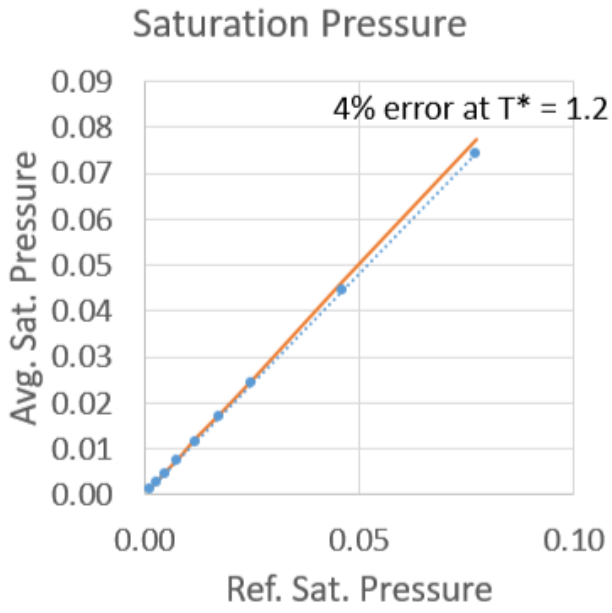


Figure A.4: Our saturation pressure with respect to reference data using TMMC.[4]

[3] Pieter J in't Veld, Ahmed E Ismail, and Gary S Grest. "Application of Ewald summations to long-range dispersion forces". In: *The Journal of chemical physics* 127.14 (2007), p. 144711.

[4] Jeffrey R Errington. "Direct calculation of liquid–vapor phase equilibria from transition matrix Monte Carlo simulation". In: *The Journal of chemical physics* 118.22 (2003), pp. 9915–9925.

[5] Jeffrey R Errington. "Evaluating surface tension using grand-canonical transition-matrix Monte Carlo simulation and finite-size scaling". In: *Physical Review E* 67.1 (2003), p. 012102.

[6] Fernando A Escobedo and Juan J de Pablo. "Pseudo-ensemble simulations and Gibbs–Duhem integrations for polymers". In: *The Journal of chemical physics* 106.7 (1997), pp. 2911–2923.

# Appendix B

# Anion Effects on the Phase Separation Behavior of Polymer in Ionic Liquids

In this appendix, we test several approach to estimate phase transition temperature and see anion effects on phase behavior of poly(ethylene oxide) (PEO) in [BMIM][$BF_4$] and [BMIM][$PF_6$].

## B.1 Simulation method

For our molecular simulation method, we use GROMACS 5.0.4 software package. As for force field of molecules, we take the force field parameters from our previous study for PEO and the OPLS/AA force field of ILs.[1] The detail of simulation parameters is the following: 2 $fs$ for time step using leapfrog integrator, constrained hydrogen bonds via LINC algorithm, and Smooth Particle-mesh Ewald (SPME) summation for calculating electrostatic field with cut-off distance, 1.4 $nm$, and PME order, 6. To simulate two phases with interfaces, we use $NP_zAT$ ensemble (cross area fixed cell under $P_z$ =1 $atm$) with Nose-hoover and Parrinello-Rahman couplings with pressure control on z-direction.

Our hypothesis for finding LCST-type phase transition temperatures is that the initial system with artificial two phases will disrupt at mixing temperatures $T < T_c$, then somewhat order pa-

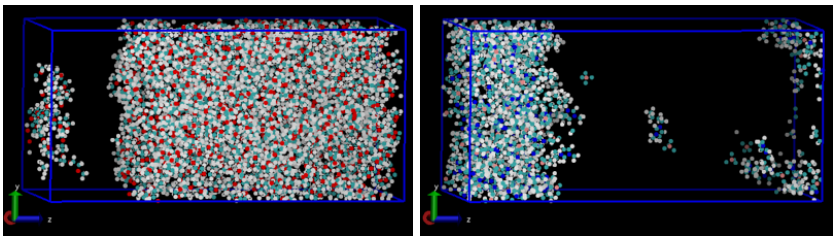

Figure B.1: Example of initial coordinates of pre-separated poly(ethylene oxide)/[BMIM][$BF_4$]; (left) PEO polymers (right) ionic liquids are only shown in a cell for visualization. Note that black empty regions are occupied by another component.

rameters should be significantly changed during phase transition. In order to make the initial coordinates of system at high temperature $T >> T_c$, the following steps are:

1. The randomly distributed 100 pairs of a IL and 127 chains of PEO ($CH_3$-[O-C-C]$_n$-O-$CH_3$, n=9) in a box ( 4 x 4 x 8 $nm$) is made.

2. The simulation box is equilibrated at 600 K. After 30 ns, the system quickly show separation phase, e.g. IL and polymer rich region.

3. Taken off the polymers, the system is filled by adding 127 chains of PEO and 5 pairs of the IL randomly, then the weight fraction of the system is $\sim$ 70 $wt\%$. The system is simulated for 120 $ns$ to reach equilibrium state, then we acquire data for at least another 600 $ns$ simulation time.

The example of final coordinate after previous steps is shown in Figure B.1. Using the single cell simulation, we discuss some properties in next section to figure out phase separation temperature of PEO/ILs; Local number fluctuation, heat capacity, and polymer conformation.

## B.2 Local number fluctuation during phase separation

To define the critical temperature, $T_c$, we use local number fluctuations as order parameter. Whereas single cell is performed under constant N and Pz with fixed xy-area, it is regarded as an ensemble

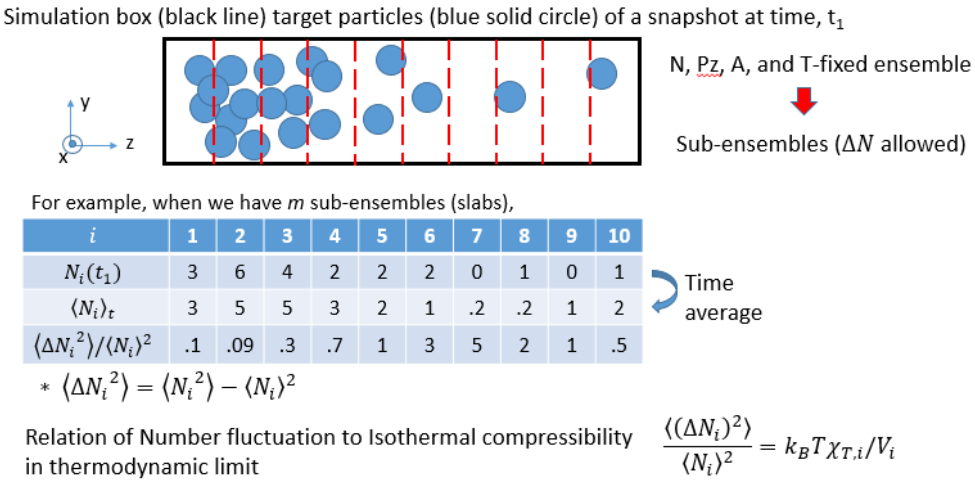


| $i$ | 1 | 2 | 3 | 4 | 5 | 6 | 7 | 8 | 9 | 10 |
|---|---|---|---|---|---|---|---|---|---|---|
| $N_i(t_1)$ | 3 | 6 | 4 | 2 | 2 | 2 | 0 | 1 | 0 | 1 |
| $\langle N_i \rangle_t$ | 3 | 5 | 5 | 3 | 2 | 1 | .2 | .2 | 1 | 2 |
| $\langle \Delta N_i^2 \rangle / \langle N_i \rangle^2$ | .1 | .09 | .3 | .7 | 1 | 3 | 5 | 2 | 1 | .5 |

Figure B.2: Pictorial images for slicing a single cell and the relations of local number fluctuations.

which contains many but tiny grand canonical sub-cells by slicing into slabs. (see figure B.2) In statistical mechanics, the number fluctuation of molecules in grand canonical ensemble has the following relation with compressibility:

$$\frac{\left\langle (\Delta N)^2 \right\rangle}{\langle N \rangle^2} = k_B T \chi_T / V \tag{B.1}$$

where difference between the number of particles and ensemble average number of particles, $N - \langle N \rangle = \Delta N$, Boltzmann constant, $k_B$, temperature, $T$, Volume, $V$, and isothermal compressibility, $\chi_T$ are shown. In practice, we choose local number fluctuations of (center of mass of) anions rather than cations or polymers. Due to the relatively compact sphere shape of anions and only translational motion, it would be easy to distinguish phase transition temperature from simulations at various temperatures.

The local number fluctuation of anions can be understood in terms of the relative amount of mass transfer of anions between neighbor slabs in polymer region. Under phase separation condition such as $T > T_c$, the average number of anions in the polymer-rich region is very low. Also, the change of the number of anions in the tiny cell would be relatively high by transferring just 1 or 2 anions from/to neighbor slabs. As a result, Figure B.3 shows the increase of local number

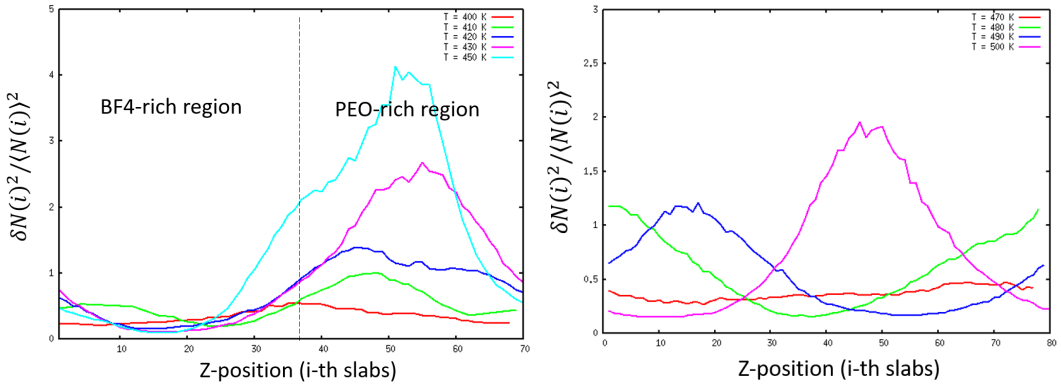


Figure B.3: Local number fluctuation distribution along z-axis slab at various temperature for (left) PEO/[BMIM][$BF_4$] and (right) PEO/[BMIM][$PF_6$]. Note that the slab thickness is around 0.12 nm.

fluctuation in the polymer-rich region with temperature.

In Figure B.3, we roughly estimate phase separation temperatures, 420 K and 480 K for PEO(n=9) in [BMIM][$BF_4$] and [BMIM][$PF_6$], respectively. The result indicates replacing [$BF_4$] with [$PF_6$] anion lowers solubility of PEO by $\sim 60K$. Considering the fact of weaker (attractive) cohesive energy between [BMIM] and [$PF_6$] than [$BF_4$],[2] the attractive interaction of [BMIM] cations and oxygen atoms of PEO by hydrogen bonding can be broken with higher thermal energy because of less electrostatic interactions between IL ions, which means enthalpy contribution. Note that we tried to obtain precise separation temperature, but the local number flucuation distribution becomes obscure due to fluctuation in time seen in Figure B.4.

## B.3 Heat capacity changes near transition temperature

As you can see many example of Differential scanning calorimetry (DSC) experimental data, heat capacity can be a good indicator for phase transition. From fluctuation-dissipation theory, the heat capacity becomes infinity at the transition temperature in macroscopic system; see Eq. B.2,

$$C_p = \frac{\sigma_H^2}{k_B T^2} = \frac{1}{k_B T^2}\left\langle (H - \langle H\rangle)^2 \right\rangle = \frac{1}{k_B T^2}\left[\left\langle H^2\right\rangle - \langle H\rangle^2\right] \tag{B.2}$$

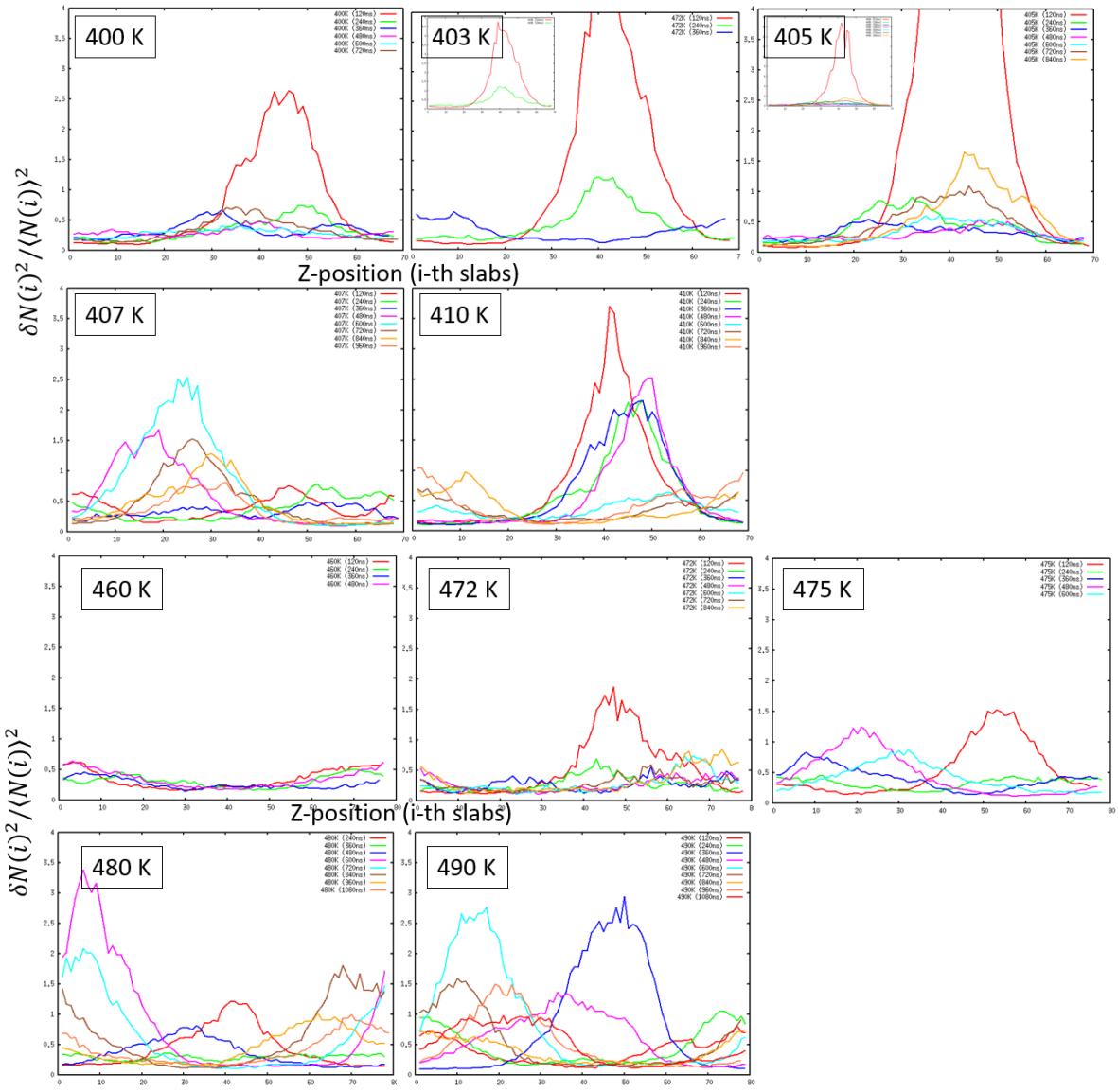


Figure B.4: Local number fluctuation distribution along z-axis slab at different time window and various temperature for (top) PEO/[BMIM][$BF_4$] and (bottom) PEO/[BMIM][$PF_6$]. Near phase transition temperature, the distribution fluctuates with a large magnitude within up to 1 $\mu s$ simulation time and it seems not to work to precisely get the temperature.

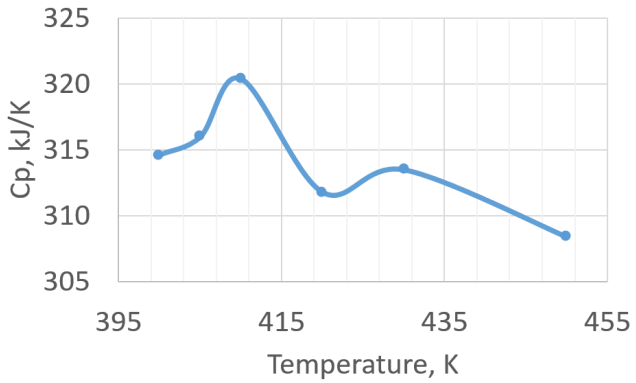


Figure B.5: Heat capacities at various temperatures at 70 wt% of polymers in PEO/[BMIM][$BF_4$]. Note that the error for $C_p$ is within 25 - 35 kJ/K.

where $H$ is the enthalpy of the mixture.

Figure B.5 shows the phase transition temperature of 70 wt% PEO/[BMIM][$BF_4$] could be $\sim$ 410 K where $C_p$ peak appears. Although the error of $C_p$ is too big (25 - 35 kJ/K) to figure out phase transition temperature, the estimated temperature does not match with the result of local number fluctuation. These discrepancy might be because the local number fluctuation and heat capacity could be affected with somewhat different extent by finite size effect. Also, the difference can be understood by the fact that phase transition point can vary with what experiment or analysis is used to figure out. In addition, the absolute $C_p$ value obtained by simulation is under lack of accuracy because most of force fields focused on intermolecular interactions, not intramolecular interactions which significantly contribute on internal energy $U$. A quantum calculation may be asked for a good quality of $C_p$ value to compare with experimental data, but it is not feasible for phase separation studies.

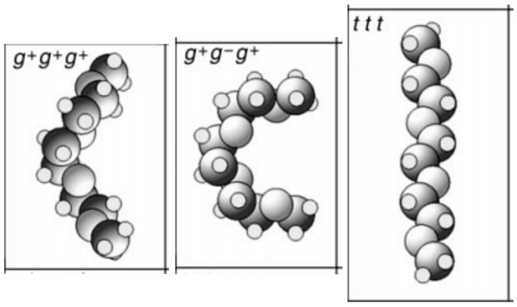


Figure B.6: Three representative segment conformations for poly(ethylene oxide). Reprinted from a quantum calculation study.[3]

Table B.1: The probability of finding conformer types for PEOs from last 120 ns trajectory. All values are in unit of percentage (%) except temperature $T$ in unit of kelvin.

| Anion in PEO/ILs | T | $g^+g^+g^+$ | $g^+tg^+$ | $tg^+t$ | $ttt$ | $g^+g^+t$ | $g^+tt$ |
|---|---|---|---|---|---|---|---|
| $BF_4$ | 390 | 29.4 | 11.2 | 9.4 | 3.7 | 33.0 | 13.2 |
| | 450 | 30.7 | 11.9 | 8.1 | 3.6 | 32.3 | 13.4 |
| $PF_6$ | 390 | 29.1 | 11.2 | 9.7 | 3.6 | 33.1 | 13.2 |
| | 460 | 30.7 | 12.0 | 8.3 | 3.5 | 32.2 | 13.3 |
| | 500 | 31.3 | 12.4 | 7.7 | 3.4 | 31.8 | 13.4 |

## B.4 Polymer conformations below/above phase separation temperature

The idea is to check if polymers have different structures depending on two-phase or one-phase. In polymer physics, polymer chains expand at good solvent but form polymer coils at poor solvent. Relating with LCST behavior of PEO/ILs, the solubility of IL decreases as temperature increase like the analogy of a transition from good solvent to poor solvent for PEOs. Conventional polymer properties such as radius of gyration and end-to-end distance of polymer change little for a short chain length of polymer. Instead, we use the distribution of polymer conformer types which characterises gauche or trans angles of C-O-C-C and O-C-C-O on single PEO backbone.[3] Our preliminary result in Table B.1 shows the general trend but not steep change to figure out phase transition.

## B.5 Conclusion

We use several approaches to obtain phase separation temperature at a given temperatures and the result of local number fluctuation shows that weak interaction between [BMIM] and [$PF_6$] lower the solubility of PEO as $T_c$ increases. The change of heat capacity and polymer conformation during phase transition is very weak to recognize transition. Instead, the local number fluctuation can be a good indicator for phase separation, but still difficult to accurately assign phase boundary. As another disadvantage, while alignment algorithms described in Introduction chapter can obtain two compositions at once from single simulation at a given temperature, this method is somewhat expensive because it requires all simulations at different concentrations.

# References

[1] Eunsong Choi and Arun Yethiraj. "Entropic mechanism for the lower critical solution temperature of poly (ethylene oxide) in a room temperature ionic liquid". In: *ACS Macro Letters* 4.7 (2015), pp. 799–803.

[2] Jesse G McDaniel et al. "Ab initio force fields for imidazolium-based ionic liquids". In: *The Journal of Physical Chemistry B* 120.28 (2016), pp. 7024–7036.

[3] Richard LC Wang, H Jürgen Kreuzer, and Michael Grunze. "The interaction of oligo (ethylene oxide) with water: a quantum mechanical study". In: *Physical Chemistry Chemical Physics* 2.16 (2000), pp. 3613–3622.

# Appendix C

# Examples of Prediction of the Critical Point: A Simulation Study of PEO/ILs with OPLS-AA Force Field

In this Appendix, our goal is to show the predicted critical point of poly(ethylene oxide) (PEO) in [BMIM][$BF_4$] with the conventional OPLS-AA force field. For prediction of the critical point, we utilize critical exponents and some points on phase boundary obtained by the Convolution method we described in Chapter 2. Although we did not check the finite size effect on phase coexistence due to limited resource and time, we show our preliminary result as an example of those methods for PEO/IL mixtures.

## C.1 Simulation method

To obtain the mass fractions of PEOs in coexisting phases, we perform direct simulations of the mixtures using GROMACS 5 software package. As for an initial configuration, we prepared the coordinate of coexisting phases at 600 K. Initially, for a 50 wt% PEO solution, 255 short PEO chains ($CH_3$-[O-C-C]$_n$-O-$CH_3$ for n = 9), and 500 pairs of [BMIM][$BF_4$] are randomly distributed

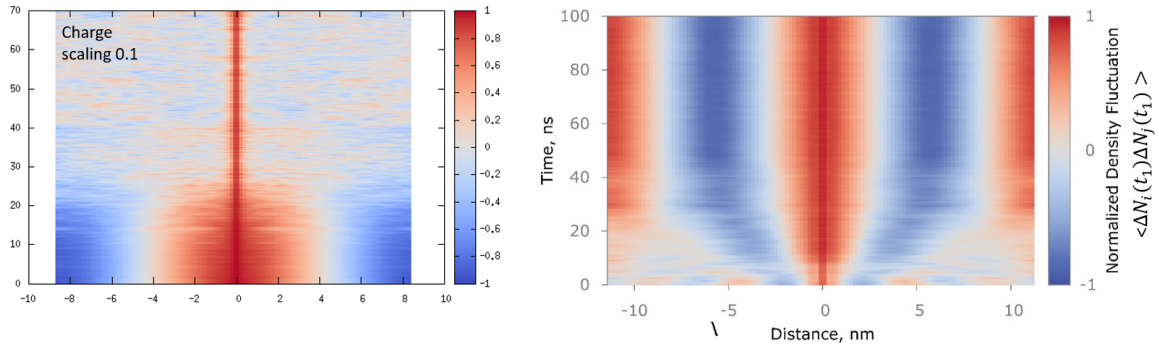


Figure C.1: Example of density profiles in time for poly(ethylene oxide)/[BMIM][$BF_4$] at mixing and separation temperature; (left) the mixing phase made by scaling charge by a tenth (right) separation phase at 560 K. While separation phase forms large size of domains in middle of cell, the domain mostly disappears under mixing.

in a parallelepiped box, $L$ x $L$ x $\sim 5L$. Note that $L$ = 4.2 nm which is bigger than 1.4 nm for cut-off distance of Lennard-Jones Particle Mesh Ewald (LJ-PME) method. The system is equilibrated for 100 ns at 600 K ($\gg T_c$) and 1 bar with Nose-Hoover thermostat and Parrinello-Rahman barostat. Then, the equilibrated system at 600 K is regarded as initial coordinates for simulations at 440 K $\leq$ T $<$ 600 K. At lower temperatures, 400 K $\leq$ T $<$ 440 K, we found the domain size of phases is not equal, which prevents getting phase boundary effectively. Thus, we use a system of 280 PEO chains with n = 9, and 300 IL pairs for 65 wt% PEO solution, which allows to obtain similar domain size for coexisting phases in a cell.

To check if the equilibrium can reach from mixing phase, we additionally simulate randomly oriented coordinates. The initial mixing phases are prepared by artificially scaling charge down to 10 times smaller for a 100 ns simulation . You can see example of concentration profiles in time using Convolution method for mixing and separated system in Figure C.1. The simulations run up to 1 $\mu$s and the last few hundreds nanoseconds trajectories are used for averaged density profiles. Figure C.2 shows raw and aligned concentration profile at 420 K as a result of the Convolution method. Table C.1 summarizes configurations of our simulations to get some points on phase boundary.

All simulations run with the following settings: Verlet integrator, $NP_zAT$ ensemble where x

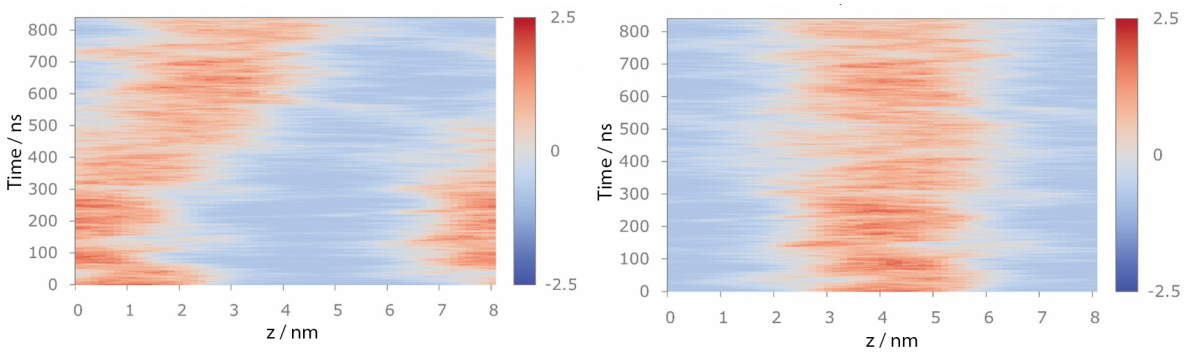


Figure C.2: Example of density profiles of [$BF_4$] in time for poly(ethylene oxide)/[BMIM][$BF_4$] at 420 K; (left) raw density profile (right) aligned density profile using the Convolution method.

Table C.1: Summary of simulation cell settings for initial coordinates of PEO/[BMIM][$BF_4$]. Note that sep. and mix. in the last column mean pre-seperated cell and mixing cell, respectively.

| $L_x$, nm | $L_z$ | $N_{PEO}$:$N_{IL}$ $_{pairs}$ | T, K | time, $\mu s$ | Note |
|---|---|---|---|---|---|
| 4.2 | $\sim 5\ L_x$ | 255:500 (50 wt%) | 600 | 0.1 | sep. |
| | | | 540 | 0.3 | sep. |
| | | | | 0.1 | mix. |
| | | | 480 | 1.2 | sep. |
| | | | | 0.1 | mix. |
| | | | 440 | 1.2 | sep. |
| | | | | 0.1 | mix. |
| 4.0 | $\sim 2\ L_x$ | 127:105 (71 wt%) | 430 | 0.75 | sep. |
| | | | 420 | 0.85 | |
| | | | 410 | 0.95 | |
| | | | 400 | 0.65 | |
| 4.2 | $\sim 4\ L_x$ | 280:300 (65 wt%) | 380 | 0.1 | mix. |

and y length of simulation box are fixed, and periodic boundary condition (PBC). As for long range correction for Van der Waals interaction, we use LJ-PME method recently implemented in Gromacs 5 to handle spatially heterogeneous interactions with good accuracy. The PME parameters for electrostatic and dispersion interaction are the same: real space cut off distance of 1.4 nm, grid spacing of 0.12 nm, and interpolation order of 6.

## C.2 The prediction of the critical point using critical exponents

Aligned number density profiles are block-averaged using the last a few hundred nanosecond trajectories. Then, for the precise number densities of two components in coexisting phases, we fit the density profiles with hyperbolic tangent model,

$$\rho_{IL}(z) = \rho_{IL}^{poor} + \frac{\rho_{IL}^{rich} - \rho_{IL}^{poor}}{2} \left[ \tanh\left( \frac{z - z_{center}^{rich} + z_{half-width}^{rich}}{\lambda_{interface}} \right) - \tanh\left( \frac{z - z_{center}^{rich} - z_{half-width}^{rich}}{\lambda_{interface}} \right) \right] \tag{C.1}$$

, where $\rho_{IL}^{poor}$ is the number density of BF[$_4$] in anion-poor region, $z_{center}$ is the position of center of anion-rich region, $z_{half-width}$ is the half-width of anion-rich region, and $\lambda_{interface}$ is the width of interface. As for fitting number density of anion with Eq. C.1, the nonlinear least-squares (NLLS) Marquardt-Levenberg algorithm implemented in GNUPLOT is used. Those analysis procedures are also used to obtain coexisting mass fractions of PEO in two-phase cell. The some results of coexisting mass fraction at various temperature are shown in Figure C.3. Note that we do not use number density profiles at $T \leq 420$ K due to no flat region for PEO or IL-rich phase.

To extrapolate the critical point, we fit our coexisting data with Eq. 1.3 and Eq. 1.4 for OPLS-AA and SAPT-UA force field from Chapter 4. Be aware that our simluation data is far from the critical point which means the fitting equations would fail in the extrapolation of the critical point. As the fitting result, the LCST point of PEO/[BMIM][BF$_4$] is predicted at 390 K and 76 wt% of polymers for OPLS-AA force field and 260 K and 50 wt% for SAPT-UA force field. We do not rigorously investigate the finite size effect on phase boundary with OPLS-AA force field and

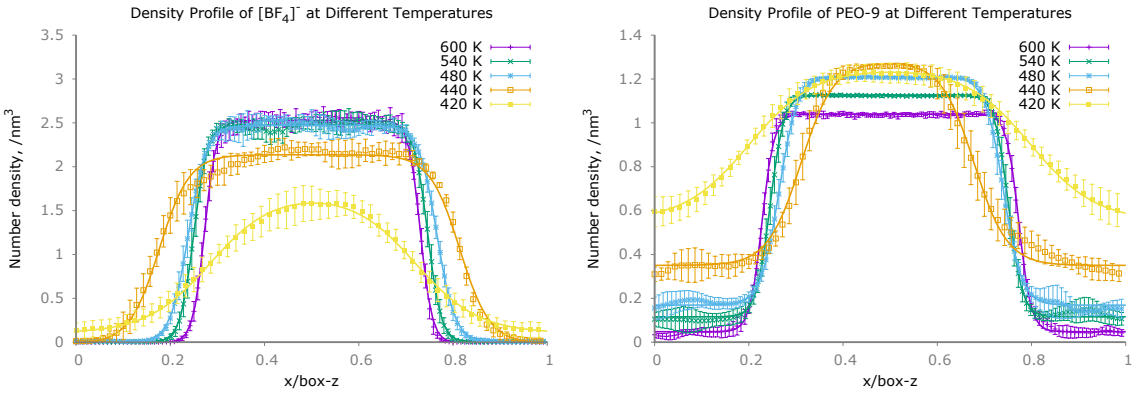


Figure C.3: The block averaged number density profile of (left) [$BF_4$] anions and (right) PEO polymers with respect to temperatures using the Convolution method. Solid lines show a fit with a hyperbolic tangent model in Eq. C.1.

the validation of machine learning method. In Figure C.6 and Figure C.7, we see that machine learning results fairly fit with 3D Ising critical exponents for critical temperature. However, as for prediction of critical weight concentration, an additional work might be needed for a better result by searching a good property to represent the critical point.

We easily see the big difference of $T_c$ depending on force fields. Comparing with SAPT-UA force field result, the result of OPLS-AA force field shows less solubility of PEOs in ILs and very low solubility of ILs in PEO melts, which contributes lower predicted $T_c$ and asymmetric curve toward to the higher weight fraction of PEOs. Unfortunately, because of limited experimental data for phase diagram of PEO/ILs, we could not know which force field is better or not. To fill the gap between experiments and simulations, a study of effects of terminal group and shorter chain length of polymer in [BMIM] cation and [$BF_4$] anion would be worth to confirm the accuracy of those force fields.

# References

[1] Hau-Nan Lee et al. “Unusual lower critical solution temperature phase behavior of poly (ethylene oxide) in ionic liquids”. In: *Macromolecules* 45.8 (2012), pp. 3627–3633.

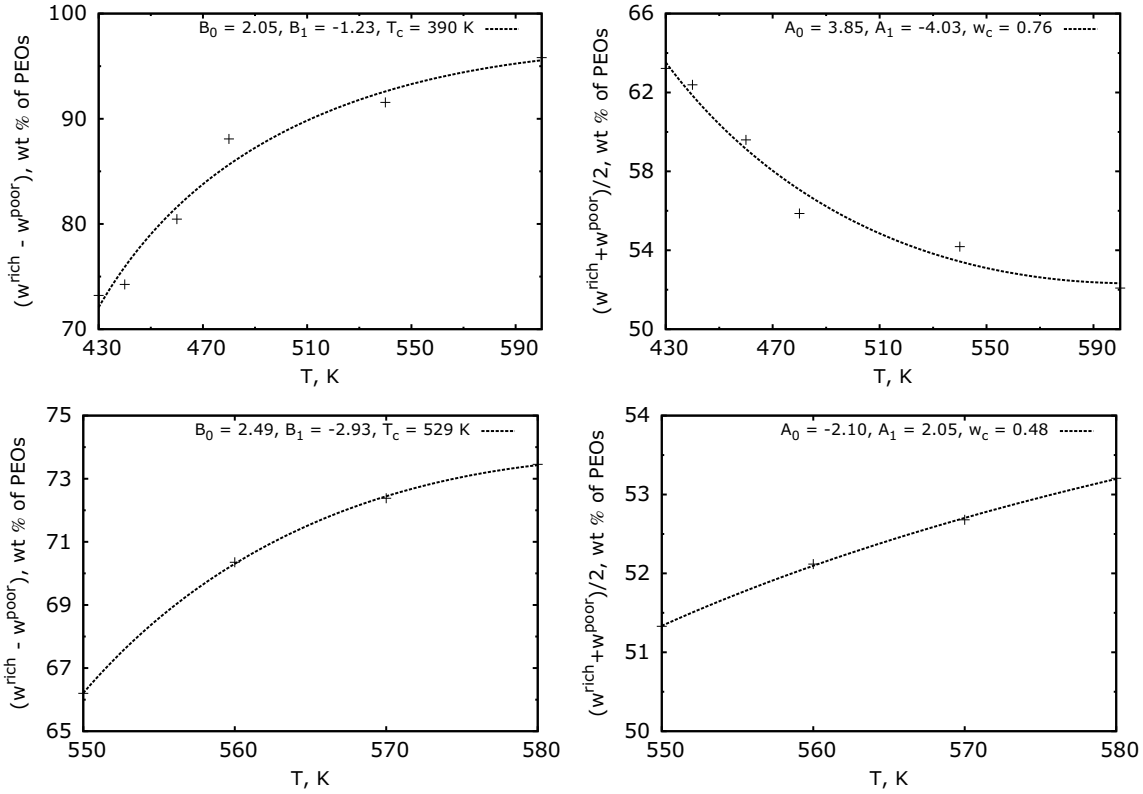


Figure C.4: The fitting plots of the left side of (left) Eq. 1.3 and (right) Eq. 1.4 with respect to temperature using 3D Ising critical exponents for phase boundary with SAPT-UA and OPLS-AA force field. Solid lines are the fitting curve with optimal parameters.

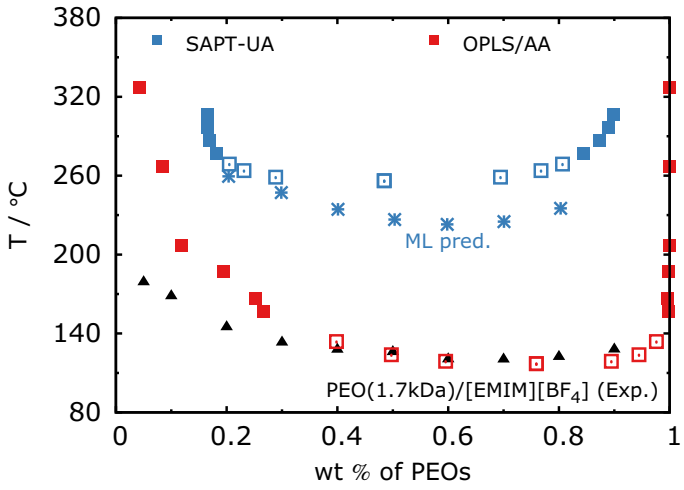


Figure C.5: Phase diagrams of PEO (0.4 KDa) /[BMIM][$BF_4$] with (blue) SAPT-UA force field and machine learning and (red) with OPLS-AA force field and critical exponents. Filled box points mean the result of MD simulation and the Convolution method. Blue and red color of empty box points are predicted using artificial neural network and 3D Ising critical exponents, respectively. Note that Black points are experimental data for PEO/[EMIM][$BF_4$].[1].

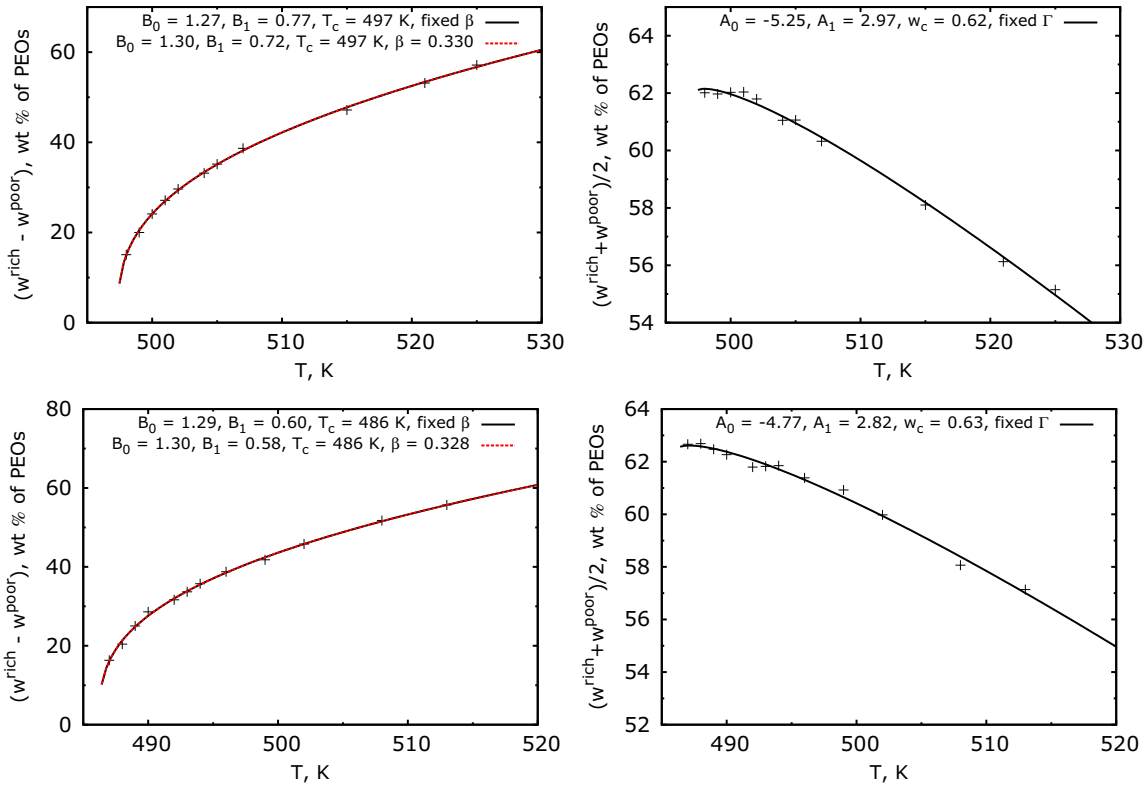


Figure C.6: The fitting plots of the left side of (left) Eq. 1.3 and (right) Eq. 1.4 with respect to temperature using 3D Ising critical exponents for phase boundary with SAPT-UA force field for (top) PEO/[BMIM][$BF_4$] and (bottom) PEO/[BMMIM][$BF_4$]. Black and red lines are the fitting curves with optimal parameters when both $\beta$ and $\Gamma$ is fixed and changeable to fit, respectively. Because we did not see significant change on $\Gamma$, we show the curves only with flexible $\beta$.

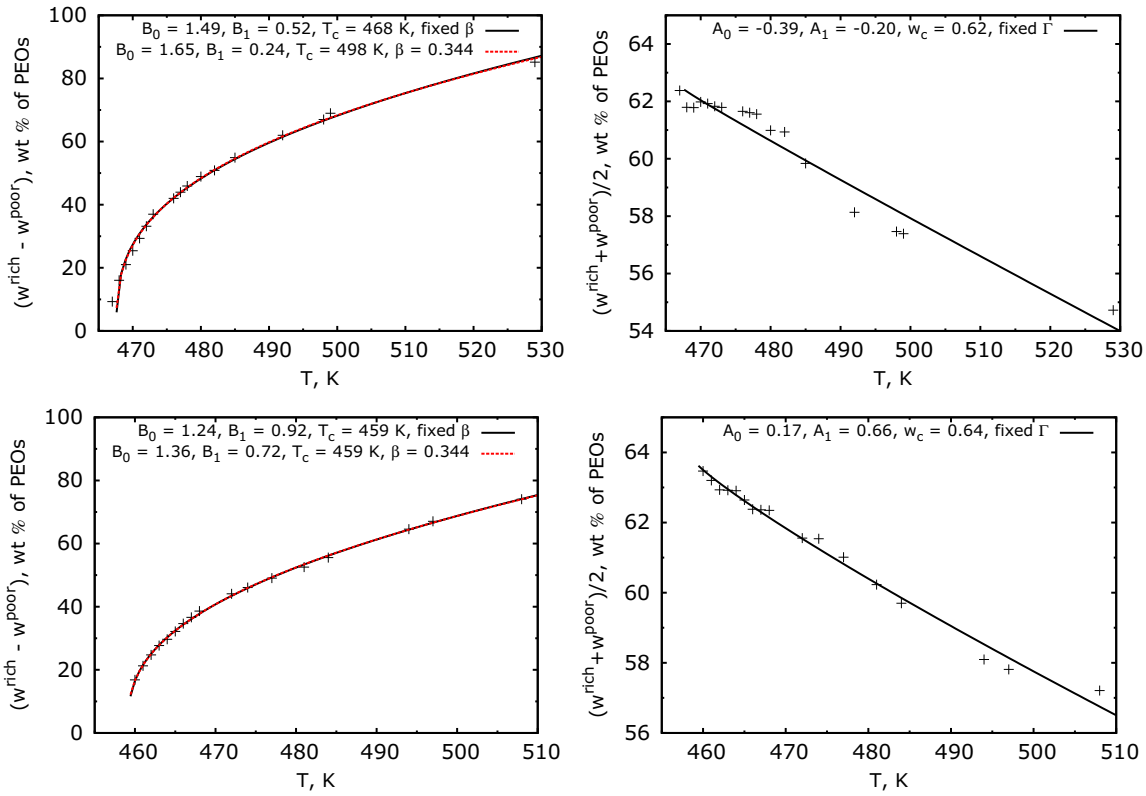


Figure C.7: The fitting plots of the left side of (left) Eq. 1.3 and (right) Eq. 1.4 with respect to temperature using 3D Ising critical exponents for phase boundary with SAPT-UA force field for (top) PEO/[EMIM][$BF_4$] and (bottom) PEO/[EMMIM][$BF_4$]. Other notation is the same as Fig. C.6

# Appendix D

# Supporting Information for "Methylation Effect on Phase Separation Behavior of Poly(ethylene oxide) and Imidazolium Ionic Liquids Mixture: A Molecular Dynamics and Deep Neural Network Study"

## D.1 SAPT-UA force field parameters

The total nonbonded interaction energy in SAPT-UA force field is given by

$$E_{tot} = \sum_{i,j} \frac{q_i q_j}{r_{ij}} + \sum_{i,j} \left( A_{ij}^{tot} \exp\left(-B_{ij} r_{ij}\right) - \sum_{n=6,8,10,12} f_{n,ij} \frac{C_n^{ij}}{r_{ij}^n} \right) \tag{D.1}$$

where $r_{ij}$ is the distance between $i$ and $j$ particles, $A_{ij}^{tot} = A_{ij}^{exch} + A_{ij}^{elec} + A_{ij}^{ind} + A_{ij}^{dhf}$, and $f_{n,ij}$ is Tang-Toennies damping function.[1]

Table D.1: The partial charges of united atom types of [EMIM], [EMMIM], and [BMMIM] cations. See Fig. 4.1 for atomtype names.

| Atom type | [EMIM] | [EMMIM] | [BMMIM] |
|---|---|---|---|
| N | -0.6754 | -0.6772 | -0.5945 |
| CM | - | 0.2527 | 0.2439 |
| C1 | 0.3040 | 0.3630 | 0.3366 |
| C2 | 0.6944 | 0.3271 | 0.2604 |
| C3 | 0.5165 | 0.5165 | 0.4886 |
| C4 | 0.4585 | 0.4585 | 0.4608 |
| C5 | - | - | -0.0053 |
| CE | 0.0734 | 0.0734 | 0.0728 |

Table D.2: SAPT-UA force fields of atom types for the nonbonded interaction potential in Eq. D.1. As for B values in , we use 39.061 $\mathring{A}^{-1}$ for N atom type and otherwise, 34.384 $A^{-1}$ for other atom types. Note that $A_i$'s are in $kJ/mol$ and $C_n$ are in $kJ/(mol\mathring{A}^{-n})$

| Atom type | $A_{exch}$ | $A_{elec}$ | $A_{ind}$ | $A_{dhf}$ |
|---|---|---|---|---|
| N | 252624.4 | 102233.5 | 0.0 | 17537.3 |
| C1, C2 | 869803 | 253355 | 0.0 | 94498.0 |
| CM, C3, CE | 2620353 | 765461 | 43780 | 144620 |
| C4, C5 | 3038134 | 922261.5 | 65333 | 188853 |

| Atom type | $C_6$ | $C_8$ | $C_{10}$ | $C_{12}$ |
|---|---|---|---|---|
| N | 1018.7 | 6246.0 | 92197.5 | 676941.7 |
| C1, C2 | 2211.4 | 24830.1 | 149571 | 295630 |
| CM, C3 | 3893.1 | 43280.5 | 430425 | 3438615 |
| C4 | 2186.6 | 16556.1 | 309338 | 2831947 |
| C5 | 2937.7 | 42270.1 | 566233 | 6097084 |
| CE | 5165.3 | 67458.1 | 848542 | 8569083 |

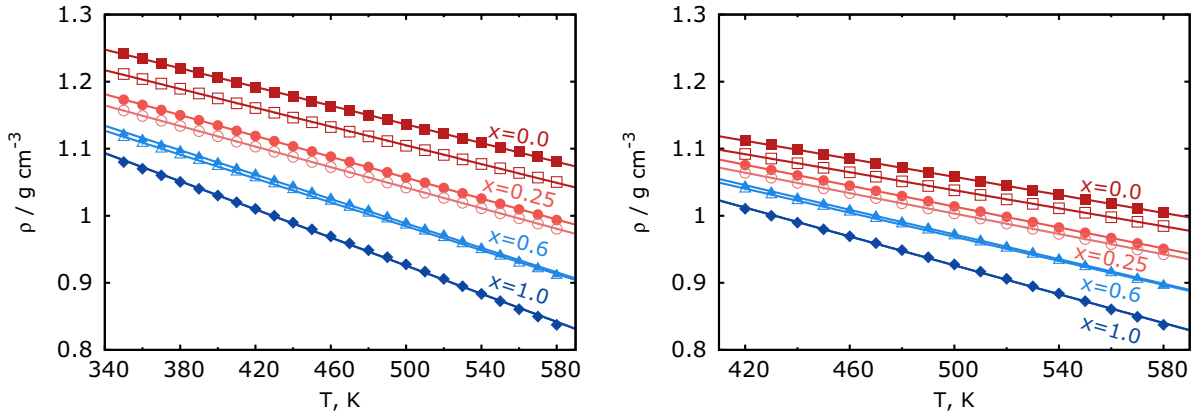


Figure D.1: Variation of density for (left) PEO/[EMIM][$BF_4$] and PEO/[EMMIM][$BF_4$] and (right) PEO/[BMIM][$BF_4$] and PEO/[BMMIM][$BF_4$] mixtures for several mole fractions of PEOs, $x$'s, and the studied temperature range. Note that filled and empty symbols represent [$C_n$MIM] and [$C_n$MMIM] cations in mixtures, respectively. The solid lines represent a fit to the equation $\rho = \rho_0 + aT$.

## D.2 Thermophysical properties: density and excess molar volume

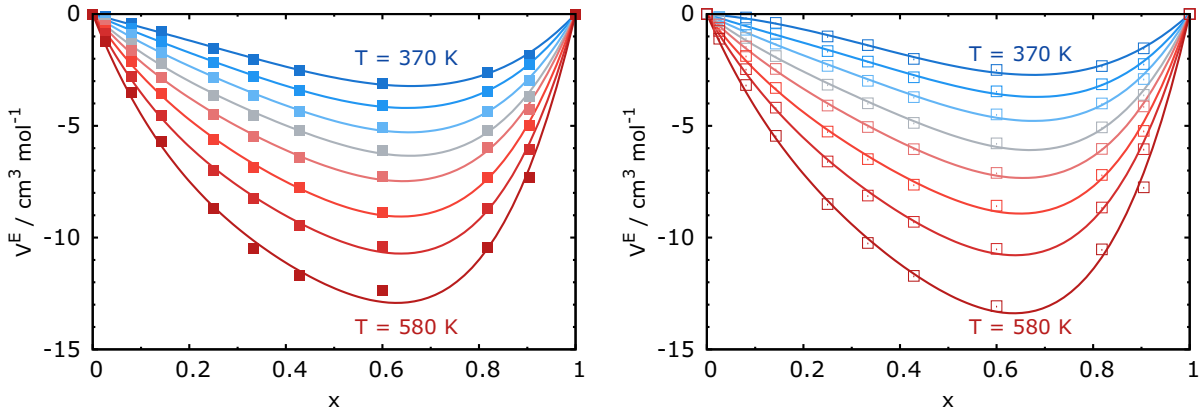


Figure D.2: Variation of molar excess volume of (left) PEO/[EMIM][$BF_4$] and (right) PEO/[EMMIM][$BF_4$] mixtures as a function of mole fraction of PEOs. The color of lines represents temperature from 370 K to 580 K with interval 30 K. Solid and dashed curves show fits according to the Redlich-Kister equation.

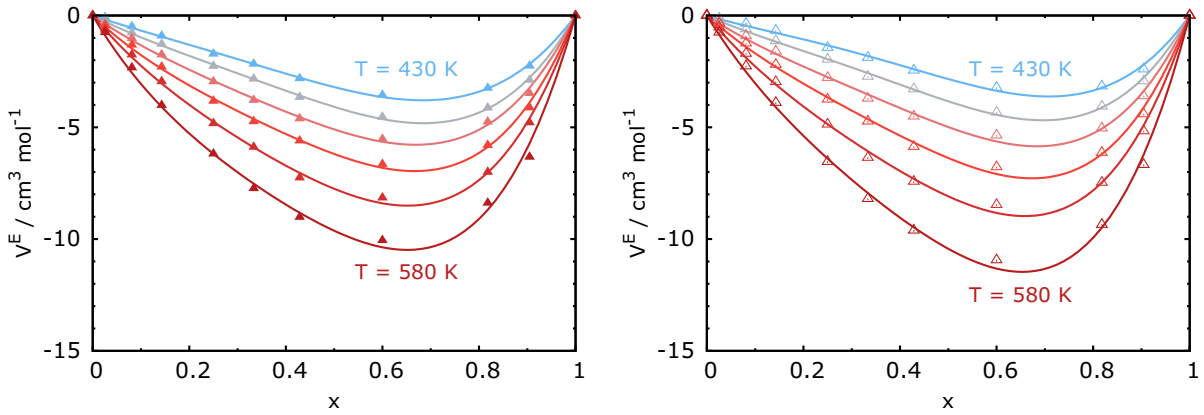


Figure D.3: Variation of molar excess volume of (left) PEO/[BMIM][$BF_4$] and (right) PEO/[BMMIM][$BF_4$] mixtures as a function of mole fraction of PEOs. The color of lines represents temperature from 430 K to 580 K with interval 30 K. Solid and dashed curves show fits according to the Redlich-Kister equation.

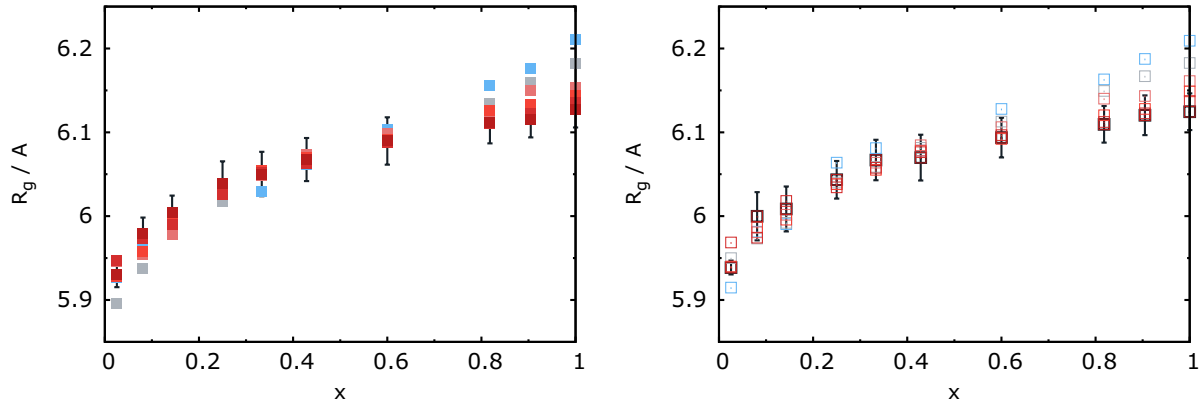


Figure D.4: Variation of radius of gyration of (left) PEO/[EMIM][$BF_4$] and (right) PEO/[EMMIM][$BF_4$] mixtures as a function of mole fraction of PEOs. The color of lines represents temperature from 370 K to 580 K with interval 30 K, which is the same as Fig. D.2. The y-error bar (black) is the standard deviation at 580 K (red).

## D.3 Polymer conformations: radius of gyration and end-to-end distance of poly(ethylene oxide)

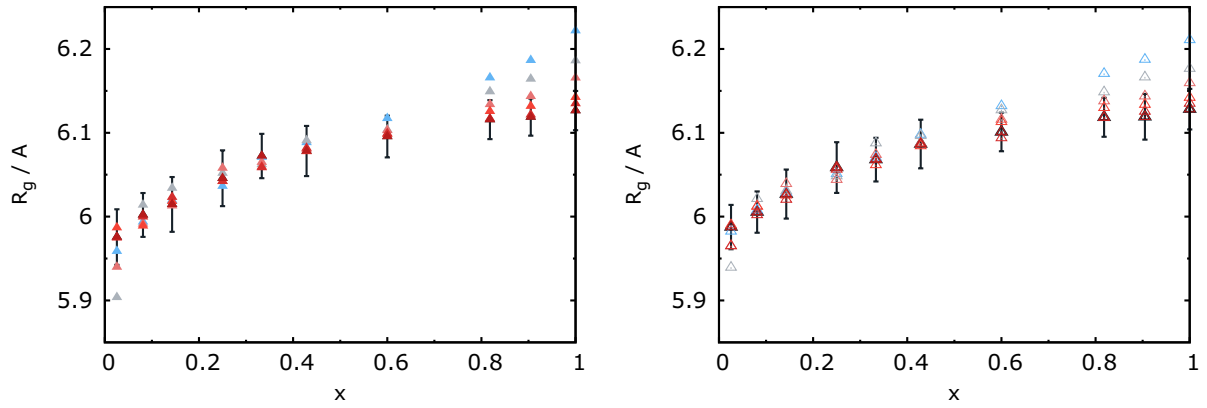


Figure D.5: Variation of radius of gyration of (left) PEO/[BMIM][$BF_4$] and (right) PEO/[BMMIM][$BF_4$] mixtures as a function of mole fraction of PEOs. The color of lines represents temperature from 430 K to 580 K with interval 30 K, which is the same as Fig. D.3. The y-error bar (black) is the standard deviation at 580 K (red).

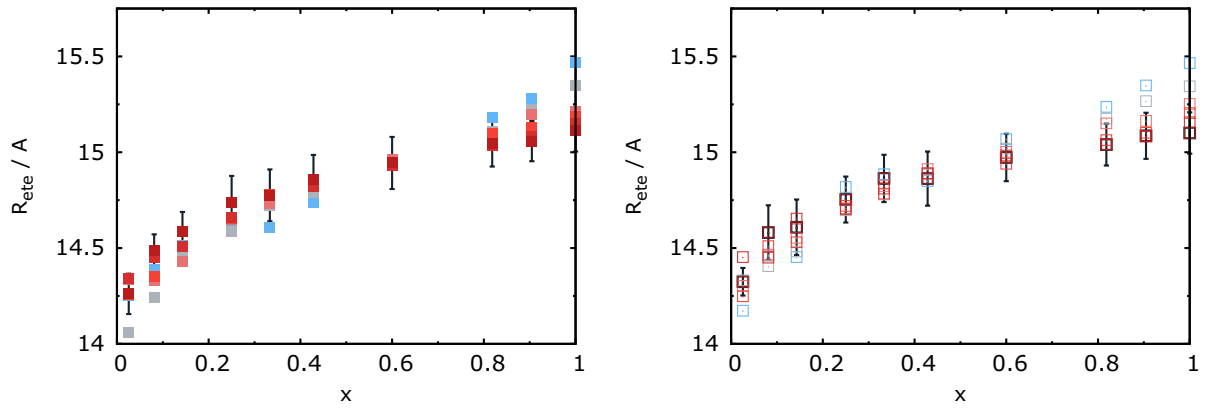


Figure D.6: Variation of end-to-end distance of (left) PEO/[EMIM][$BF_4$] and (right) PEO/[EMMIM][$BF_4$] mixtures as a function of mole fraction of PEOs. The color of lines represents temperature from 370 K to 580 K with interval 30 K, which is the same as Fig. D.2. The y-error bar (black) is the standard deviation at 580 K (red).

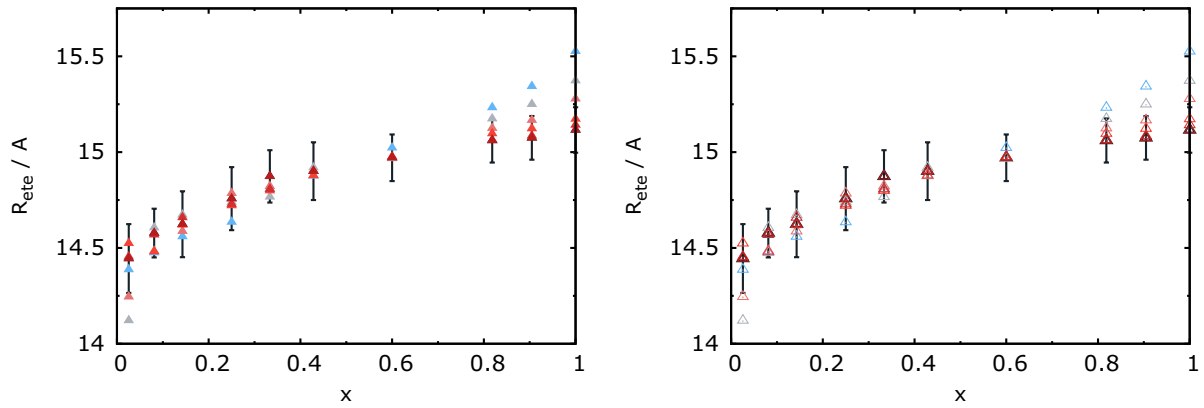


Figure D.7: Variation of end-to-end distance of (left) PEO/[BMIM][$BF_4$] and (right) PEO/[BMMIM][$BF_4$] mixtures as a function of mole fraction of PEOs. The color of lines represents temperature from 430 K to 580 K with interval 30 K, which is the same as Fig. D.3. The y-error bar (black) is the standard deviation at 580 K (red).

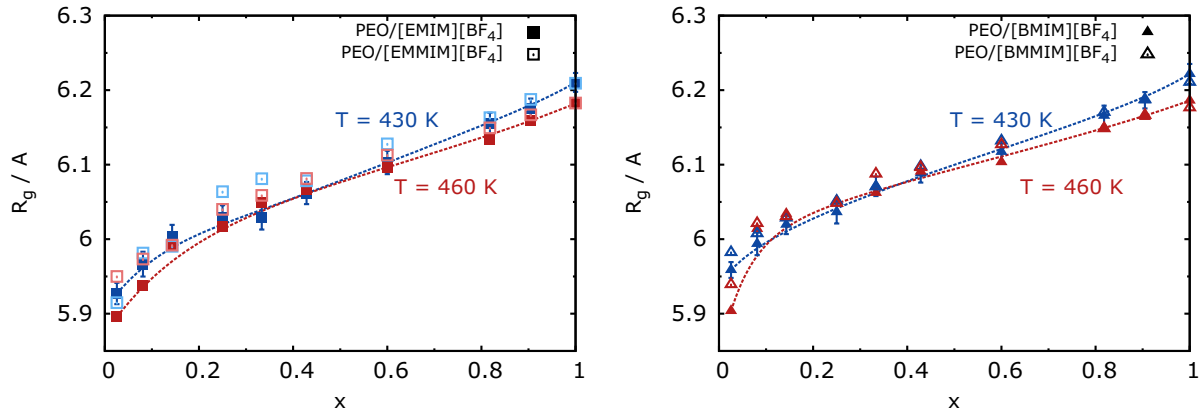


Figure D.8: Plots of radius of gyration and end-to-end distance of polymers in (left) PEO/[EMIM][$BF_4$] and PEO/[EMMIM][$BF_4$] and (right) PEO/[BMIM][$BF_4$] and PEO/[BMMIM][$BF_4$] as a function of mole fraction of PEOs at 430 K and 460 K. The y-error bar is the block average error of PEO/[BMIM][$BF_4$] at 430 K. Dotted lines serve as eye-guide lines for PEO/[$C_n$MIM][$BF_4$] mixture.

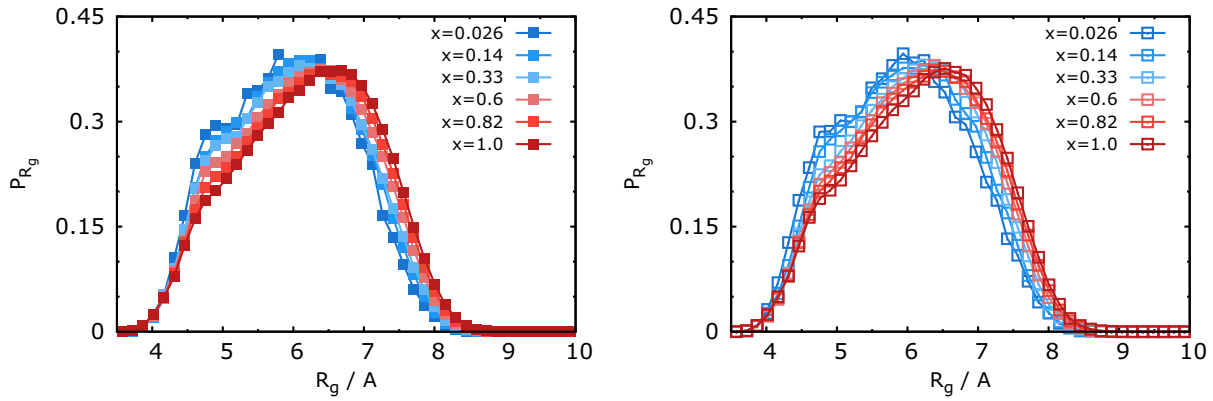


Figure D.9: Probabilities of $R_g$ of PEOs for (left) PEO/[EMIM][$BF_4$] and (right) PEO/[EMMIM][$BF_4$] as a function of mole fractions of PEOs at 430 K.

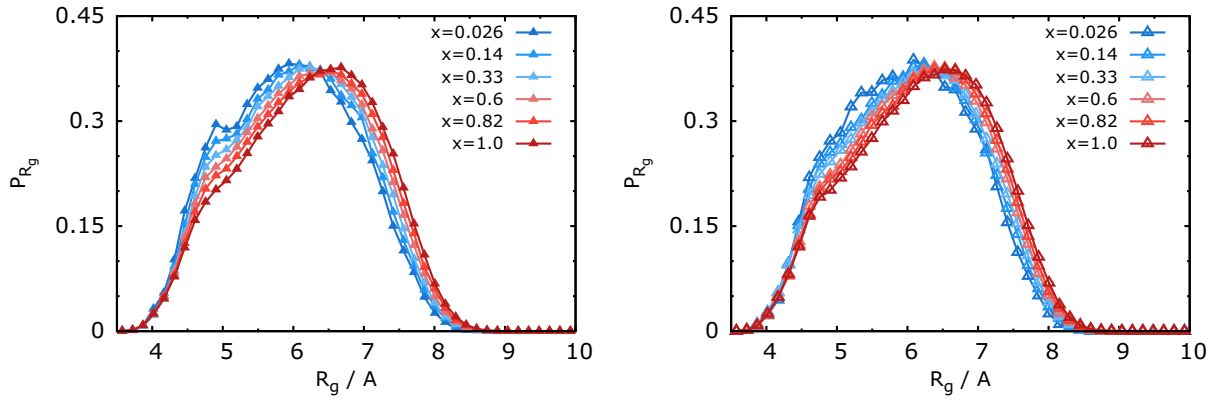


Figure D.10: Probabilities of $R_g$ of PEOs for (left) PEO/[BMIM][$BF_4$] and (right) PEO/[BMMIM][$BF_4$] as a function of mole fractions of PEOs at 430 K.

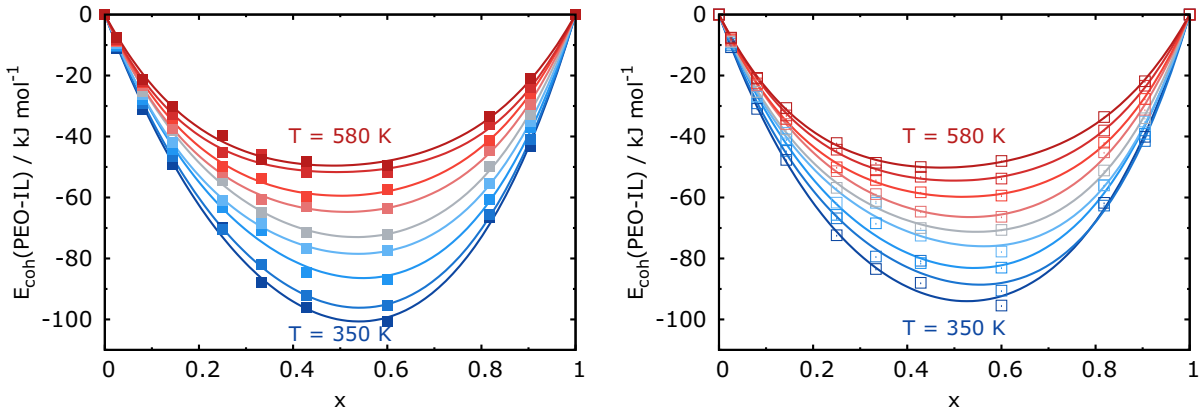


Figure D.11: Variation of molar cohesive energy of (left) PEO/[EMIM][$BF_4$] and (right) PEO/[EMMIM][$BF_4$] mixtures as a function of mole fraction of PEOs. The color of lines represents temperature from 370 K to 580 K with interval 30 K, which is the same as Fig. D.2.

## D.4 Molar cohesive energy between PEO and ILs

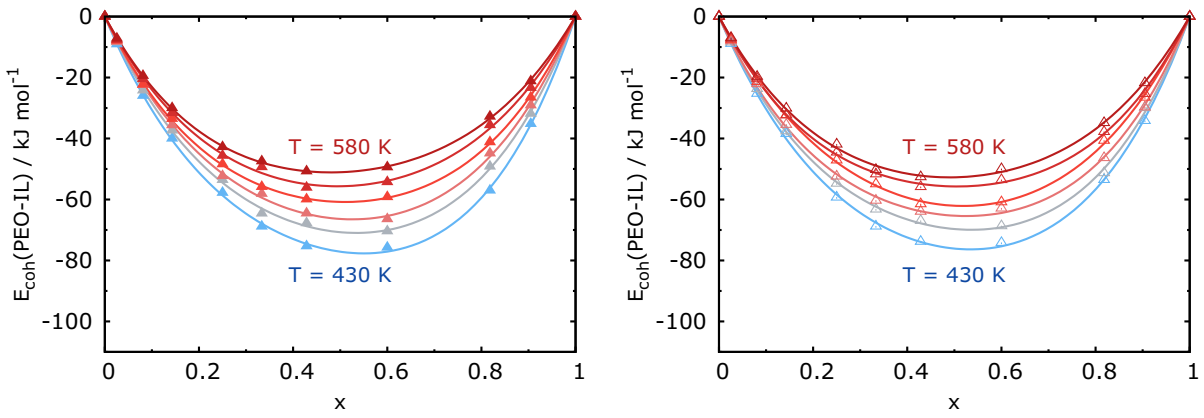


Figure D.12: Variation of molar cohesive energy of (left) PEO/[BMIM][$BF_4$] and (right) PEO/[BMMIM][$BF_4$] mixtures as a function of mole fraction of PEOs. The color of lines represents temperature from 430 K to 580 K with interval 30 K, which is the same as Fig. D.3.

## D.5 Pair correlation functions of atoms in mixtures

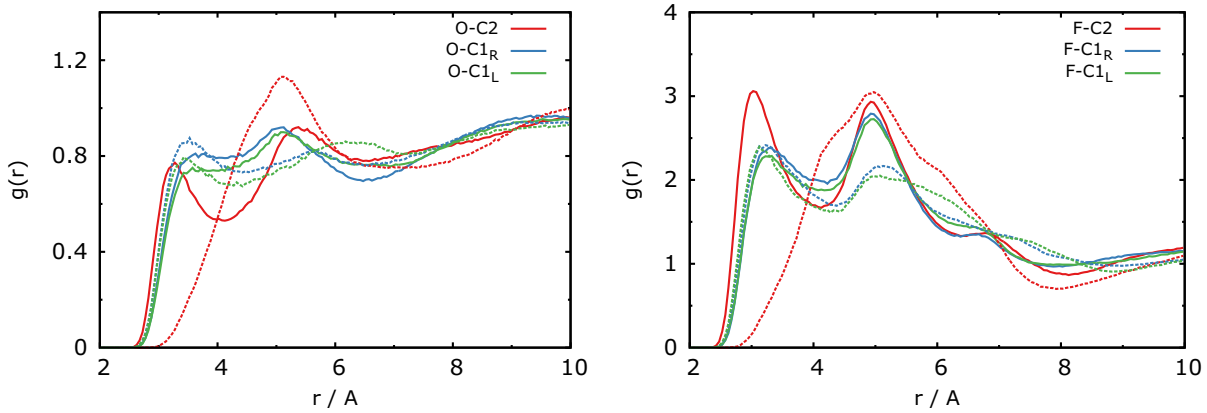


Figure D.13: Variation of radial distribution functions of (left) oxygen atoms of PEOs and (right) flourine atoms of [$BF_4$] anions. Solid lines and dashed lines are for PEO/[EMIM][$BF_4$] mixture and PEO/[EMMIM][$BF_4$] mixtures at 430 K for x=0.43, respectively.

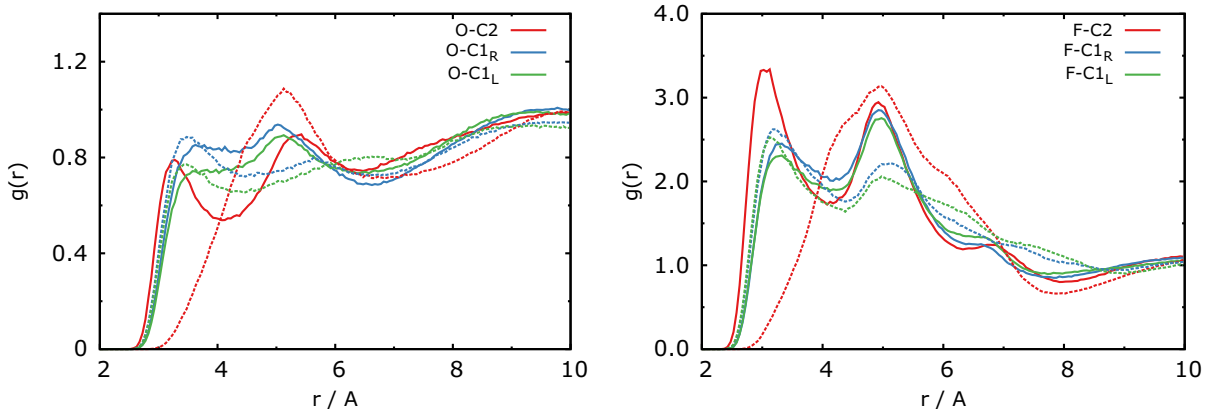


Figure D.14: Variation of radial distribution functions of (left) oxygen atoms of PEOs and (right) flourine atoms of [$BF_4$] anions. Solid lines and dashed lines are for PEO/[BMIM][$BF_4$] mixture and PEO/[BMMIM][$BF_4$] mixtures at 430 K for x=0.43, respectively.

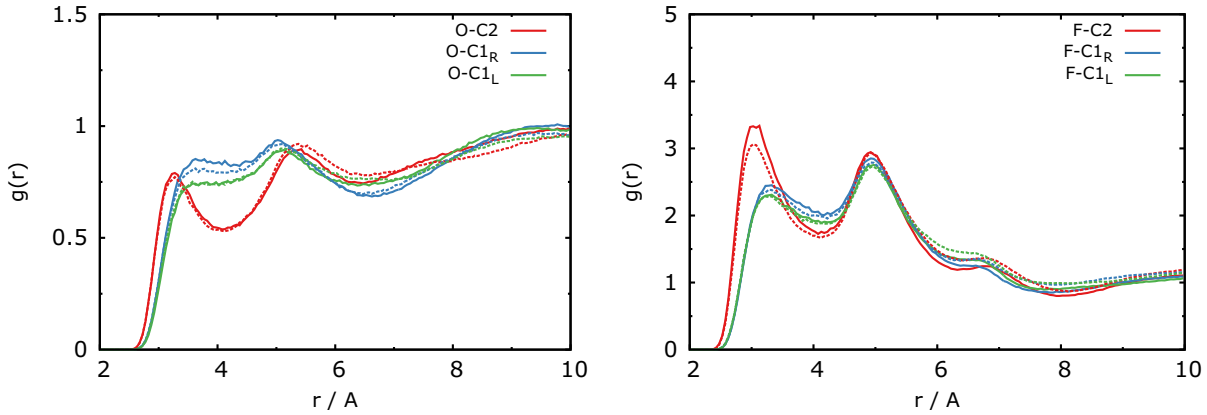


Figure D.15: Variation of radial distribution functions of (left) oxygen atoms of PEOs and (right) flourine atoms of $[BF_4]$ anions. Solid lines and dashed lines are for PEO/[BMIM][$BF_4$] mixture and PEO/[EMIM][$BF_4$] mixtures at 430 K for x=0.43, respectively.

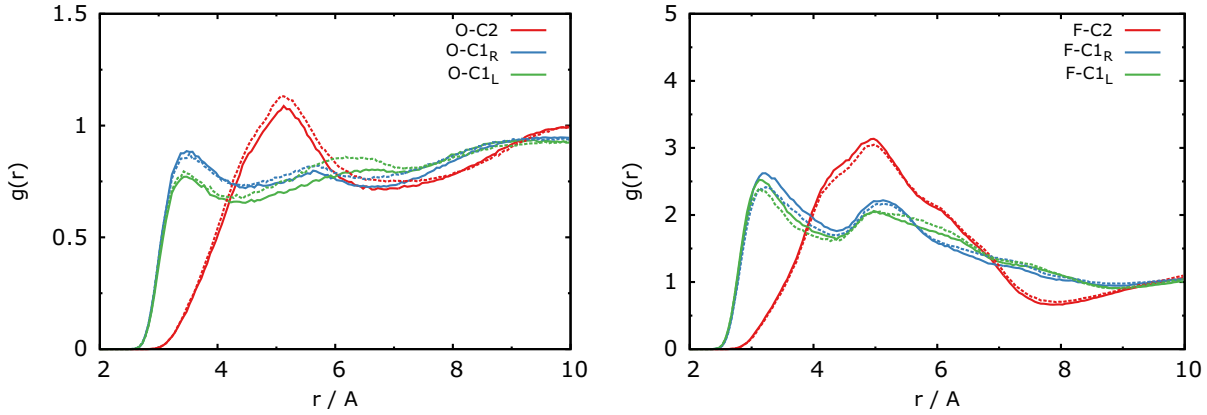


Figure D.16: Variation of radial distribution functions of (left) oxygen atoms of PEOs and (right) flourine atoms of $[BF_4]$ anions. Solid lines and dashed lines are for PEO/[BMMIM][$BF_4$] mixture and PEO/[EMMIM][$BF_4$] mixtures at 430 K for x=0.43, respectively.

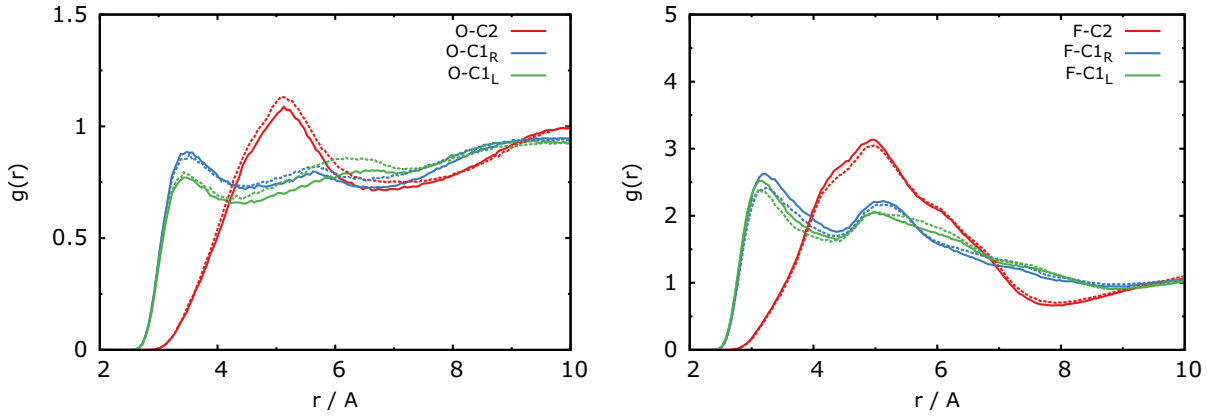


Figure D.17: Variation of radial distribution functions of (left) oxygen atoms of PEOs and (right) flourine atoms of [$BF_4$] anions. Solid lines and dashed lines are for PEO/[BMMIM][$BF_4$] mixture and PEO/[EMMIM][$BF_4$] mixtures at 430 K for x=0.43, respectively.

## D.6 Molar total coordination number of PEO oxygen atoms with unsaturated carbons (C1 and C2) of cation

## References

[1] Jesse G McDaniel and JR Schmidt. “Physically-motivated force fields from symmetry-adapted perturbation theory”. In: *The Journal of Physical Chemistry A* 117.10 (2013), pp. 2053–2066.

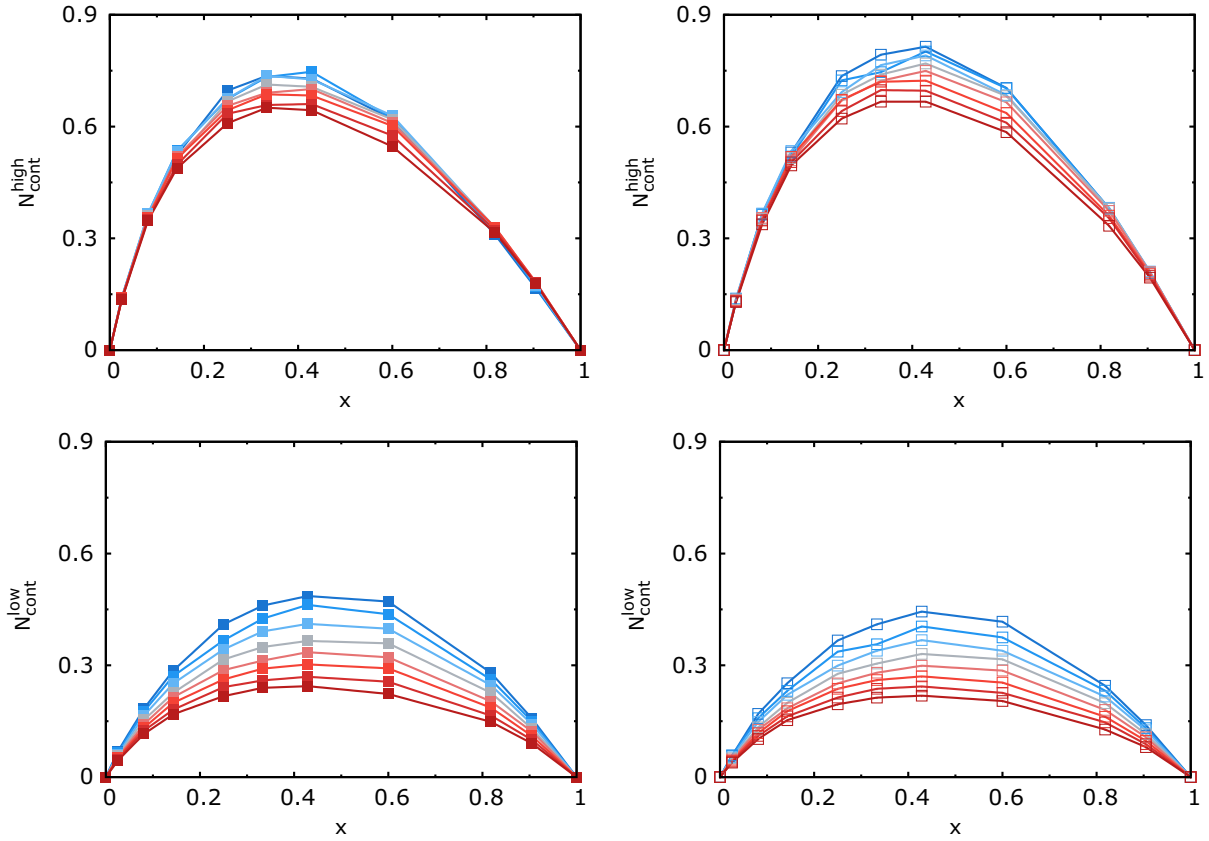


Figure D.18: Variation of $N_{cont}$ for (top) molar high contacts and (bottom) molar low contacts of oxygen atoms of PEOs in (left) PEO/[EMIM][$BF_4$] and (right) PEO/[EMMIM][$BF_4$] mixture. The meaning of colors is working temperature, as shown in Fig. D.2. Solid lines are the linearly interpolated lines.

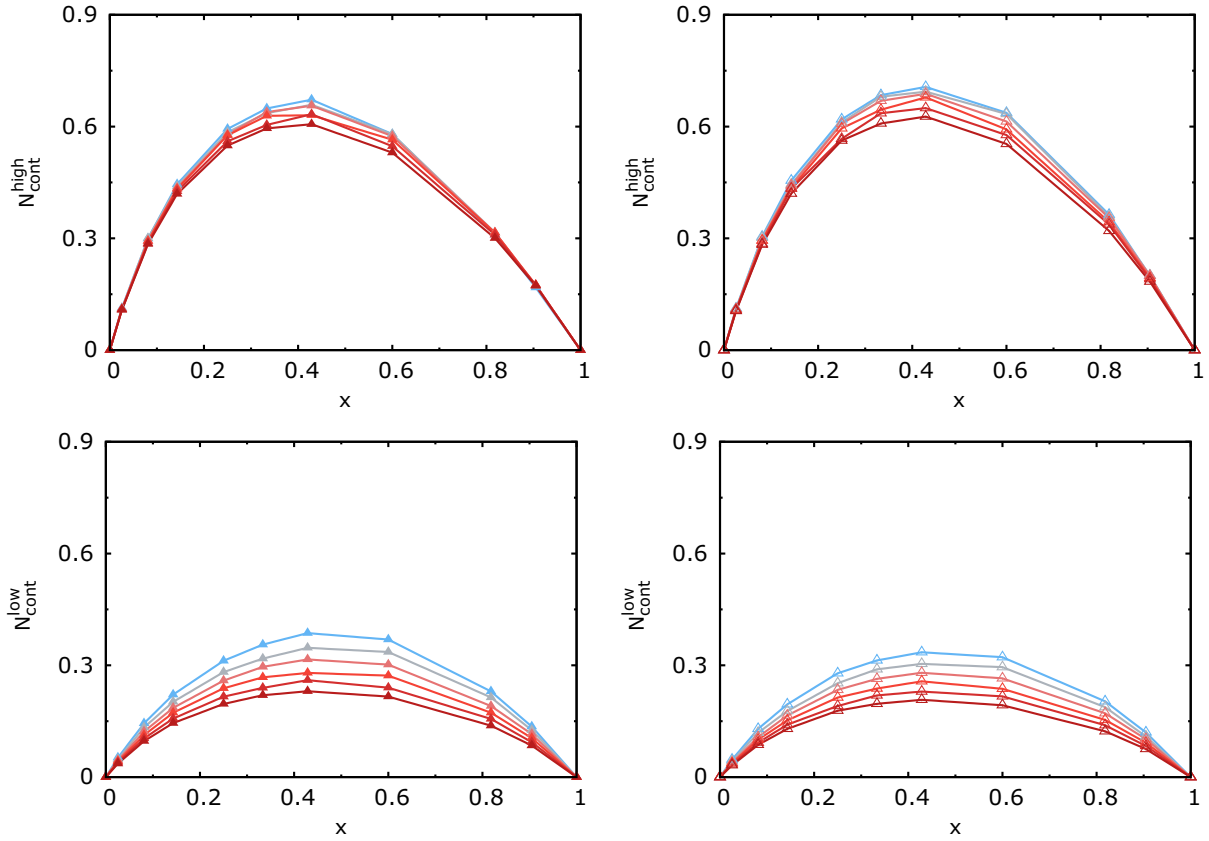


Figure D.19: Variation of $N_{cont}$ for (top) molar high contacts and (bottom) molar low contacts of oxygen atoms of PEOs in (left) PEO/[BMIM][$BF_4$] and (right) PEO/[BMMIM][$BF_4$] mixture. The meaning of colors is working temperature, as shown in Fig. D.3. Solid lines are the linearly interpolated lines.

# Appendix E

# List of Publications

1. Hyuntae Jung and Arun Yethiraj. "A simulation method for the phase diagram of complexfluid mixtures". In: *The Journal of chemical physics* 148. 24 (2018), p. 244903.

2. Hyuntae Jung and Arun Yethiraj. "Supervised Machine Learning of Binary Off-lattice Systems for Prediction of Phase Separation". *in preparation*

3. Hyuntae Jung and Arun Yethiraj. "Entropy-driven Phase Separation Behaviors of Poly(ethylene oxide) in C2 Methylated Imidazolium Ionic Liquids: A Molecular Simulation and Artificial Neural Network Study". *in preparation*